creative commons

COMMONS DEED

저작자표시-비영리-변경금지 2.0 대한민국

이용자는 아래의 조건을 따르는 경우에 한하여 자유롭게

- 이 저작물을 복제, 배포, 전송, 전시, 공연 및 방송할 수 있습니다.

다음과 같은 조건을 따라야 합니다:

저작자표시. 귀하는 원저작자를 표시하여야 합니다.

비영리. 귀하는 이 저작물을 영리 목적으로 이용할 수 없습니다.

변경금지. 귀하는 이 저작물을 개작, 변형 또는 가공할 수 없습니다.

- 귀하는, 이 저작물의 재이용이나 배포의 경우, 이 저작물에 적용된 이용허락조건을 명확하게 나타내어야 합니다.
- 저작권자로부터 별도의 허가를 받으면 이러한 조건들은 적용되지 않습니다.

저작권법에 따른 이용자의 권리는 위의 내용에 의하여 영향을 받지 않습니다.

이것은 이용허락규약(Legal Code)을 이해하기 쉽게 요약한 것입니다.

Disclaimer

dCollection

Double hydrophilic Block Copolymer-Templated Nanoparticle and Energy Application

Eunyong Seo

Department of Energy Engineering

Graduate School of UNIST

2017

Double Hydrophilic Block Copolymer-Templated Nanoparticle and Energy Application

Eunyong Seo

Department of Energy Engineering

Graduate School of UNIST

ULSAN NATIONAL INSTITUTE OF SCIENCE AND TECHNOLOGY

Double Hydrophilic Block Copolymer-Templated Nanoparticle and Energy Application

A thesis submitted to the Graduate School of UNIST
in partial fulfillment of the requirements for the degree of
Doctor of Philosophy

Eunyong Seo

1. 6. 2017

Approved by

Advisor
Byeong-Su Kim

ULSAN NATIONAL INSTITUTE OF SCIENCE AND TECHNOLOGY

Double Hydrophilic Block Copolymer-Templated Nanoparticle and Energy Application

Eunyong Seo

This certifies that the thesis/dissertation of Eunyong Seo is approved.

1. 6. 2017

Advisor: Byeong-Su Kim

Tae-Hyuk Kwon: Thesis Committee Member #1

Jin Young Kim: Thesis Committee Member #2

So Youn Kim: Thesis Committee Member #3

Hyung-il Lee: Thesis Committee Member #4;

ULSAN NATIONAL INSTITUTE OF
SCIENCE AND TECHNOLOGY

ULSAN NATIONAL INSTITUTE OF SCIENCE AND TECHNOLOGY

Abstract

This thesis describes a variety of utilization of double hydrophilic block copolymer (DHBC), in the synthesis of NP (NP) and its broad applications. Double hydrophilic block copolymer can be induced to form a micellar structure through electrostatic or coordinative interaction with metal precursor in aqueous solution. These interactions can then lead to the synthesis of metal or metal oxide NP with the treatment of proper reductant. Poly(ethylene oxide)-*block*-poly(acrylic acid) (PEO-*b*-PAA) copolymer used in this thesis consists of both water-soluble, and chemically distinct blocks. These different functionalities in each block are effectively utilized to synthesize NP with a controlled size and shape, further influencing the properties of resulting NP.

Au NPs can be prepared by interaction between metal precursor and carboxylate groups in PAA block through coordinative bonding. It is found that the size of Au NPs is independent of the molecular weight of PAA, while the micellar structure with metal precursor is mainly induced by PAA block. This result indicates the density of DHBC in a single NP decreases when the molecular weight of PAA block increases. This polymeric density difference of each NP shows the different stability in a harsh condition.

We have also demonstrated that additional Ag shell structure on Au NPs could be synthesized by utilizing the PEO block on the surface of Au NP template by DHBC, resulting in Au-Ag core-shell nanostructure. Interestingly, we found the changes in configuration of core-shell NP as well as the tunable thickness of Ag shell could be attributed to PEO chains, leading to the transition of intrinsic plasmonic absorption band in a wide spectrum. This phenomenon allows the integration of NPs into optoelectronic devices with enhanced properties.

Considering a wide range of tunability and functionalities of DHBCs, we anticipate that the DHBCs can offer a novel synthetic approaches for nanomaterials and allow the NPs to be applicable into various applications including biological and energy fields.

ULSAN NATIONAL INSTITUTE OF SCIENCE AND TECHNOLOGY

Contents

Chapter 1. Introduction of Thesis 18

1-1. Introduction 18

1-1-1. Nanomaterials 18

1-1-2. Properties of Nanomaterials 19

1-1-3. Application of Nanomaterials 20

1-2. Synthetic Methods in Nanoparticles 23

1-3. Surface Modification of Nanoparticles 25

1-4. Polymer Templated Nanoparticles 30

1-5. Overview of Thesis 33

1-6. Reference 34

Chapter 2. Double Hydrophilic Block Copolymer Templated Au Nanoparticles with Enhanced Catalytic Activity toward Nitroarene Reduction 38

2.1. Introduction 38

2.2. Experimental Section 40

2.3. Results and Discussion 42

2.4. Conclusion 59

2.5. References 60

Chapter 3. Plasmonic Transition via Interparticle Coupling of Au@Ag Core−Shell Nanostructures Sheathed in Double Hydrophilic Block Copolymer for High-Performance Polymer Solar Cell 64

3.1. Introduction 64

3.2. Experimental Section 68

ULSAN NATIONAL INSTITUTE OF SCIENCE AND TECHNOLOGY

3.3. Results and Discussion 71

3.4. Conclusion 93

3.5 References 94

Chapter 4. Highly Stable Au Nanoparticle Sheathed in Double Hydrophilic Block Copolymer 100

4.1. Introduction 100

4.2. Experimental Section 103

4.3. Results and Discussion 106

4.4. Conclusion 121

4.5. References 122

Chapter 5. Versatile Double Hydrophilic Block copolymer: Dual Role as Synthetic Nanoreactor and Ionic and Electronic Conduction Layer for Ruthenium Oxide Nanoparticle Supercapacitor 125

5.1. Introduction 125

5.2. Experimental Section 129

5.3. Results and Discussion 131

5.4. Conclusion 147

5.5. References 148

Chapter 6. Conclusions and Prospects 152

ULSAN NATIONAL INSTITUTE OF SCIENCE AND TECHNOLOGY

List of Figures

Chapter 1

Figure 1.1. Controlled shapes of nanomaterials categorized based on geometrical parameters. Reprinted with permission from ref. 5. Copyright 2011 Nature Publishing Group

Figure 1.2. Different heterogeneous nanostructured materials based on structural complexity. Reprinted with permission from ref. 6. Copyright 2011 Royal Society of Chemistry

Figure 1.3. Formation of Au NPs coated with organic shells by reduction of Au^{III} compounds in the presence of thiols. Reprinted with permission from ref. 14 and 15. Copyright 1994 and 2001 Royal Society of Chemistry.

Figure 1.4. Seed-mediated growth approach to making gold and silver nanorods of controlled aspect ratio. Reprinted with permission from ref. 21. Copyright 2005 American Chemical Society.

Figure 1.5. The surface modification of Au NPs in drug-delivery system carrier. Reprinted with permission from ref. 28. Copyright 2014 Nature Publishing Group

Figure 1.6. (a) Schematic description of a place-exchange reaction between dodecylamine (DDA)-functionalized Au NPs and a mixture of neutral 11-mercaptoundecanoic acid (MUA) and positively charged *N*,*N*,*N*-trimethyl(11-mercaptoundecyl)ammonium ion (TMA). Reprinted with permission from ref. 30. Copyright 2013 American Chemical Society. (b) A few examples of PEG-appended ligands together with the disulfide precursor. Reprinted with permission from ref. 31. Copyright 2010 American Chemical Society.

ULSAN NATIONAL INSTITUTE OF SCIENCE AND TECHNOLOGY

Figure 1.7. (a) Schematic representation of PS-*b*-PAA copolymer adsorption into pre-formed NPs with controlled sizes. Reprinted with permission from ref. 32. Copyright 2005 American Chemical Society. (b) Layer-by-Layer assembly for the construction of core-shell nanoparticle. Reprinted with permission from ref. 33. Copyright 2006 American Chemical Society.

Figure 1.8. A star-like-polymer template strategy for the synthesis of monodispersed colloidal nanoparticles. Reprinted with permission from ref. 39. Copyright 2013 Nature Publishing Group

Chapter 2

Figure 2.1. FT-IR spectra of (a) PEO-*b*-PAA, (b) PEO-*b*-PAA with NaOH, and (c) PEO-*b*-PAA with NaOH and Au precursor. The schematic description of the coordinative bond formation between Au precursor and carboxylate group is displayed in the right panel.

Figure 2.2. Dynamic light scattering (DLS) analysis of DHBC, DHBC with Au precursor and Au@DHBC NPs, providing the hydrodynamic diameter range of 0.10 - 5.62 nm, 0.67 - 12.87 nm and 8.01 - 31.62 nm, respectively.

Figure 2.3. (a and b) TEM images of synthesized Au@DHBC. Scale bar in (a) represents 10 nm and (b) 2 nm. Inset in **Figure** 2b shows the crystalline lattice fringe of Au NP. (c) Corresponding size distribution histogram of as-prepared Au@DHBC NPs. (d) UV/vis spectrum of synthesized suspension of Au@DHBC NPs. Inset shows the photograph image of a suspension of Au@DHBC NPs.

Figure 2.4. TEM images of Au@DHBC NPs before purification by centrifuge, showing the large Au aggregates. Scale bar in (a) represents 20 nm and (b) 5 nm.

Figure 2. 5. TEM images of Au@DHBC NPs using 0.0067 mmol of $HAuCl_4 \cdot 3H_2O$. The

ULSAN NATIONAL INSTITUTE OF SCIENCE AND TECHNOLOGY

diameter of Au NPs is ranged from 1 to 4 nm, which is smaller than that of Au@DHBC NPs used as a catalyst in the reduction of nitroarenes presented in this work. Scale bar in (a) represents 10 nm and (b) 2 nm.

Figure 2.6. TEM images of Au@DHBC NPs reduced by ascorbic acid. The diameter of Au@DHBC NPs is ranged from 22 to 29 nm. Scale bar in (a) represents 20 nm and (b) 10 nm.

Figure 2.7. Thermogravimetric analysis (TGA) curves of (black) pure DHBC of PEO-b-PAA, and (red) synthesized Au@DHBC NPs. The samples were subjected to heating at a rate of 10 ^{o}C min-1 under air atmosphere.

Figure 2.8. TEM images of Au@DHBC NPs annealed at 400 ^{o}C for 2 h under Ar atmosphere. The size of Au@DHBC NPs surrounded by polymeric residue increased after thermal treatment. Scale bar in (a) represents 100 nm and (b) 20 nm

Figure 2.9. (a) The color change of 4-nitrophenol reduction with Au@DHBC NPs catalyst and NaBH4. (b) Representative time-dependent UV/vis absorption spectra for the reduction of 4-nitrophenol over Au@DHBC NP catalyst in aqueous media at 303 K. (c) Plot of ln(Ct/C0) versus time spectra for the reduction of 4-nitrophenol over Au@DHBC catalyst under different mol% of catalyst and equiv. of NaBH4 used. (d) Plot of ln(Ct/C0) versus time for the reduction of 4-nitrophenol over Au@DHBC NP catalysts under different temperatures at 0.50 mol% of catalyst and 300 equiv. of NaBH4. Inset shows the corresponding Arrhenius plot.

Figure 2.10. UV/vis spectra of 4-nitrophenol before and after the addition of $NaBH_4$.

Figure 2.11. (a) TEM image of spherical Au NPs synthesized by citric acid, whose diameter is about 10.7 ± 4.3 nm (Scale bar in (a) represents 2 nm), and (b) time-dependent UV/vis spectra of 4-nitrophenol catalyzed using Au NPs synthesized by citric acid. 10 mL of 7.50×10^{-4} M 4-nitrophenol, 0.118 mL of 3.178×10^{-4} M Au catalyst (0.50 mol% with respect to the Au concentration) and 1.0 mL of 2.22 M $NaBH_4$ (300 equiv. to the substrate) were used for the reduction of 4-nitrophenol.

ULSAN NATIONAL INSTITUTE OF SCIENCE AND TECHNOLOGY

Figure 2.12. UV/vis spectra of 4-nitrophenol with $NaBH_4$ without Au@DHBC NP catalyst.

Figure 2.13. TEM images of the synthesized (a, b) Pd@DHBC NPs and (c, d) Pt@DHBC NPs with a histogram of size distribution. The average diameter is 87.9 ± 18.1 nm for Pd NPs and 55.5 ± 10.6 nm for Pt NPs, respectively. Scale bar in a and c represents 100 nm and b and d 20 nm.

Chapter 3

Figure 3.1. Isolated Au@Ag NPs by DHBC. TEM images of (a) Au@DHBC NPs and (b, c) Au@Ag@DHBC NPs synthesized by 0.1 and 0.9 μmol $AgNO_3$, denoted as Au@$Ag_{0.1}$@DHBC NPs and Au@$Ag_{0.9}$@DHBC NPs, respectively. Inset **Figure**s in b and c show the dark field STEM images of Au@Ag@DHBC NPs. (d) Compositional line profiles of representative Au@Ag@DHBC NPs shown in **Figure** 1c. (e) UV-Vis spectra of Au@DHBC NPs and Au@Ag@DHBC NPs.

Figure 3.2. (a, b) Representative TEM images and (c) size distribution of Au@DHBC NPs prepared by modified method.[83] Specifically, the DHBC poly(ethylene oxide)-*block*-poly(acrylic acid) (PEO-*b*-PAA) is used as both a template and stabilizer for Au NPs. Typically, the carboxylate group of the PAA block interacts with the Au precursor via coordinative bonding between the metal precursor and the carboxylate group. Then, the PAA blocks segregate to form micellar structures in solution. Once the micelle formation is induced, the PEO-*b*-PAA micelle acts as a nanoreactor to template the growth of the Au NP within the micellar core upon the addition of a reducing agent, *L*-ascorbic acid. As the Au precursor is reduced to Au NPs, the transparent yellow solution turns reddish, indicating the formation of Au NPs. The average diameter of the Au NPs formed within the DHBC template (Au@DHBC NPs) is 17.0 ± 4.1 nm.

ULSAN NATIONAL INSTITUTE OF SCIENCE AND TECHNOLOGY

Figure 3.3. Low-magnification dark field HAADF STEM images of (a) Au@DHBC NPs, (b) Au@$Ag_{0.1}$@DHBC NPs, and (c) Au@$Ag_{0.9}$@DHBC NPs. Insets in b and c show the high resolution dark field TEM images of Au@Ag@DHBC NPs.

Figure 3.4. STEM analysis of representative Au@Ag@DHBC NPs. (a-b) Energy dispersive X-ray spectroscopy data of core-shell structure showing the component of Au and Ag at the different site of nanoparticles. The other atoms are observed because of the TEM grid.

Figure 3.5. (a) (top) A series of TEM images and (bottom) their corresponding photographs of the Au@Ag@DHBC solution. The scale bar in the TEM images is 10 nm. (b) Average size of Au@Ag_n@DHBC NPs as a function of the concentration of Ag precursors (n = 0.0-1.0) and their corresponding Ag shell thickness. (c) UV-Vis spectra collected for Au@Ag_n@DHBC NPs produced with different concentrations of Ag precursor (n = 0.0-1.0).

Figure 3.6. A comparison of the (a) UV-Vis spectra and (b) FDTD simulation results collected for Au@Ag_n@DHBC NPs produced with different concentrations of Ag precursor (n = 0.0 – 0.9). The experiment data indicates that the plasmon bands of the NPs initially blue-shifted and then exhibited strong absorption with increasing Ag shell thickness, showing a similar trend as the simulation data.

Figure 3.7. (a) Low and (b) high-resolution TEM images of Au@$Ag_{0.9}$@DHBC NPs.

Figure 3.8. Coupled Au@Ag NPs by DHBC. (a-c) TEM images of Au@Ag@DHBC NPs synthesized by (a) 1.0, (b) 1.4 and (c) 1.8 μmol of Ag precursor, denoted as Au@$Ag_{1.0}$@DHBC, Au@$Ag_{1.4}$@DHBC and Au@$Ag_{1.8}$@DHBC, respectively.

Figure 3.9. (a) UV-Vis absorption spectra of Au@Ag@DHBC with Ag precursor concentrations in the range of 1.0 to 2.0 μmol and (b) the corresponding plasmon band plots of Au@Ag@DHBC NPs by transverse absorption (line T) and plasmon coupling

ULSAN NATIONAL INSTITUTE OF SCIENCE AND TECHNOLOGY

(line C).

Figure 3.10. The plot showing vertical length of junction formed between NPs as a function of Ag precursor. Inset indicating the area of junction and corresponding vertical length.

Figure 3.11. (a) A series of TEM images of Au@$Ag_{1.6}$@DHBC as a function of reaction time (5, 10, 15, 30, and 45 min). (b) Schematic drawings of the growth of the Ag layer and interparticle coupling. (c) Dynamic light scattering (DLS) analysis showing the hydrodynamic diameter changes during the growth of Au@$Ag_{1.6}$@DHBC NPs.

Figure 3.12. Device characteristics and spectral responses of plasmonic PSCs. (a) Schematic of polymer solar cell with chemical structures of PTB7-Th and $PC_{71}BM$, (b) current density-voltage (J-V) characteristics and (c) IPCE of a control device (black circles) and the best plasmonic PSCs with embedded Au@Ag@DHBC NPs (red and blue circles). (d) Comparison of enhanced IPCE and absorbance by Au@Ag@DHBC NPs.

Figure 3.13. AFM images of active layer with con**Fig**urations of (a) ITO/PEDOT:PSS/active layer, (b) ITO/PEDOT:PSS/isolated NPs/active layer, and (c) ITO/PEDOT:PSS/coupled NPs/active layer. Scale bar in all images represents 500 nm. The thickness of the films was measured with profilometer.

Figure 3.14. Device characteristics and spectral responses of plasmonic PSCs with and without Au@DHBC NPs. (a) Current density-voltage (J-V)w characteristics and (b) IPCE of a control device (black circles) and the best plasmonic PSCs with embedded Au@DHBC NPS (red circle). (c) Enhanced IPCE of device with Au@DHBC NPs in comparison with control device.

Figure 3.15. Representative height-mode AFM images of PEDOT:PSS film coated with (a) isolated Au@$Ag_{0.9}$@DHBC NPs and (b) coupled Au@$Ag_{1.6}$@DHBC NPs. The images were taken with NPs solutions after filtration.

ULSAN NATIONAL INSTITUTE OF SCIENCE AND TECHNOLOGY

Figure 3.16. (a) Schematic description of different arrangement of plasmonic Au@Ag@DHBC NPs embedded within active layer on the device and (b) corresponding FDTD simulated extinction. (c) UV-Vis spectra of PTB7/$PC_{71}BM$ without NPs and with isolated Au@$Ag_{0.9}$@DHBC NPs or coupled Au@$Ag_{1.6}$@DHBC NPs.

Figure 3.17. The absorption and scattering spectra on the device with plasmonic Au@Ag core-shell NPs, which is analyzed using FDTD simulation.

Figure 3.18. (a, b) Representative TEM images of (a) free Au and (b) free Ag NPs without DHBC and (c) normalized UV-vis spectra of Au and Ag NP solutions.

Figure 3.19. Steady-state photoluminescence (PL) spectra of fluorescence of SY films by the effect of isolated and coupled NPs (Au@$Ag_{0.9}$@DHBC and Au@$Ag_{1.6}$@DHBC NPs, respectively) and free Au and Ag NPs synthesized without DHBC template.

Chapter 4

Figure 4.1. (a) Synthetic Scheme of the representative double hydrophilic block copolymer (DHBC), $PEO_{5.0k}$-*b*-$PAA_{6.9k}$. (b) ^{1}H NMR of spectra of PEO-Br macroinitiator (black), PEO-*b*-P*t*BA copolymer (red), and PEO-*b*-PAA (blue). (c) GPC traces of PEO-Br macroinitiator (black) and PEO-*b*-P*t*BA (red) in $CHCl_3$.

Figure 4.2. SEC traces of PEO macroinitiator and PEO-*b*-P*t*BA copolymers in Chloroform GPC analysis. PMMA was used as a standard to obtain the molecular weight and molecular weight distribution shown in Table 1.

Figure 4.3. (a) Monomer conversion and polydispersity index and (b) SEC traces of PEO_{5k}-*b*-P*t*$BA_{6.9k}$ copolymer (P1) as a function of reaction time.

Figure 4.4. (a) Scheme of reaction between sodium acetate and gold precursor. (b) ^{1}H NMR spectra of pure sodium acetate (upper) and (b) complex with Au precursor in

ULSAN NATIONAL INSTITUTE OF SCIENCE AND TECHNOLOGY

methanol-d_4 at room temperature. The proton signal of the sodium acetate shifted to downfield by the complexation with gold precursor. (c) Job plots were investigated at reaction time of 1.0 h and 12.0 h after complexation with sodium acetate and Au precursor, showing efficient interaction when the ratio of sodium acetate to Au precursor was 0.667:0.333.

Figure 4.5. Average diameter of (a) micelle of PEO_{5k}-*b*-$PAA_{6.9k}$ and Au precursor (before reduction) and (b) Au NP by PEO_{5k}-*b*-$PAA_{6.9k}$ (after reduction by ascorbic acid), depending on the molar ratio, *R* of acrylic acid unit in PEO_{5k}-*b*-$PAA_{6.9k}$ to Au precursor

Figure 4.6. Schematic description of Au NPs sheathed in double hydrophilic block copolymer, PEO_{5k}-*b*-$PAA_{6.9k}$. (b) TEM image and (c) Size distribution of Au@PEO-*b*-PAA NPs. Inset in Figure b is a high-resolution TEM image of representative Au@PEO-*b*-PAA NPs.

Figure 4.7.Thermal stability of (a) Au@P2 and Au@citrate NPs depending on the reaction time at 95 ^{o}C in oven. TEM images of each Au NP were measured before and after thermal annealing. (b) Photograph of agarose gel without and with Au@P2 or Au@citrate NPs. The particle concentration of Au solution in gel solution was fixed at 0.10 nM.

Figure 4.8. Photographs (a) Au@P2 and Au@citrate NP in various buffer solutions with different pH. (b, c) Relative stability of Au@P2 NPs in acid and basic conditions.

Figure 4. 9. Thermal stability at 95 ^{o}C and (b) cyanide digestion in KCN solution (12 mM) of Au@citrate and Au NPs by various PEO-*b*-PAA copolymers..

Chapter 5

Figure 5.1. (a,b) TEM images of as-prepared hydrous $RuO_2 \cdot xH_2O$ nanoparticles. Inset in

ULSAN NATIONAL INSTITUTE OF SCIENCE AND TECHNOLOGY

Figure 5.1b shows the crystalline lattice fringe of $RuO_2 \cdot xH_2O$ nanoparticles. (c) Corresponding size distribution histogram with an image of as-prepared hydrous $RuO_2 \cdot xH_2O$ nanoparticle suspension.

Figure 5. 2. FT-IR spectra of (a) PEO-*b*-PAA, (b) PEO-*b*-PAA with NaOH, (c) PEO-*b*-PAA with NaOH and $RuCl_3 \cdot xH_2O$, and (d) PAA with NaOH and $RuCl_3 \cdot xH_2O$. Note that the PEO-*b*-PAA shows the C=O stretching vibration of the carboxylic group at 1729 cm^{-1} and the C-O stretching vibration of PEO block and PAA block at 1241 and 1091 cm^{-1}, respectively. Upon complexation with Ru^{3+} through electrostatic interaction to form micellar structure, the carboxylic acid groups of PAA block are dissociated into COO^- groups, which correspond to the absorption peaks at 1625 and 1410 cm^{-1} assigned to asymmetric and symmetric stretching vibrations of COO^-, while a peak of C-O observed in PEO block still remains at 1104 cm^{-1}. This implies that the carboxylate groups of PAA block are easily involved in the reaction by combining with Ru^{3+}. In a control experiment using only PAA polymer, the absorption peaks at 1561 and 1404 cm^{-1} could be assigned to asymmetric and symmetric stretching vibrations of COO^-, supporting carboxylate groups in PAA complex with Ru^{3+}.

Figure 5.3. (a) Deconvoluted high-resolution XPS spectra of as-prepared hydrous $RuO_2 \cdot xH_2O$ nanoparticles. (b) XRD spectra of various RuO_2 nanoparticles before and after annealing at different temperatures. Note the circles in **Figure** 2b represent the peak matching to metallic ruthenium.

Figure 5.4. *In situ* XRD patterns of hydrous $RuO_2 \cdot xH_2O$ nanoparticles with increasing temperature under ambient condition. It indicates that the crystalline RuO_2 structure is evolved from amorphous structure of as-prepared hydrous $RuO_2 \cdot xH_2O$ near at 300 ^oC. Note that the peaks marked with blue triangle are assigned to the Al_2O_3substrate, where the sample was loaded.

Figure 5. 5. FT-IR spectra of RuO_2 nanoparticles annealed at 400 ^oC and 600 ^oC. Both spectra reveals the presence of residual polymeric layer, including symmetric stretching of carboxylate peaks at 1435 cm^{-1}, which corresponds to the surface-bound strong

ULSAN NATIONAL INSTITUTE OF SCIENCE AND TECHNOLOGY

coordinating carboxylate groups, and the other strong peak observed at 863 cm^{-1} due to the strong rocking of methylene (-CH_2-) backbone of the polymer.

Figure 5.6. Representative TEM images of RuO_2 nanoparticles annealed at various temperatures. (a, b) 200 ^oC, (d, e) 400 ^oC and (g, h) 600 ^oC. The inset images show the crystalline plane of RuO_2 nanoparticles. (c, f, i) The corresponding size distribution histograms of RuO_2 nanoparticles averaged over 50 samples.

Figure 5.7. (a) Thermogravimetric analysis (TGA) and (b) differential thermal analysis (DTA) curves of as-prepared hydrous $RuO_2 \cdot xH_2O$ nanoparticles. The sample was subjected to heating at a rate of 10 ^oC/min under air atmosphere.

Figure 5.8. Comparison of electrochemical properties of all RuO_2 nanoparticle samples. (a) Cyclic voltammograms (CVs) of RuO_2 nanoparticle electrodes at a scan rate of 200 mV/s, (b) scan rate dependent current density plot of RuO_2 nanoparticles after annealing at 400 ^oC with a scan rate of 10, 20, 50, 100, 200 mV/s. Inset shows the peak current density versus scan rate plot in an equi-span log-log scale with a calculated slope of 1.0, (c) dependence of the capacitance loss on the scan rate of all RuO_2 nanoparticle samples, and (d) galvanostat cycling of RuO_2 after annealing at 400 ^oC with a current density of 20 A/g. Inset shows the charge/discharge curves with various current densities. All electrochemical properties were collected in a three-electrode system with a SCE reference in 1.0 M H_2SO_4 electrolyte.

Figure 5. 9. Representative HR-TEM image of RuO_2 nanoparticles annealed at 600 ^oC. Highly crystalline carbon layer is formed on the surface of RuO_2 nanoparticles.

Figure 5.10. Schematic representation of the origin of enhanced capacitive performance of RuO_2 nanoparticles annealed at 400 ^oC with the corresponding TEM image.

Figure 5. 11. Nyquist plots for an electrode of (black square) as-prepared RuO_2 and (red circle) RuO_2 annealed at 400 ^oC, measured over a frequency range from 100 mHz to 200 kHz at 0.6 V.

ULSAN NATIONAL INSTITUTE OF
SCIENCE AND TECHNOLOGY

Figure 5.12. Comparison of capacitance values of all RuO_2 nanoparticles samples annealed at different temperature ranges. Capacitance values were obtained with a cyclic voltammetry measurement at a scan rate of 10 mV/s.

ULSAN NATIONAL INSTITUTE OF SCIENCE AND TECHNOLOGY

List of Tables

Chapter 2

Table 2.1. Reduction of various nitroarenes using Au@DHBC NP catalyst

Chapter 3

Table 3.1. Device Characteristics of PTB7-Th:$PC_{71}BM$-based PSCs with Au@Ag@DHBC NPs

Table 3.2. Device Characteristics of PTB7-Th:$PC_{71}BM$-based PSCs with Au@DHBC NPs.

Table 3.3. PL quantum efficiency (PLQE) of films with different configurations measured inside an integrating sphere with an excitation wavelength of 470 nm.

Chapter 4

Table 4. 1. Characterization of PEO-b-PAA copolymers

Table 4.2. Characterization of Au NPs by PEO_{5k}-*b*-$PAA_{6.9k}$ copolymer

Table 4. 3. Characterization of Au NPs prepared by citrate and PEO-*b*-PAA copolymers

Chapter 5

Table 5. 1. Comparison of capacitance values of all RuO_2 nanoparticles samples annealed at different temperature ranges measured at various scan rates.

ULSAN NATIONAL INSTITUTE OF SCIENCE AND TECHNOLOGY

List of Schemes

Chapter 2.

Scheme 2.1. Schematic illustration of the synthesis of Au@DHBC NP through the coordinative bonding between the Au precursor and a double hydrophilic block copolymer (DHBC) (PEO-*b*-PAA) as a soft template.

Chapter 3

Scheme 3.1. Schematic Illustration of the Synthesis of Au-Ag Core-Shell NPs Using a Double Hydrophilic Block Copolymer Template (Au@Ag@DHBC NPs). Isolated and Coupled Au@Ag@DHBC NPs via a Seed Growth Method Are Determined by the Concentration of Ag Precursor.

Chapter 4

Scheme 4.1. Synthetic approaches of Au nanoparticle and corresponding stability in various conditions.

Scheme 4.2. Proposed formation of nanoparticles synthesized by different molecular weight of PAA block

Scheme 4.3. Synthesis of Au@DHBC NPs through micelle complexation between double hydrophilic block copolymer (DHBC), PEO-*b*-PAA, and metal precursor, hydrated $HAuCl_4$.

ULSAN NATIONAL INSTITUTE OF SCIENCE AND TECHNOLOGY

Scheme 4.4. Proposed description of NP and its property, depending on both the different molecular weight of PAA block and corresponding density of PEO block on the surface of NP.

Chapter 5

Scheme 5.1. Schematic illustration of synthesis of RuO_2 nanoparticles using double hydrophilic block copolymer as a template and resulting nanostructures after annealing at high temperature.

ULSAN NATIONAL INSTITUTE OF SCIENCE AND TECHNOLOGY

Chapter 1.

Introduction of Thesis

1-1. Introduction

1-1-1. Nanomaterials

Nanoscience is an interdisciplinary field that has been extensively developed over the past decades. Nanoparticles (NPs) is a materials with size of 1-100 nm, which can bridge the gap in the middle of small molecules and bulk materials. Unique characteristics such as optical, electrical, and magnetic properties displayed at nano-scale are dependent on the particle size, shape, and distance between particles as well as environment conditions.[1] Metal NPs are an intensive subject of recent research because NPs provide new opportunities for utilization in catalytic, optical, and electronic properties. Noble Metal NPs have immense potential for applications in photocatalysis, sensors, electrode materials, and energy conversion or storages. For example, Au or Ag NPs with size of less than 20 nm have a characteristic collective oscillation frequency of surface plasmon resonance, which are employed as a biosensor[2] or a material for energy conversion.[3]

The initial report of scientific researches was the colloidal gold NPs (Au NPs) prepared by Michael Faraday in 1857.[4] Since the nano-sized Au was discovered, many researches for synthesis, characterization, modification of NPs have been widely conducted around the world. Studies on control over the size and morphology of NPs was numerously achieved, allowing them to be tunable in nano-scale (Figure 1.1).[5] Ran et al. described 4 major categories of heterogeneous nanomaterials on the basis of their structural complexity (Figure 1.2)[6]. They split these major categories into sub categories by combining the nanomaterials into sub-level nanostructures.

ULSAN NATIONAL INSTITUTE OF SCIENCE AND TECHNOLOGY

1-1-2. Properties of Nanomaterials

Nanomaterials have the structural features in between of those of atoms and the bulk materials. While most microstructured materials have similar properties to the corresponding bulk materials, the properties of materials with nanometer dimensions are significantly different from those of atoms and bulks materials. This is mainly due to the nanometer size of the materials which render them: (1) large fraction of surface atoms; (2) high surface energy; (3) spatial confinement; (4) reduced imperfections, which do not exist in the corresponding bulk materials. Due to their small dimensions, nanomaterials have extremely large surface area to volume ratio, which makes a large to be the surface or interfacial atoms, resulting in more “surface” dependent material properties. Especially when the sizes of nanomaterials are comparable to length, the entire material will be affected by the surface properties of nanomaterials. This in turn may enhance or modify the properties of the bulk materials. For example, metallic NPs can be used as very active catalysts. Chemical sensors from NPs and nanowires enhanced the sensitivity and sensor selectivity. The nanometer feature sizes of nanomaterials also have spatial confinement effect on the materials, which bring the quantum effects. The energy band structure and charge carrier density in the materials can be modified quite differently from their bulk and in turn will modify the electronic and optical properties of the materials. For example, lasers and light emitting diodes (LED) from both of the quantum dots and quantum wires are very promising in the future optoelections. High density information storage using quantum dot devices is also a fast developing area. Reduced imperfections are also an important factor in determination of the properties of the nanomaterials. Nanosturctures and Nanomaterials favors of a self- purification process in that the impurities and intrinsic material defects will move to near the surface upon thermal annealing. This increased materials perfection affects the properties of nanomaterials. For example, the chemical stability for certain nanomaterials may be enhanced, the mechanical properties of nanomaterials will be better than the bulk materials. The superior mechanical properties of carbon nanotubes are well known. Due to their nanometer size, nanomaterials are already known to have many novel properties. Many novel applications of the nanomaterials rose from these novel properties have also been proposed.

ULSAN NATIONAL INSTITUTE OF SCIENCE AND TECHNOLOGY

1-1-3. Application of Nanomaterials

Nanomaterials have been employed into wide range of applications in the field of electronics, fuel cells, batteries, agriculture, food industry, and medicine. Over the past a few decades, nanomaterials have been employed in biological researches and biomedicine. The effect of various parameters such as sizes, shapes, and surface properties of NPs on biological phenomena or processes, including circulation, cellular internalization, transportation, tumor targeting, delivery, and body clearance. NPs can also applied as optical probes in sensor and contrast agents in optical imaging.

Among noble metals, Au is chemically inert, very stable metals, therefore, it is resistant to oxidation. Due to their interesting properties, Au NPs have been widely investigated as a catalyst in CO and H_2 oxidation, NO reduction, water-gas shift reaction, CO_2 hydrogenation, and in broad catalytic organic reaction. Additionally, Au catalysts supported oxide have shown enhanced catalytic efficiency, which is being consistently explored to develop new catalytic systems.

ULSAN NATIONAL INSTITUTE OF
SCIENCE AND TECHNOLOGY

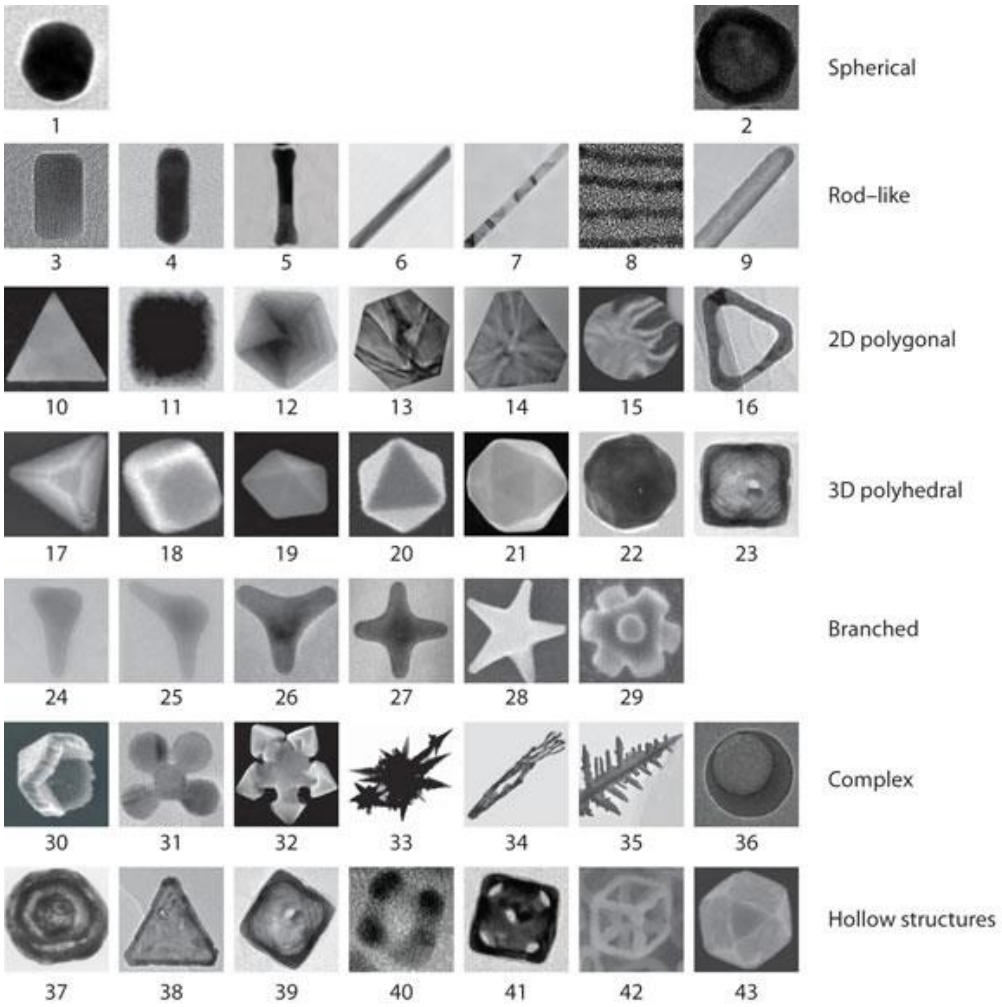

Figure 1.9. Controlled shapes of nanomaterials categorized based on geometrical parameters. Reprinted with permission from ref. 5. Copyright 2011 Nature Publishing Group

ULSAN NATIONAL INSTITUTE OF SCIENCE AND TECHNOLOGY

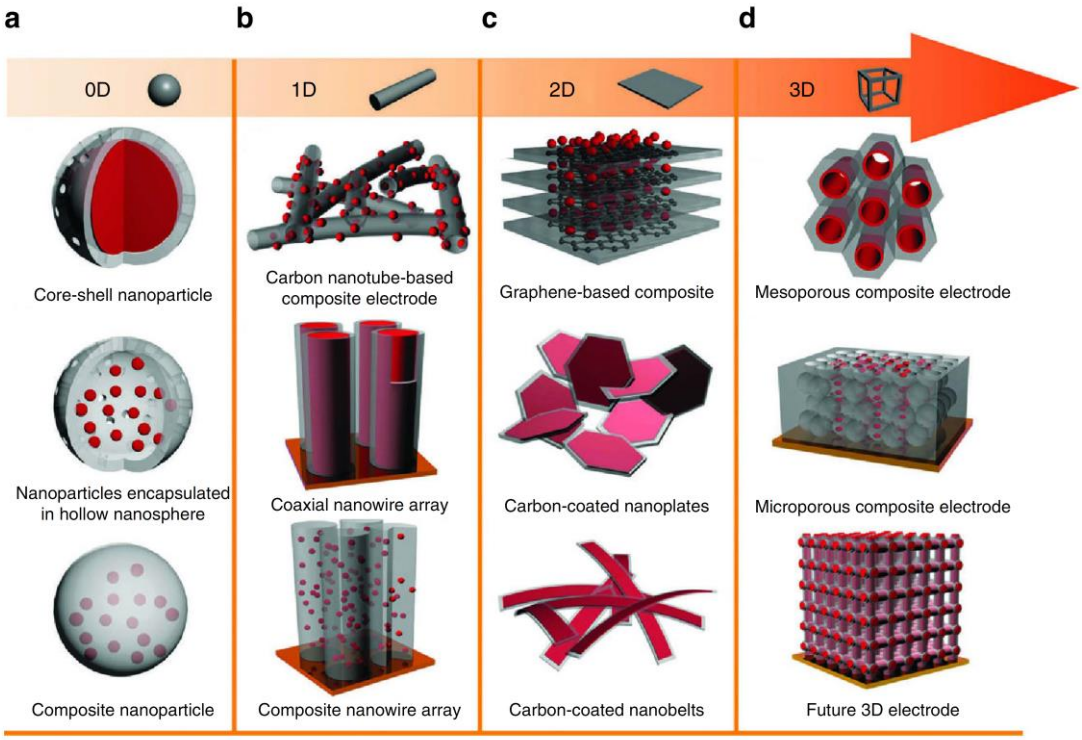

Figure 1.10. Different heterogeneous nanostructured materials based on structural complexity. Reprinted with permission from ref. 6. Copyright 2011 Royal Society of Chemistry

ULSAN NATIONAL INSTITUTE OF SCIENCE AND TECHNOLOGY

1-2. Synthetic Methods in Nanoparticles

Over the past decade, the field of nanomaterials has been significantly developed, focusing on the broad applications as well as their generation. Most of these applications utilizing nanomaterials require large amount with high quality, multiple functionalities of surface, high stability under various environments of nanomaterials, which leads to development of a number of method, and post-processing.

Metal NPs including Au, Ag, and Cu, have been intensively studied because of various properties such as optical, electronic, and catalytic effect in broad applications.[1, 7-8] Such properties of NPs are different of those of bulk or molecular components, which were experimentally and theoretically investigated by many scientists. Among various NPs, gold is a very interesting material in nanoscience; for example, nanosized Au has a very stability, higher electronic conductivity than silicon, and the unique surface chemistry that can allow for broad applications.[1, 9]

Up to now, numerous methods for the preparation of Au NPs have been reported by many researchers. Generally, wet-chemical method is very useful to grow a broad range of particle types, and to control over size and shape of particle and provide narrow particle polydispersity. The wet-chemical synthesis of colloidal NP was found by the pioneering work of Faraday. The aqueous solution of gold chloride ions was reduced into red colored gold NPs using reductant, which was the first example of methodology to describe the method of preparing the nanosized materials.

One of the popular route of Au NPs is the method based on sodium citrate in boiling solution.[10-11] This method allows the size of NPs to be controlled ranging from 10 to over 100 nm) by the different ratio of gold precursor and sodium citrate. Brust et al. reported the two-phase reduction.[12-13] They used alkanethiol as a ligand to protect the Au surface, and the size of NPs was tunable between ~1 and 10 nm as a function of reactant ratio between Au precursor and ligand (Figure 1.3).[14-15] Murry et al. developed this synthesis by functionalization of NP through the ligand exchange method.[16] In other approach, one-phase method without surfactants was developed in organic solutions including methanol, tetrahydrofuran.[17-18] Murphy et al. reported that Au NPs were easily prepared by citric acid as capping and reducing agents, and additionally, this method provided the tunable size of NPs in the range over 100 nm shown in Figure 1.4.[19-21]

ULSAN NATIONAL INSTITUTE OF SCIENCE AND TECHNOLOGY

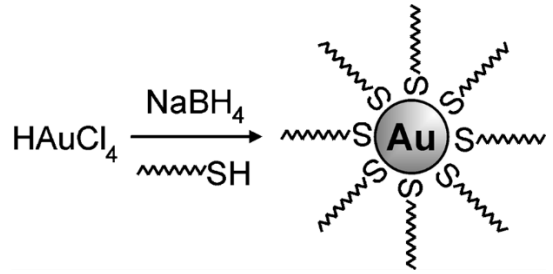

$$AuCl_4^-(aq) + N(C_8H_{17})_4^+(C_6H_5Me) \rightarrow N(C_8H_{17})_4^+AuCl_4^-(C_6H_5Me)$$

$$mAuCl_4^-(C_6H_5Me) + nC_{12}H_{25}SH(C_6H_5Me) + 3m\,e^- \rightarrow 4m\,Cl^-(aq) + [Au_m(C_{12}H_{25}SH)_n](C_6H_5Me)$$

Figure 1.11. Formation of Au NPs coated with organic shells by reduction of Au^{III} compounds in the presence of thiols. Reprinted with permission from ref. 14 and 15. Copyright 1994 and 2001 Royal Society of Chemistry.

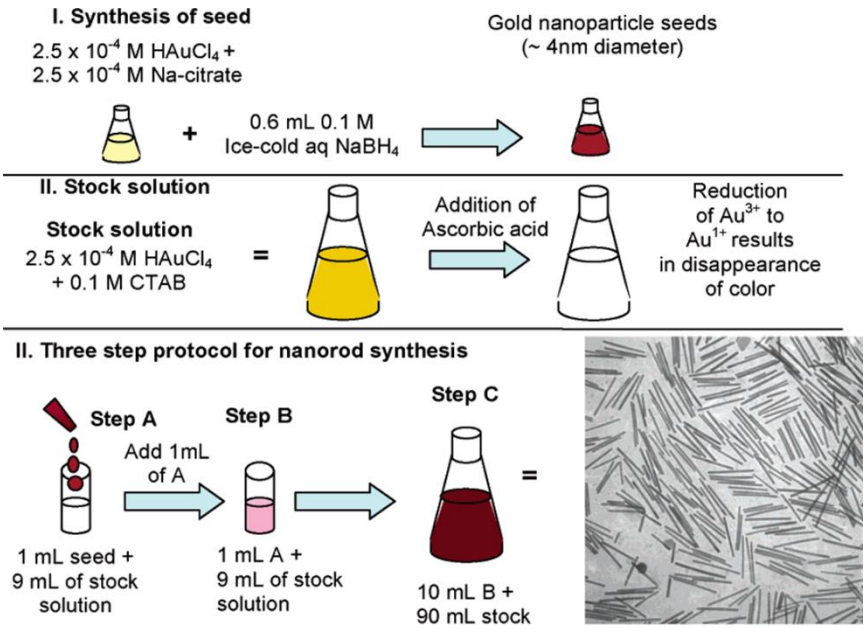

Figure 1.12. Seed-mediated growth approach to making gold and silver nanorods of controlled aspect ratio. Reprinted with permission from ref. 21. Copyright 2005 American Chemical Society.

ULSAN NATIONAL INSTITUTE OF SCIENCE AND TECHNOLOGY

1-3. Surface Modification of Nanoparticles

Inorganic and semiconductor nanomaterials have been widely applied due to the ability to interact with light or magnetic fields into broad application including fluorescence or magnetic resonance imaging (MRI)[22], X-ray imaging[23], Raman scattering[24], and drug delivery system (DDS)[25] with an external stimulus-responsive function. Among inorganic metal NPs, gold NP (Au NPs) have some advantages over other inorganic NP, such as simple synthesis with controlled sizes and shapes,[26-27] and biocompatibility due to the inertness. Because the biological applications of NPs usually require high colloidal stability and dispersibility in aqueous solution, modification of NP to endow these properties have been considered as an important issue. For example, the surface modification of Au NPs is simply achieved by the interaction between gold and thiol group. It can provide a variety of platforms for a drug delivery, including monolayers, layer by layer (LBL), and silica gel coating (Figure 1.5).[28]

Both strong anchoring of the surface ligands to the NP surface and the display of hydrophilic moieties are generally required to increase colloidal stability of NPs in water. For example, thiol and disulfide-derivatives have been employed to modify Au NPs because of their strong affinity with surface of inorganic NP. Typically, gold nanorods (Au NRs) are prepared using cationic surfactant bearing C16 alky molecules (cetyltrimethylammonium bromide (CTAB)). This molecule can non-covalently bind with surface of Au NRs, therefore, conjugation of peptides into surface of Au NRs can be hindered by remaining CTAB. On the other hand, C16 thiol molecules can be successfully attached, leading to the stable dispersion of NRs in aqueous solution.[29]

The dispersibility of NP in water can be improved by attaching the hydrophilic moieties to the ligand; for example, poly (ethylene glycol) (PEG), carboxylic acid, sulfonic acid, ammonium salt, and so on are the most popular functional molecules for surface modification. Additionally, charged moieties in NP provide much higher dispersibility in water than non-charged moieties. Grzybowsk et al. reported that Au NPs coated with two different charged ligands such as 11-mercaptohexadecyltrimethylammonium chloride as a cationic ligand and 11-mercaptoundecaoic acid as an anionic ligand are very stable under controlled pH (Figure 1.6a).[30] Generally, charge of NP is important in cellular uptake; for example, in NP,

ULSAN NATIONAL INSTITUTE OF SCIENCE AND TECHNOLOGY

positive charge allows for high absorption into cell because of high affinity for the cell membrane, and negative charge provide long circulation in the blood. Therefore, adjusting the balance between two charges is important through the surface modification and useful to extend their applications to responsive cellular uptake.

The use of polymer as a stabilizer in NPs has several advantages. For example, polymeric stabilizers provide longer stability than molecules, controlled solubility and balance between hydrophobic and hydrophilic properties, and various functionality of NPs. A variety of polymers have been reported to protect Au NPs against the aggregation. The modification with dithiol ligands, dihydrolopoic acid-based PEG ligands is efficient to provide high stability of NP (Figure 1.6b).[31] Moreover, such multidendate ligands of NPs also provide high stability in acidic and basic conditions or in high concentration of salt solution. The self-assembly method with NPs has been employed to facilitate stable, monodisperse and well-ordered NPs by using block copolymers. Kang et al. reported the core-shell Au NPs in the presence of PS-*b*-PAA copolymer.[32] Self-assembly behavior of PS-*b*-PAA in Au solution depends on the particle sizes, which can induce the polymer absorption into surface of NPs or dissolution of Au NPs into polymer shell (Figure 1.7a). In other approach, Schneider et al. modified the surface of NPs by oppositely charged polyelectrolytes through layer-by-layer (LbL) deposition to control the fluorescence property of NPs (Figure 1.7b).[33]

The synthesis of homogeneous NPs can be generally prepared via wet-chemical method, and further, the surface modification of NPs can provide higher colloidal stability and controlled hydrophilic/hydrophobic properties through ligand exchange. This process allows the NPs to be more applicable into broad application.

ULSAN NATIONAL INSTITUTE OF
SCIENCE AND TECHNOLOGY

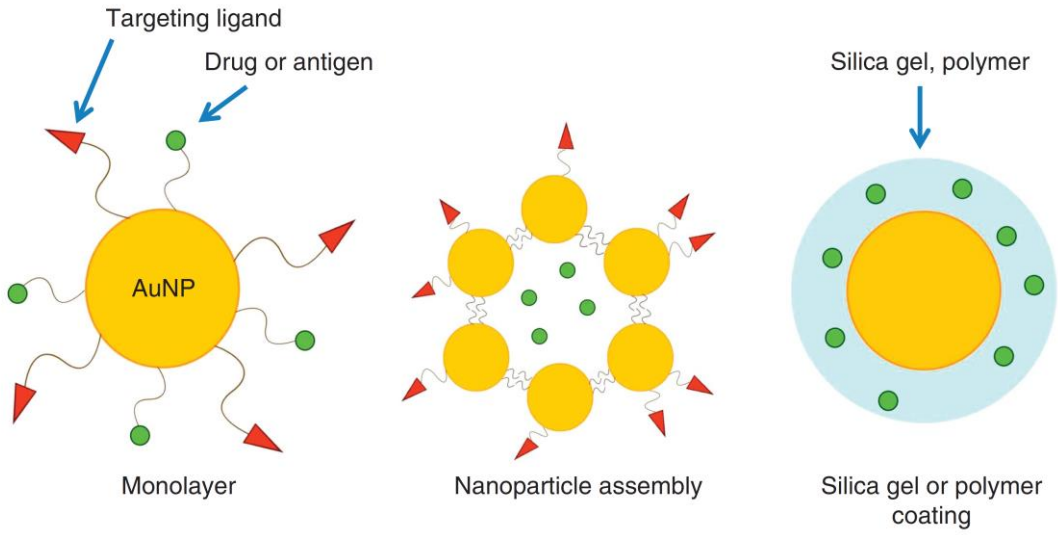

Figure 1.13. The surface modification of Au NPs in drug-delivery system carrier. Reprinted with permission from ref. 28. Copyright 2014 Nature Publishing Group

ULSAN NATIONAL INSTITUTE OF SCIENCE AND TECHNOLOGY

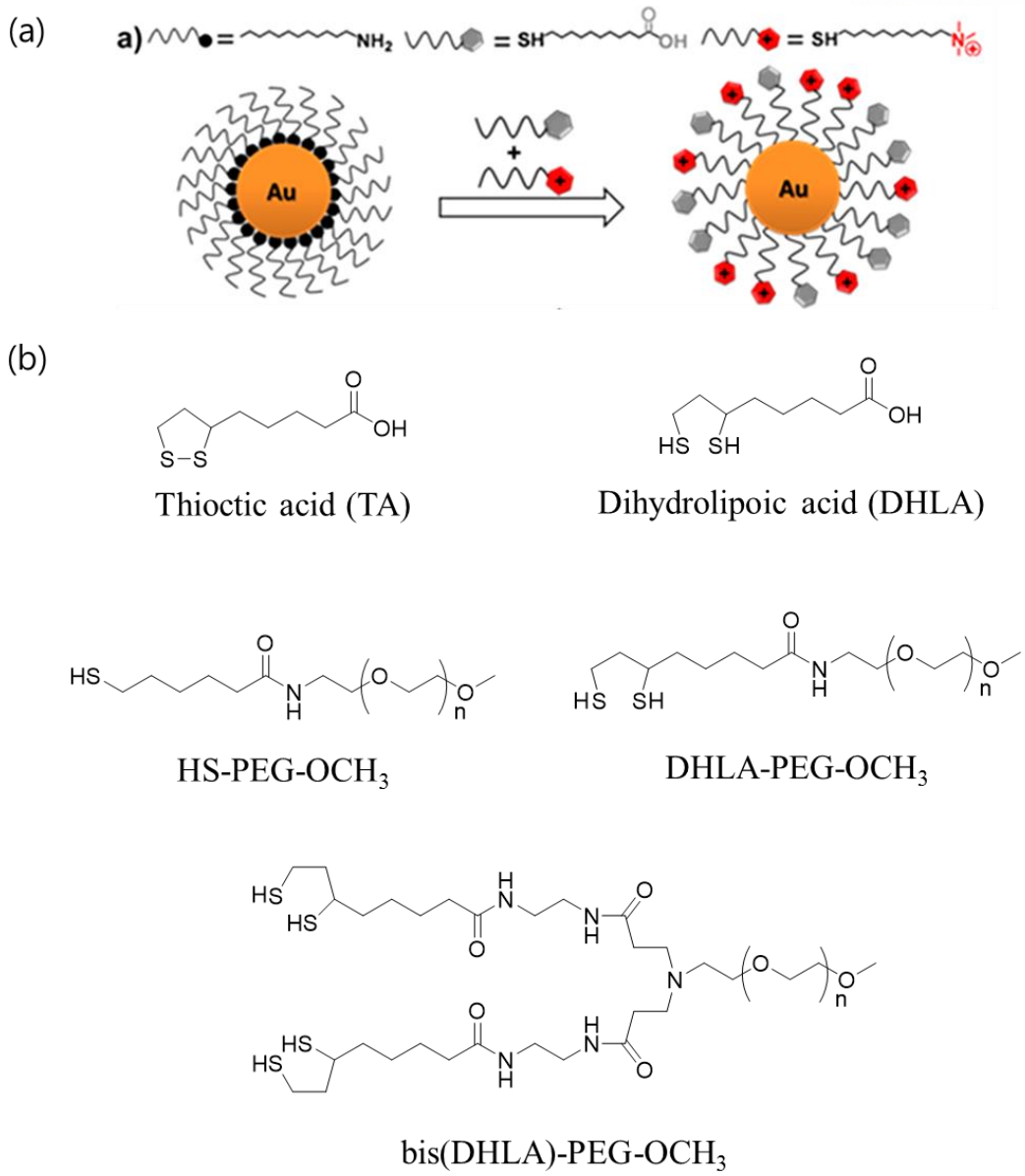

Figure 1.14. (a) Schematic description of a place-exchange reaction between dodecylamine (DDA)-functionalized Au NPs and a mixture of neutral 11-mercaptoundecanoic acid (MUA) and positively charged *N*,*N*,*N*-trimethyl(11-mercaptoundecyl)ammonium ion (TMA). Reprinted with permission from ref. 30. Copyright 2013 American Chemical Society. (b) A few examples of PEG-appended ligands together with the disulfide precursor. Reprinted with permission from ref. 31. Copyright 2010 American Chemical Society.

ULSAN NATIONAL INSTITUTE OF SCIENCE AND TECHNOLOGY

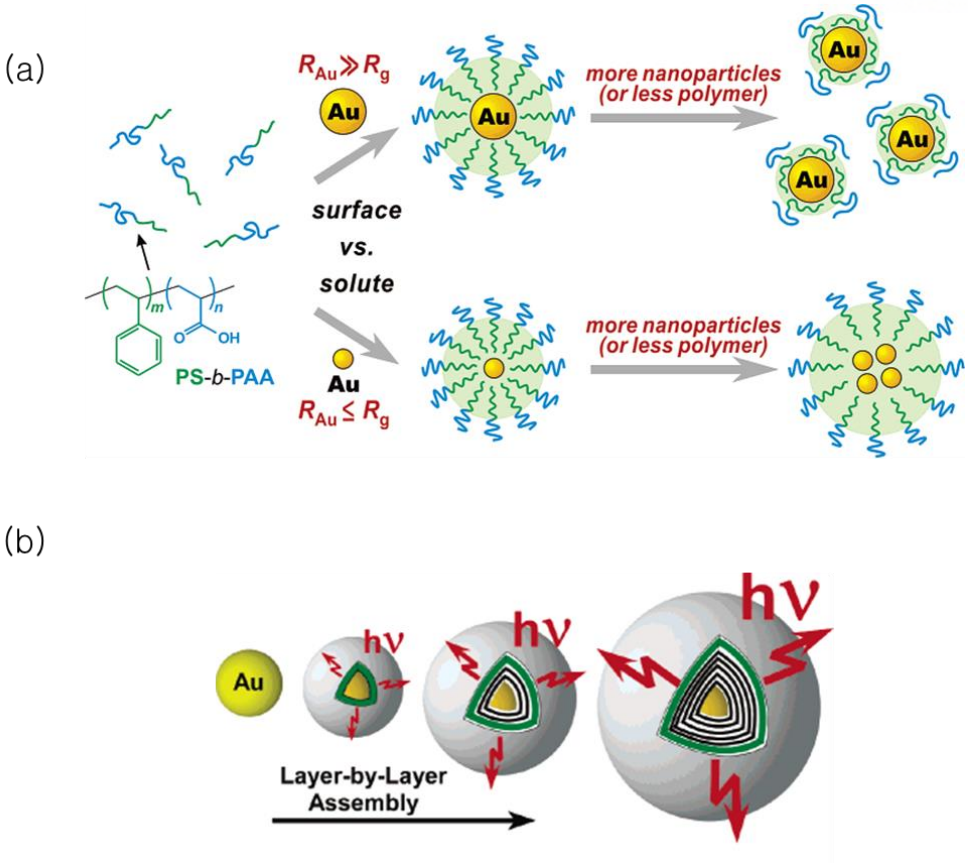

Figure 1.15. (a) Schematic representation of PS-*b*-PAA copolymer adsorption into pre-formed NPs with controlled sizes. Reprinted with permission from ref. 32. Copyright 2005 American Chemical Society. (b) Layer-by-Layer assembly for the construction of core-shell nanoparticle. Reprinted with permission from ref. 33. Copyright 2006 American Chemical Society.

ULSAN NATIONAL INSTITUTE OF SCIENCE AND TECHNOLOGY

1-4. Polymer Templated Nanoparticles

Numerous methods to synthesize the metal NPs have been reported using surfactants or polymeric ligands. As a potential material enable to be an alternative to the traditional surfactant in NP synthesis, (co)polymer show interesting opportunities for the formation of inorganic NPs with tunable size and shape, as well as for the stabilization of NPs by steric or ionic barriers around the NPs.[34-36] Among a variety of ways to achieve the synthesis of polymer-assisted NP, in situ synthesis of NP in polymer matrix by the reduction of the metal salts could be popular. For instance, Au NPs were obtained by the reflux of the Au precursor in the presence of NaOH,[37] and Au NPs are also prepared with poly(acrylamide) by the reducing agent, $NaBH_4$. Reduction of metal ions in the presence of polymers often uses the complexation of metal precursor with ligands, leading to metal NPs.

Linear amphiphilic block copolymer have been used as a template to synthesize functional NPs. Yonezawa et al. reported PVP-stabilized core-shell NPs by simultaneous alcohol reduction of the two metal salts. Yamauchi et al. demonstrated a triple-layered core-shell nanostructure consisting of Au core, Pd inner shell, and Pt outer shell by using Poly(ethylene oxide)-poly(propylene oxide)-poly(ethylene oxide) (PEO-PPO-PEO) block copolymers through one-pot process.[36] In terms of single NP, the synthesis of NPs using such copolymers comprises three main steps.[38] First, complexation of metal precursor with copolymer and formation of metal cluster is observed. Second, copolymer is absorbed on cluster, then additional complexation and reduction facilitate the formation of NPs. Third, pre-formed NPs can be grown into larger structure, which is protected by copolymer during the growth.

Zhiqun Lin group used a star-like block copolymer as nano-reactors.[39] They described star-like block copolymer could form unimolecular micelles that is structurally stable in organic or aqueous solution. This property can overcome the intrinsic instability of linear copolymer micelles induced by complexation with reactants. Additionally, this copolymer-based synthesis can provide monodisperse nanocrystals with desired composition and architecture. Based on the multi-arm star-like block copolymers, they can prepare a variety of metal and metal oxide NPs with controlled size and shape including single, core-shell, and hollow nanostructure. This unimolecular template

ULSAN NATIONAL INSTITUTE OF SCIENCE AND TECHNOLOGY

method enables the preparation of nearly monodisperse NPs with precisely tunable size and shape (Figure 1.8).

Recently, double hydrophilic block copolymer (DHBC) comprising both water-soluble, and chemically different functionalities have been stood out as an alternative to the conventional surfactant-based method.[39-41] all hydrophilic block copolymers show distinct property in water. For example, they can readily dissolve in aqueous solution and then induce polyion complexations with specific metal ions to form micellar aggregates. These materials can be used as nanoreactors with DHBCs for ionic substances, compared to the amphiphilic block copolymer micelles.[42] However, only a few studies by DHBCs as a template for NP synthesis have been reported due to the limitation of controlling size, shape, or morphology. In terms of NP synthesis, DHBCs are still challenging because micellization with inorganic materials and corresponding mineralization for the growth of NPs can be systemically designed by control of composition and molecular weight of each block, and architecture of structure, contributing to tunability of NPs.[42-43]

Therefore, in this thesis, we have investigated the how the each block of DHBC contribute to the interaction with inorganic materials, and different functional molecules of DHBC contribute to the size, shape, and morphology of resulting NPs. Furthermore, we have studied the broad applications of metal and metal NPs prepared by DHBCs.

ULSAN NATIONAL INSTITUTE OF SCIENCE AND TECHNOLOGY

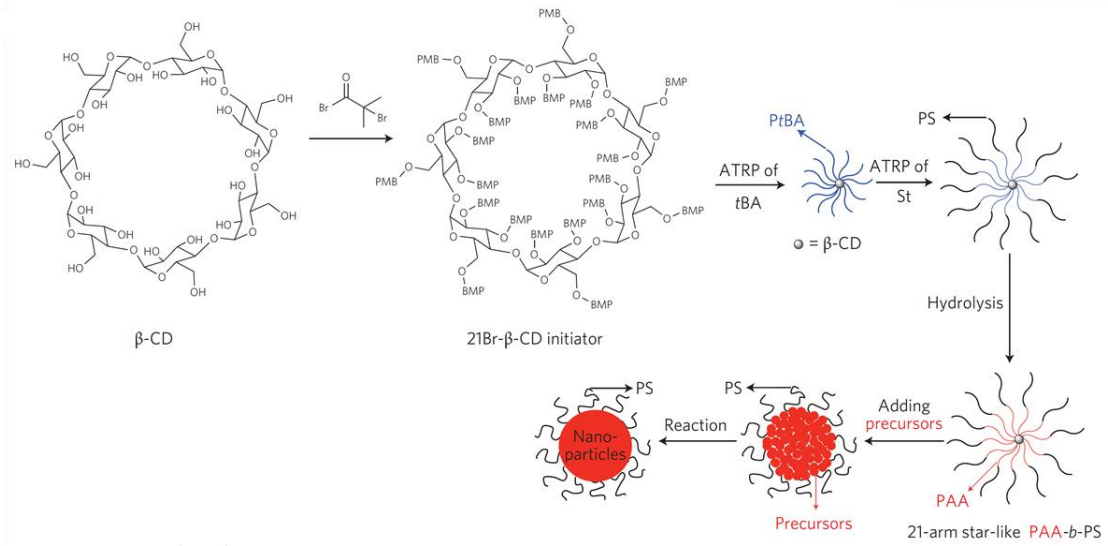

Figure 1.16. A star-like-polymer template strategy for the synthesis of monodispersed colloidal nanoparticles. Reprinted with permission from ref. 39. Copyright 2013 Nature Publishing Group

ULSAN NATIONAL INSTITUTE OF SCIENCE AND TECHNOLOGY

1-5. Overview of Thesis

This thesis, comprised of 5 chapters, describes synthesis of metal and metal oxide NPs using double hydrophilic block copolymer (DHBC), poly(ethylene oxide)-block-poly (acrylic acid) (PEO-b-PAA) as a template, and their applications.

Chapter 2 demonstrates typical synthetic route to prepare gold NP (Au NPs) using PEO-*b*-PAA copolymer. We confirmed that the metal precursor formed the micellar structure with polymer through the coordinative interaction in aqueous solution. This result facilitated the growth of spherical NPs with reducing agent.

In Chapter 3, we utilized two different functionalities of PEO-*b*-PAA copolymer to prepare core-shell type of nanostructure. Because of abundant electrons of PEO block, we could prepare the nanostructure of Au core and Ag shell (Au@Ag NPs) sequentially through the seed growth method. Control of shell thickness, and interparticle coupling to cluster-like shape could result in the transition of plasmonic properties. Such core-shell NPs were efficiently employed to enhance the performance of polymer solar cell.

In chapter 4, we investigated the effect of molecular weight of PAA block in PEO-b-PAA copolymer on the NP growth and the corresponding property, such as stability and size in NPs. Interesting results were demonstrated; for example, the change in the molecular weight of PAA block did not contribute to the size of NP. Additionally this result could contribute the stability of synthesized NPs. This assumption was experimentally demonstrated, but need more experiment or theoretical evidence to support the correlation between Mn and stability of NPs.

Chapter 5 extend our DHBC-templated method into synthesis of metal oxide NPs as well as metal NPs. The ruthenium oxide NPs (RuO_2) were successfully synthesized with PEO-*b*-PAA copolymer through electrostatic interaction. Through post-annealing process of as-prepared NPs, it is found that the crystallinity of NPs and transformation of DHBC can be controlled, enhancing the specific capacitance in supercapacitor.

1-6. Reference

(1) Daniel, M.-C.; Astruc, D., Gold Nanoparticles: Assembly, Supramolecular Chemistry, Quantum-Size-Related Properties, and Applications toward Biology, Catalysis, and Nanotechnology. *Chem. Rev.* **2004**, *104*, 293-346.

(2) Wang, Y.; Liu, Y.; Luehmann, H.; Xia, X.; Wan, D.; Cutler, C.; Xia, Y., Radioluminescent Gold Nanocages with Controlled Radioactivity for Real-Time in Vivo Imaging. *Nano Lett.* **2013**, *13*, 581-585.

(3) Ko, S.-J.; Choi, H.; Lee, W.; Kim, T.; Lee, B. R.; Jung, J.-W.; Jeong, J.-R.; Song, M. H.; Lee, J. C.; Woo, H. Y., Highly Efficient Plasmonic Organic Optoelectronic Devices Based on a Conducting Polymer Electrode Incorporated with Silver Nanoparticles. *Energy Environ. Sci.* **2013**, *6*, 1949-1955.

(4) Faraday, M., The Bakerian Lecture: Experimental Relations of Gold (and Other Metals) to Light. *Philos. Trans. R. Soc. Lond.* **1857**, *147*, 145-181.

(5) Tan, S. J.; Campolongo, M. J.; Luo, D.; Cheng, W., Building Plasmonic Nanostructures with DNA. *Nat. Nanotechnol.* **2011**, *6*, 268-276.

(6) Liu, R.; Duay, J.; Lee, S. B., Heterogeneous Nanostructured Electrode Materials for Electrochemical Energy Storage. *Chem. Commun.* **2011**, *47*, 1384-1404.

(7) Wiley, B. J.; Im, S. H.; Li, Z.-Y.; McLellan, J.; Siekkinen, A.; Xia, Y., Maneuvering the Surface Plasmon Resonance of Silver Nanostructures through Shape-Controlled Synthesis. *J. Phys. Chem. B* **2006**, *110*, 15666-15675.

(8) Kelly, K. L.; Coronado, E.; Zhao, L. L.; Schatz, G. C., The Optical Properties of Metal Nanoparticles: The Influence of Size, Shape, and Dielectric Environment. *J. Phys. Chem. B* **2003**, *107*, 668-677.

(9) Yang, X.; Yang, M.; Pang, B.; Vara, M.; Xia, Y., Gold Nanomaterials at Work in Biomedicine. *Chem. Rev.* **2015**, *115*, 10410-10488.

(10) Turkevich, J.; Stevenson, P. C.; Hillier, J., A Study of the Nucleation and Growth Processes in the Synthesis of Colloidal Gold. *Disc. Faraday Soc.* **1951**, *11*, 55-75.

(11) Frens, G., Controlled Nucleation for the Regulation of the Particle Size in Monodisperse Gold Suspensions. *Nature* **1973**, *241*, 20-22.

(12) Bethell, D.; Brust, M.; Schiffrin, D.; Kiely, C., From Monolayers to Nanostructured Materials: An Organic Chemist's View of Self-Assembly. *J. Electroanal. Chem.* **1996**,

ULSAN NATIONAL INSTITUTE OF SCIENCE AND TECHNOLOGY

409, 137-143.

(13) Brust, M.; Kiely, C. J., Some Recent Advances in Nanostructure Preparation from Gold and Silver Particles: A Short Topical Review. *Colloids Surf. A Physicochem. Eng. Asp.* **2002**, *202*, 175-186.

(14) Brust, M.; Walker, M.; Bethell, D.; Schiffrin, D. J.; Whyman, R., Synthesis of Thiol-Derivatised Gold Nanoparticles in a Two-Phase Liquid–Liquid System. *J. Chem. Soc., Chem. Commun.* **1994**, 801-802.

(15) Sun, L.; Crooks, R. M.; Chechik, V., Preparation of Polycyclodextrin Hollow Spheres by Templating Gold Nanoparticles. *Chem. Commun.* **2001**, 359-360.

(16) Templeton, A. C.; Wuelfing, W. P.; Murray, R. W., Monolayer-Protected Cluster Molecules. *Acc. Chem. Res.* **2000**, *33*, 27-36.

(17) Brust, M.; Fink, J.; Bethell, D.; Schiffrin, D.; Kiely, C., Synthesis and Reactions of Functionalised Gold Nanoparticles. *J. Chem. Soc., Chem. Commun.* **1995**, 1655-1656.

(18) Yee, C. K.; Jordan, R.; Ulman, A.; White, H.; King, A.; Rafailovich, M.; Sokolov, J., Novel One-Phase Synthesis of Thiol-Functionalized Gold, Palladium, and Iridium Nanoparticles Using Superhydride. *Langmuir* **1999**, *15*, 3486-3491.

(19) Jana, N. R.; Gearheart, L.; Murphy, C. J., Seeding Growth for Size Control of 5-40 Nm Diameter Gold Nanoparticles. *Langmuir* **2001**, *17*, 6782-6786.

(20) Jana, N. R.; Gearheart, L.; Murphy, C. J., Evidence for Seed-Mediated Nucleation in the Chemical Reduction of Gold Salts to Gold Nanoparticles. *Chem. Mater.* **2001**, *13*, 2313-2322.

(21) Murphy, C. J.; Sau, T. K.; Gole, A. M.; Orendorff, C. J.; Gao, J.; Gou, L.; Hunyadi, S. E.; Li, T., Anisotropic Metal Nanoparticles: Synthesis, Assembly, and Optical Applications. *J. Phys. Chem. B* **2005**, *109*, 13857-13870.

(22) Yoo, D.; Lee, J.-H.; Shin, T.-H.; Cheon, J., Theranostic Magnetic Nanoparticles. *Acc. Chem. Res.* **2011**, *44*, 863-874.

(23) Zhou, C.; Long, M.; Qin, Y.; Sun, X.; Zheng, J., Luminescent Gold Nanoparticles with Efficient Renal Clearance. *Angew. Chem.* **2011**, *123*, 3226-3230.

(24) Qian, X.; Peng, X.-H.; Ansari, D. O.; Yin-Goen, Q.; Chen, G. Z.; Shin, D. M.; Yang, L.; Young, A. N.; Wang, M. D.; Nie, S., In Vivo Tumor Targeting and Spectroscopic Detection with Surface-Enhanced Raman Nanoparticle Tags. *Nat. Biotechnol.* **2008**, *26*, 83-90.

ULSAN NATIONAL INSTITUTE OF SCIENCE AND TECHNOLOGY

(25) Mura, S.; Nicolas, J.; Couvreur, P., Stimuli-Responsive Nanocarriers for Drug Delivery. *Nat. Mater.* **2013**, *12*, 991-1003.

(26) Personick, M. L.; Mirkin, C. A., Making Sense of the Mayhem Behind Shape Control in the Synthesis of Gold Nanoparticles. *J. Am. Chem. Soc.* **2013**, *135*, 18238-18247.

(27) Sau, T. K.; Murphy, C. J., Room Temperature, High-Yield Synthesis of Multiple Shapes of Gold Nanoparticles in Aqueous Solution. *J. Am. Chem. Soc.* **2004**, *126*, 8648-8649.

(28) Kobayashi, K.; Wei, J.; Iida, R.; Ijiro, K.; Niikura, K., Surface Engineering of Nanoparticles for Therapeutic Applications. *Polym. J.* **2014**, *46*, 460-468.

(29) Colombo, M.; Mazzucchelli, S.; Collico, V.; Avvakumova, S.; Pandolfi, L.; Corsi, F.; Porta, F.; Prosperi, D., Protein-Assisted One-Pot Synthesis and Biofunctionalization of Spherical Gold Nanoparticles for Selective Targeting of Cancer Cells. *Angew. Chem. Int. Ed.* **2012**, *51*, 9272-9275.

(30) Pillai, P. P.; Huda, S.; Kowalczyk, B.; Grzybowski, B. A., Controlled pH Stability and Adjustable Cellular Uptake of Mixed-Charge Nanoparticles. *J. Am. Chem. Soc.* **2013**, *135*, 6392-6395.

(31) Stewart, M. H.; Susumu, K.; Mei, B. C.; Medintz, I. L.; Delehanty, J. B.; Blanco-Canosa, J. B.; Dawson, P. E.; Mattoussi, H., Multidentate Poly(ethylene glycol) Ligands Provide Colloidal Stability to Semiconductor and Metallic Nanocrystals in Extreme Conditions. *J. Am. Chem. Soc.* **2010**, *132*, 9804-9813.

(32) Kang, Y.; Taton, T. A., Controlling Shell Thickness in Core-Shell Gold Nanoparticles Via Surface-Templated Adsorption of Block Copolymer Surfactants. *Macromolecules* **2005**, *38*, 6115-6121.

(33) Schneider, G.; Decher, G.; Nerambourg, N.; Praho, R.; Werts, M. H.; Blanchard-Desce, M., Distance-Dependent Fluorescence Quenching on Gold Nanoparticles Ensheathed with Layer-by-Layer Assembled Polyelectrolytes. *Nano Lett.* **2006**, *6*, 530-536.

(34) Mistark, P. A.; Park, S.; Yalcin, S. E.; Lee, D. H.; Yavuzcetin, O.; Tuominen, M. T.; Russell, T. P.; Achermann, M., Block-Copolymer-Based Plasmonic Nanostructures. *ACS Nano* **2009**, *3*, 3987-3992.

(35) Shin, D. O.; Mun, J. H.; Hwang, G.-T.; Yoon, J. M.; Kim, J. Y.; Yun, J. M.; Yang, Y.-B.; Oh, Y.; Lee, J. Y.; Shin, J., Multicomponent Nanopatterns by Directed Block

ULSAN NATIONAL INSTITUTE OF SCIENCE AND TECHNOLOGY

Copolymer Self-Assembly. *ACS Nano* **2013**, *7*, 8899-8907.

(36) Wang, L.; Yamauchi, Y., Autoprogrammed Synthesis of Triple-Layered Au@Pd@Pt Core-Shell Nanoparticles Consisting of a Au@Pd Bimetallic Core and Nanoporous Pt Shell. *J. Am. Chem. Soc.* **2010**, *132*, 13636-13638.

(37) Hirai, H.; Nakao, Y.; Toshima, N., Preparation of Colloidal Transition Metals in Polymers by Reduction with Alcohols or Ethers. *J. Macromol. Sci., Chem.* **1979**, *13*, 727-750.

(38) Sakai, T.; Alexandridis, P., Mechanism of Gold Metal Ion Reduction, Nanoparticle Growth and Size Control in Aqueous Amphiphilic Block Copolymer Solutions at Ambient Conditions. *J. Phys. Chem. B* **2005**, *109*, 7766-7777.

(39) Pang, X.; Zhao, L.; Han, W.; Xin, X.; Lin, Z., A General and Robust Strategy for the Synthesis of Nearly Monodisperse Colloidal Nanocrystals. *Nat. Nanotechnol.* **2013**, *8*, 426-431.

(40) Bastakoti, B. P.; Guragain, S.; Yusa, S.-i.; Nakashima, K., Novel Synthesis Route for Ag@SiO_2 Core–Shell Nanoparticles Via Micelle Template of Double Hydrophilic Block Copolymer. *RSC Adv.* **2012**, *2*, 5938-5940.

(41) Bastakoti, B.; Sukegawa, H.; Wu, K. C.-W.; Yamauchi, Y., Synthesis of Porous Iron Oxide Microspheres by a Double Hydrophilic Block Copolymer. *RSC Adv.* **2014**, *4*, 9986-9989.

(42) Nakashima, K.; Bahadur, P., Aggregation of Water-Soluble Block Copolymers in Aqueous Solutions: Recent Trends. *Adv. Colloid Interface Sci.* **2006**, *123*, 75-96.

(43) Cölfen, H., Double-Hydrophilic Block Copolymers: Synthesis and Application as Novel Surfactants and Crystal Growth Modifiers. *Macromol. Rapid Commun.* **2001**, *22*, 219-252.

ULSAN NATIONAL INSTITUTE OF SCIENCE AND TECHNOLOGY

Chapter 2.

Double Hydrophilic Block Copolymer Templated Au Nanoparticles with Enhanced Catalytic Activity toward Nitroarene Reduction

2.1. Introduction

The development of metal nanostructures has been intensively pursued over several decades for their fundamental scientific interests and technological importance in various applications.[1-5] Among noble metals, gold nanoparticles (Au NPs) have been the subject of intense investigation due to their broad applicability in biomedicine, catalysis and biosensing. Numerous approaches to prepare Au NPs in various sizes and morphologies have been reported including citrate reduction, Brust's two-phase method, seed growth method, thermolysis of metal precursors and template synthesis with micelles and surfactants.[6-14]

In many of these approaches, control over the particle size and morphology was achieved by either using templating materials or capping agents during the growth of NPs. For example, small organic molecules or polymers are widely used as soft templates to form stable Au nanostructures without the aggregation of NPs. Murphy and co-workers reported that spherical Au NPs were successfully synthesized using citric acid as both capping and reducing agents. The size of as-prepared Au NPs using citric acid can even be tuned further by the seed growth method.[10, 15, 16] Block copolymers have recently

***** Chapter 2 is reproduced in part with permission of *"Seo, E.; Kim, J.; Hong, Y.; Kim, Y. S.; Lee, D.; Kim, B.-S., J. Phys. Chem. C 2013, 117, 11686−11693*." Copyright 2013 American Chemical Society.

ULSAN NATIONAL INSTITUTE OF SCIENCE AND TECHNOLOGY

emerged as versatile templates for synthesizing inorganic NPs because they allow for control over the size and shape of NPs and also direct the spatial patterning of NPs on the surface owing to their self-assembly capability. Toward that end, most block copolymer self-assembly approaches rely on the use of entirely hydrophobic or amphiphilic block copolymers, inevitably necessitating the use of organic solvents for synthesis and subsequent utilization. Considering that a number of applications such as waste-water treatment require the dispersion of heterogeneous catalysts in aqueous solutions and that water is by far the most environmentally friendly medium, it is crucial to develop polymer templates that will enable synthesis and stabilization of NPs in aqueous media.

In this context, double hydrophilic block copolymers (DHBCs), which consist of two chemically distinct hydrophilic segments, offer a unique alternative to the existing methods. The synthesis of metal NPs using DHBCs presents a straightforward and versatile method to produce metal nanostructures under mild aqueous conditions without the use of organic solvents or thermal treatment.[17, 18] From an environmental point of view, water provides numerous advantages over organic solvents as a reaction medium with its fast reaction rate, high yield, and non-toxicity.

Herein, we report the synthesis of Au NPs using a DHBC as a soft template to produce NPs with a superior aqueous stability and investigate their potential as catalysts for the reduction of a series of nitroarenes in aqueous solutions. Specifically, the DHBC, poly(ethylene oxide)-*block*-poly(acrylic acid) (PEO-*b*-PAA), is employed to form a micelle upon the addition of a gold precursor, $HAuCl_4 \cdot 3H_2O$, which is subsequently converted to Au NPs with the addition of a reducing agent. Au NPs with a proper size distribution are subsequently prepared by a simple centrifugation process. Furthermore, we find that Au@DHBC NP is a highly effective catalyst in the reduction of a series of nitroarenes. Remarkably, it is shown that the turnover frequency (TOF) reaches 800 h^{-1} in 4-nitrophenol reduction using the Au@DHBC NP catalyst. This DHBC-based method provides a simple synthetic procedure that produces hybrid Au NPs with outstanding performance in catalytic reactions. Because the self-assembly process (i.e., micellization) is driven by the simple coordinative bonding between Au precursor and carboxylate group of PAA block, we anticipate that this DHBC-based method will provide a facile and general means in the synthesis of other NPs for a variety of applications.

ULSAN NATIONAL INSTITUTE OF SCIENCE AND TECHNOLOGY

2.2. Experimental Section

Materials and chemicals. Gold(III) chloride trihydrate ($HAuCl_4 \cdot 3H_2O$), hydrazine (NH_2NH_2), 4-nitroarenes and sodium borohydride were purchased from Aldrich and used without further purification. Double hydrophilic block copolymer of PEO(5000)-*b*-PAA(6700) was purchased from Polymer Source, Inc.

Synthesis of Au@DHBC NPs. The gold nanoparticles with double hydrophilic block copolymer shell were prepared according to the following protocols. First, double hydrophilic block copolymer PEO(5000)-*b*-PAA(6700) (25.12 mg, 0.20 mmol of carboxylic acid groups) was dissolved under vigorous stirring in 50.0 mL of deionized water, followed by adding 0.1 mL of 4.0 M NaOH (0.40 mmol, 2 equiv. to carboxylic acid groups in PAA block). To this solution mixture, $HAuCl_4 \cdot 3H_2O$ (26.2 mg, 0.067 mmol) was mixed. Subsequently, 0.1 mL of 10.0 M hydrazine (1.0 mmol) was added to the resulting suspensions under vigorous stirring. Immediately following the addition of hydrazine, the solution underwent a color change from transparent yellow to turbid orange. After 30 min of vigorous stirring, the solution mixture was centrifuged to remove large aggregates of NPs (3197 xg, 15 min), and then, the transparent reddish supernatant was dialyzed against deionized water using a dialysis membrane (MWCO 12000 – 14000, SpectraPore) for 3 days to remove any byproducts and residuals. The prepared suspension of Au NPs exhibited a fairly good colloidal stability that lasted more than 6 months without any precipitation.

Synthesis of Pd@DHBC and Pt@DHBC NPs. The palladium and nanoparticles with double hydrophilic block copolymer shell were synthesized by following protocols. First, double hydrophilic block copolymer PEO(5000)-*b*-PAA(6700) (25.12 mg, 0.20 mmol of carboxylic acid groups) was dissolved under vigorous stirring in 50.0 mL of deionized water, followed by adding 0.1 mL of 4.0 M NaOH (0.40 mmol, 2 equiv. to carboxylic acid groups in PAA block). To this solution mixture, Na_2PdCl_4 (0.1 mmol) (or 0.1 mmol of K_2PtCl_4 for Pt@DHBC NPs) was mixed. Subsequently, 1.0 M $_L$-ascorbic acid (AA) (1.0 mL, 1.0 mmol) was added to the resulting suspensions under vigorous stirring. Immediately following the addition of AA, the solution underwent a color change from transparent brown to black. After 30 min of vigorous stirring, the solution mixture was centrifuged to remove large aggregates of nanoparticles (4000 rpm, 15 min), and then,

ULSAN NATIONAL INSTITUTE OF SCIENCE AND TECHNOLOGY

the recovered supernatant was dialyzed against deionized water using a dialysis membrane (MWCO 12000 – 14000, SpectraPore) for 3 days to remove any byproducts and residuals.

Reduction of nitroarenes. To an aqueous solution of 7.50×10^{-4} M of nitroarene (0.5 mol% with respect to the gold concentration), 0.566 mL of 6.63×10^{-5} M Au@DHBC NP catalyst was slowly added. To this mixture, 1.0 mL of 2.22 M $NaBH_4$ solution (300 equiv. of substrate, 99%, Aldrich) was added until the deep yellow solution became colorless. The yellow color of the solution gradually vanished, indicating the reduction of 4-nitrophenol. The reaction progress was checked periodically by assessing a small portion of the reaction mixture at a regular time interval.

Characterizations. The morphology, size, and size distribution of the prepared Au NPs were investigated using a transmission electron microscopy (TEM, JEOL JEM-2100, accelerating voltage of 200 kV, Gatan CCD camera). The absorbance of the Au NPs and the concentration of nitroarenes were characterized by using UV/vis spectroscopy (Shimadzu UV-1800). The concentration of Au NPs was measured using ICP-OES (720-ES, Varian). Thermogravimetric analysis (TGA) was conducted in air atmosphere at a heating rate of 10 ^{o}C/min using a thermogravimetric analyzer (Q200, TA Instrument). Fourier-transform infrared (FT-IR) spectra were obtained with a FT-IR spectrophotometer (Varian). Size distribution analysis was studied using dynamic light scattering (DLS, Nano ZS, Malvern, U.K., and BI-APD, Brookhaven Instrument, New York, U.S.A.).

ULSAN NATIONAL INSTITUTE OF SCIENCE AND TECHNOLOGY

2.3. Results and Discussion

The synthesis of Au NPs using a DHBC as a template is illustrated in Scheme 2.1. Traditionally, DHBCs have been employed in the controlled growth of inorganic minerals, such as $CaCO_3$, $BaSO_4$, and $Ca_3(PO_4)_2$, with unusual structural complexity in aqueous solutions;[19, 20] however, there are only a few examples of employing PEO-*b*-PAA DHBCs in the controlled synthesis of metal NPs.[18, 21, 22]

In our approach, we use the DHBC, PEO-*b*-PAA as our template and stabilizer for Au NP synthesis. While the carboxylate group of PAA block provides a site that can interact with metal precursors, the PEO block acts as a stabilizer for the controlled synthesis of Au NPs. Upon introducing Au precursor ($HAuCl_4$) that preferentially interacts with the carboxylate of PAA block by ligand exchange, the PAA blocks segregate to form micellar aggregates in solution. Although we have previously shown that Cu and RuO_2 NPs can be synthesized using a similar DHBC approach based on the electrostatic interactions between cationic metal ions (i.e., Cu^{2+} and Ru^{3+}) and the carboxylate group of PAA, it should be noted that the method presented in this study is somewhat counterintuitive because the Au precursor dissociates into anionic $AuCl_4^-$, which unlikely interacts with PAA through electrostatic interactions. Nevertheless, the selective interaction between the carboxylate (COO^-) group in PAA block and the Au metal precursor can be carefully confirmed using FT-IR spectroscopy (Figure 2.1). Pure PEO-*b*-PAA shows C=O stretching vibration of the carboxylic acid group at 1729 cm^{-1} and C-O stretching vibration of the PAA block and the PEO block at 1242 and 1091 cm^{-1}, respectively (Figure 2.1a). Upon introduction of NaOH, the carboxylic acid groups of the PAA block deprotonate, as evidenced by the appearance of asymmetric and symmetric stretching vibration of the carboxylate (COO^-) groups in the PAA block at 1563 and 1429 cm^{-1}, respectively (Figure 2.1b). After the addition of the Au metal precursor, the peak at 1429 cm^{-1} is considerably diminished due to the strong coordinative complexation between the Au precursor and the carboxylate groups. A previous report has shown that carboxylate groups in citric acid can displace with the Cl^- ligand of $AuCl_4^-$ anions.[23] In addition, the disappearance of peaks observed in the carboxylate group was shown to indicate the formation of Au(III)-O bond with COO^- group of PAA block,[24] which is in good agreement with our results.

ULSAN NATIONAL INSTITUTE OF SCIENCE AND TECHNOLOGY

The coordination modes formed between the metal precursor and the carboxylate groups of DHBC can be further confirmed by analyzing the FT-IR spectrum in Figure 1c. In general, the metal carboxylate coordination modes can be determined by the position and separation (Δ) of carboxylate bands in the 1300 – 1700 cm^{-1}; for example, the unidentate mode (Δ > 200 cm^{-1}), bidentate mode (Δ > 110 cm^{-1}), and bridging mode (140 < Δ < 200 cm^{-1}) can be identified by the separation between two characteristic bands of the carboxylate groups.[25, 26] The separation (Δ) between the two carboxylate groups at 1563 and 1409 cm^{-1} in Figure 2.1c corresponds to the bridging mode. Additionally, the separation between the two carboxylate bands at 1563 and 1453 cm^{-1} can be assigned a bidentate coordination mode; however, it is not clearly discernible as the peak at 1453 cm^{-1} is overlapped with a scissoring band of methylene group ($-CH_2-$) in the polymer. Therefore, Au precursor can interact with carboxylate group by coordinative bond mainly with a bridging mode (Figure 2.1). Furthermore, the peak at 1099 cm^{-1} from the ether group (C–O–C) in the PEO block remains unchanged, suggesting that the preferential interaction between PAA and the metal precursor is dominant as illustrated in Scheme 1. These selective coordinative interactions induce the DHBCs to form the micellar aggregates of approximately 4.4 nm in size as determined by dynamic light scattering (DLS) (Figure 2.2). In our previous reports, the triggered formation of micellar aggregates with a similar core–shell type structure was proposed with other metal ions such as Cu^{2+} and Ru^{3+} that formed complexes with DHBCs.[17, 18]

Once their formation is induced, the PEO-*b*-PAA micelle acts as a nanoreactor to template the growth of a NP within the micellar core upon the addition of a reducing agent, N_2H_4. When N_2H_4 is added to the mixture to induce simultaneous nucleation and growth of NPs, the solution turns from transparent yellow to turbid red, signaling the formation of Au NPs within the DHBC template. Centrifuge cycles are performed immediately after reducing the Au precursor to remove unwanted aggregates as well as to obtain NPs with a proper size distribution and an appropriate concentration. The prepared suspension of Au@DHBC NPs remains stable for several months without noticeable aggregation because the PEO block sterically stabilizes the NPs in aqueous solution (Figure 2.3d). In clear contrast, a homopolymer of PAA with a similar molecular weight, does not yield such a stable suspension of NPs, which highlights the important role of the PEO block in stabilizing the resulting Au NPs.[17]

ULSAN NATIONAL INSTITUTE OF SCIENCE AND TECHNOLOGY

The morphology and structure of the synthesized Au@DHBC NPs are characterized with transmission electron microscopy (TEM) and UV/vis spectroscopy (Figure 2.3). The TEM images of the synthesized Au NPs show a spherical morphology (Figure 2.3a-b) with an average diameter of 10.0 ± 4.0 nm averaged over 100 NPs (Figure 2.3c) after centrifuge to remove large aggregates (Figure 2.4). High-resolution TEM further in Figure 2.3b reveals that Au NPs have a crystalline lattice fringe of 0.204 nm (yellow mark) and 0.236 nm (green mark), corresponding to the primary reflection of the (200) and (111) lattice of Au, respectively.

The characteristic surface plasmon resonance (SPR) peak of Au@DHBC NPs is also observed at 533 nm, which is slightly red-shifted when compared to that of other Au NPs with a similar diameter dispersed in an aqueous medium. In general, the Mie theory suggests that an increase in the refractive index of the medium red-shifts the SPR peak of Au NPs.[27] Thus, the red-shift likely originates from the high refractive index (n_{PAA} = 1.418) of the PAA block surrounding the Au@DHBC NPs (the refractive index of a typical aqueous solution, n_{H2O} = 1.333), suggesting the formation of core-shell type Au NPs surrounded by the DHBC template. We note that due to the low electron density of the DHBC, the presence of the PEO-*b*-PAA surrounding the Au NPs cannot be directly investigated under TEM. Thus, Au@DHBC NPs are analyzed using DLS to verify the existence of a thin PEO-*b*-PAA shell. The DLS measurement yields an average diameter of 13.97 nm, which is slightly larger than that observed under TEM, indicating the presence of a thin shell of DHBC surrounding the Au NPs (Figure 2.2). We also investigate ways to control the size of Au NPs by varying the amount of Au precursor at a fixed concentration of DHBC, as well as varying the type of reductant (Figure 2.5 and 2.6). The size of Au NPs is decreased with lowering the concentration of the Au precursor at a fixed polymer concentration, albeit with a relatively broad size distribution.

The thermal stability as well as the relative composition of the DHBC in the synthesized Au@DHBC NPs is estimated based on the thermogravimetric analysis (TGA) (Figure 2.7). As shown in the TGA curve of Au@DHBC NPs, an initial mass loss of water at around 57.8 ^{o}C is observed. Following the initial loss of water, the second precipitous drop in mass begins at around 230 ^{o}C, which is associated with the degradation of the DHBCs. Characteristic peaks in the range of 230 – 613 ^{o}C are observed in the differential TGA curve, which can be attributed to the degradation of PEO-*b*-PAA.

ULSAN NATIONAL INSTITUTE OF SCIENCE AND TECHNOLOGY

Interestingly, in accord with the FT-IR data, TGA also indicates that the specific interactions between the polymer and the metal precursor increase the degradation temperature of the DHBCs from 530 to 613 ^{o}C. Finally, the subsequent weight loss corresponds to the conversion of the residual DHBCs into an amorphous carbonaceous layer around Au NPs, of which mass fraction is deduced to be approximately 16% of Au NPs present within the DHBC template. Furthermore, a residual polymeric layer is found around the aggregated Au NPs after thermal treatment (Figure 2.8).

We test the utility of Au@DHBC NPs in the catalytic reduction of a series of nitroarenes. Nitroarenes are a class of toxic and poisonous chemicals; as such, there have been active efforts to develop methods to decompose nitroarenes, including physical, biological, and chemical techniques.[28] In particular, catalytic reduction of nitroarenes using various nanostructured materials has been demonstrated with its synthetic utility and mild reaction conditions. For example, hollow Au nanostructures, bimetallic Pt and Pd, and hybrid NPs on a support have been demonstrated to be effective in the reduction of nitroarenes.[29-33]

In order to evaluate the efficiency of the Au@DHBC NP as a catalyst, we first employ the reduction of 4-nitrophenol to 4-aminophenol in the presence of a hydrogen source, $NaBH_4$ (Figure 2.9). Initially, the 4-nitrophenol solution has a light yellow color, which turns dark yellow upon the addition of $NaBH_4$ due to the formation of 4-nitrophenolate (Figure 2.10). However, with the use of Au@DHBC NPs, the dark yellow color gradually fades away with the progression of the reduction to 4-aminophenol. The kinetics of the reaction can be periodically monitored using UV/vis spectroscopy measurements. Specifically, the absorption of 4-nitrophenol at 400 nm rapidly decreases with a concomitant increase in the peak at 300 nm, which can be attributed to the production of 4-aminophenol (Figure 2.9b). The isosbestic point between the two peaks is also observed, suggesting that the two principal species are responsible for the conversion reaction. Based on the UV/vis spectra, therefore, the pseudo-first-order reaction kinetic is applied to determine the reaction rate constant, k, for the reaction. We also conduct several control experiments to determine the optimum reaction condition of the Au@DHBC NP catalyst. In addition, we vary the concentration of catalyst and reductant while keeping the reaction temperature constant. From the linear relations of $\ln(C_t/C_o)$ with time, we find that the rate constant, k, at 30 ^{o}C to be 0.029, 0.117, 0.333, and 0.768 min^{-1} with different

ULSAN NATIONAL INSTITUTE OF SCIENCE AND TECHNOLOGY

concentrations of catalyst and reductant (Figure 2.9c). These results are all comparable or superior to those reported previously, which are in the range of 10^{-1} to 10^{-3} min^{-1} under similar reaction conditions, indicating a high catalytic activity of Au@DHBC NP prepared with the DHBC template.[34] In terms of turnover frequency (TOF), which correlates the degree of reaction per unit time with the amount of catalyst used during the reaction, the 0.5 mol% Au NPs with 300 equiv. $NaBH_4$ yielded the optimal catalytic activity among all samples tested. Interestingly, it is noted that Au NP catalyst with the DHBC shell (TOF of 800 h^{-1}) displays a superior catalytic activity in the reduction of 4-nitrophenol to that of Au NPs prepared by citrate reduction (TOF of 570 h^{-1}) with a similar diameter of 10.7 ± 4.3 nm (Figure 2.11). This observation suggests that not only the core Au NPs, but also the surrounding DHBCs are playing a critical role in the enhancement of the reaction efficiency. In concert with our observation, Crooks and co-workers have previously observed enhanced catalytic activity of metal NPs synthesized within dendrimer templates.[35-37] They attributed that the dendrimer encapsulated NPs could exhibit an enhanced catalytic efficiency due to the confinement effect within the sterically confined dendrimer core. In addition, it was presented that dendrimer could serve as a selective gate to permit small molecule reactants to be located near the catalytic NPs for efficient reaction.[38] When compared to other reports which used amphiphilic block copolymers to make Au NPs, the Au@DHBC NPs exhibit a greater catalytic activity. This value is comparable to the recent study by Chen and co-workers, which showed that Au catalysts coated with an amphiphilic block copolymer, polystyrene-*block*-poly(4-vinyl pyridine) (PS-*b*-P4VP), results in a TOF value of 443 h^{-1} in 4-nitrophenol reduction.[39] Moreover, the catalytic activity of Au@DHBC NP is comparable to the catalytic activity of hybrid composites such as Au-graphene, which was previously reported by our group, demonstrating a TOF value of 400 h^{-1}, or Au-carbon nanotube, investigated by Li and co-workers, reporting a TOF value of 35 h^{-1} of TOF in 4-nitrophenol reduction. Both graphene and carbon nanotube are used as a support to increase the efficiency and stability of catalysts; thus, highlighting the excellence of Au@DHBC NP as a catalyst.[29, 30] In other example, Jin et al. reported synthesis of various metal NPs loaded oxide microspheres and their application as a catalyst.[40] Although catalytic efficiency of Au NPs loaded TiO_2 is much higher (TOF > 4800), it has to be considered that Au NPs supported by porous oxide are synthesized with different

ULSAN NATIONAL INSTITUTE OF SCIENCE AND TECHNOLOGY

synthetic approach. Furthermore, it is scarcely applied as the general tool to prepare the catalysts because only Au NPs loaded TiO_2 supports show high efficiency except for Au NPs loaded other oxide supports in the reduction of 4-NP. On the other hand, though the catalytic activity of Au@DHBC NPs for the reduction of 4-NP is lower, it is remarkable that catalytic activities of Au@DHBC NPs for the reduction of a series of nitroarenes (i.e. TOF = 4000 in the catalytic reduction of 3-nitroaniline) show high efficiency.

The reduction of 4-nitrophenol to 4-aminophenol is known to be thermodynamically favorable with a standard reduction potential of -0.76 V with a use of hydrogen source of $NaBH_4$ that possesses the reduction potential of -1.33 V. 4-nitrophenol nevertheless does not spontaneously reduce due to the high activation energy of this reaction. In agreement with this argument, we find that the peak at 400 nm indicating the concentration of 4-nitrophenol does not change for days without a catalyst (Figure 2.12). We also find that the reaction rate is quite sensitive to temperature. Thus, by carrying out the identical reaction at different temperatures, the activation energy of the reaction is determined to be 31.2 kJ mol^{-1} according to the Arrhenius plot (Figure 2.9d).

We further investigate the catalytic activity of Au@DHBC NPs for the reduction of a series of other nitroarene derivatives (Table 2.1). Here, we choose to run the reactions in the optimized condition of 0.5 mol% of catalyst with 300 equiv. of $NaBH_4$ to clearly monitor the conversion efficiency of the reaction. As shown in Table 1, we find that our Au@DHBC NPs exhibit high reactivity with excellent yields toward a series of model nitroaniline and nitrophenol compounds regardless of the types and position of the substituents. Interestingly, when the reduction of 4-, 3-, and 2-nitrophenols (or nitroanilines) is catalyzed by Au@DHBC NPs, the 3-nitrophenol (or nitroaniline) shows a better catalytic activity than 4- or 2-nitrophenols (or nitroanilines). For example, the remarkable TOF in Entry 5 is as high as 4000 h^{-1}, calculated based on the moles of nitroarene converted per mole of the Au NP catalyst per 1 h under the present reaction condition.

Finally, in order to demonstrate the versatility of the DHBC-based approach, we synthesize other metal NPs such as Pd and Pt, based on the identical protocol described for Au@DHBC NPs. As presented in Figure 2.13, highly water-dispersible Pd@DHBC and Pt@DHBC NPs are successfully prepared with a controllable size. It is also interesting to note that morphology of these NPs is significantly different from the

ULSAN NATIONAL INSTITUTE OF
SCIENCE AND TECHNOLOGY

spherical Au@DHBC NPs. This result further highlights the potential of our DHBC-based approach as a facile and general means of producing metal nanostructures with different functionalities for various applications, which will be the subject of our on-going endeavor.

ULSAN NATIONAL INSTITUTE OF SCIENCE AND TECHNOLOGY

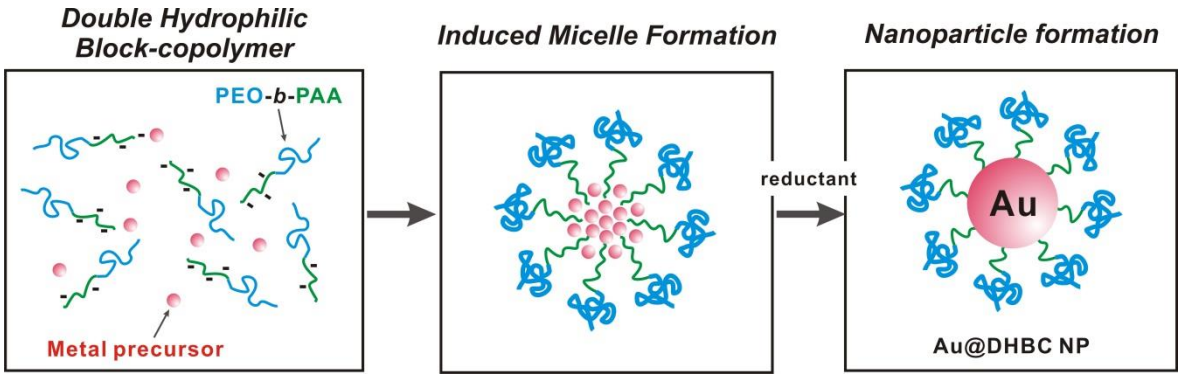

Scheme 2.2. Schematic illustration of the synthesis of Au@DHBC NP through the coordinative bonding between the Au precursor and a double hydrophilic block copolymer (DHBC) (PEO-*b*-PAA) as a soft template.

ULSAN NATIONAL INSTITUTE OF SCIENCE AND TECHNOLOGY

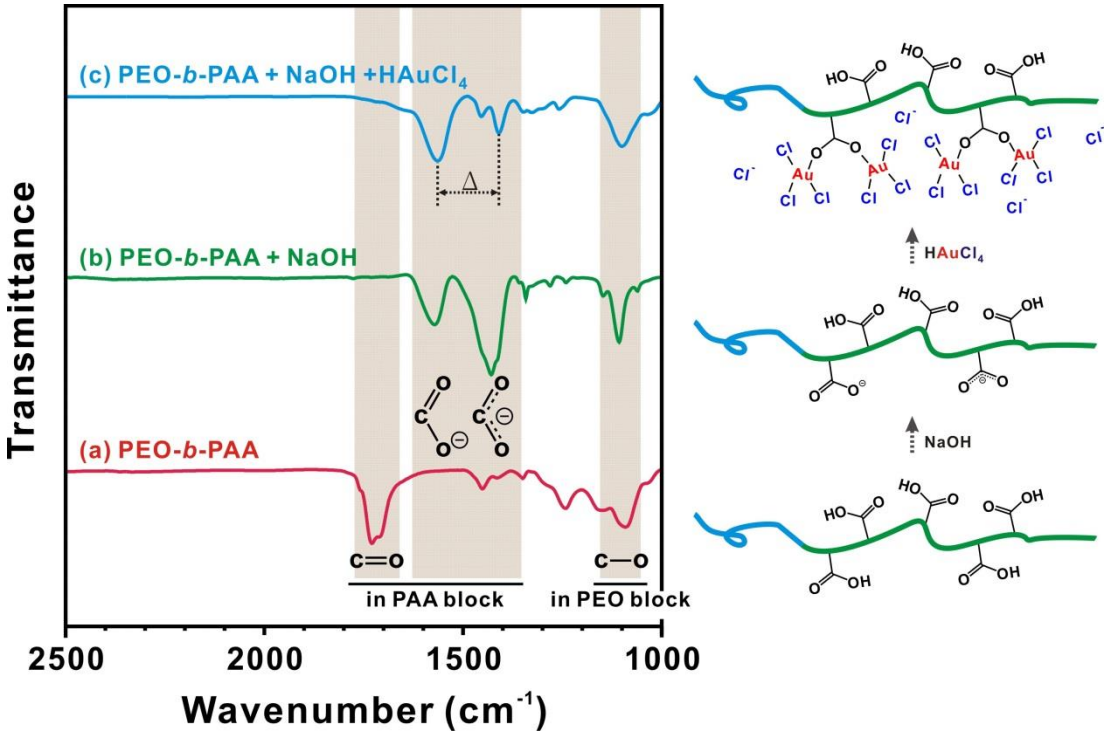

Figure 2.14. FT-IR spectra of (a) PEO-*b*-PAA, (b) PEO-*b*-PAA with NaOH, and (c) PEO-*b*-PAA with NaOH and Au precursor. The schematic description of the coordinative bond formation between Au precursor and carboxylate group is displayed in the right panel.

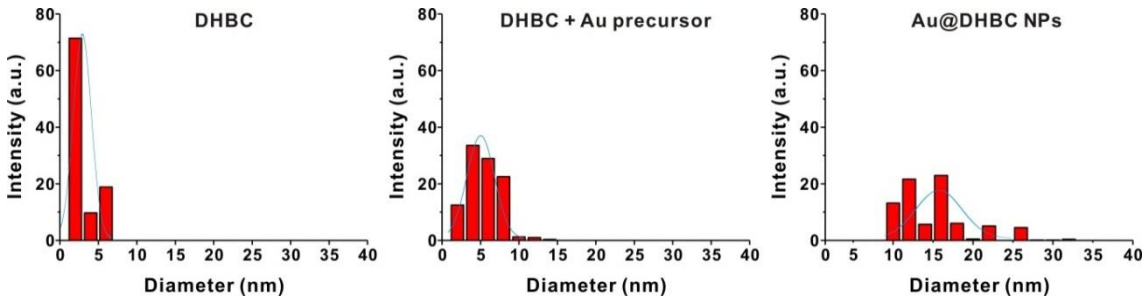

Figure 2.15. Dynamic light scattering (DLS) analysis of DHBC, DHBC with Au precursor and Au@DHBC NPs, providing the hydrodynamic diameter range of 0.10 - 5.62 nm, 0.67 - 12.87 nm and 8.01 - 31.62 nm, respectively.

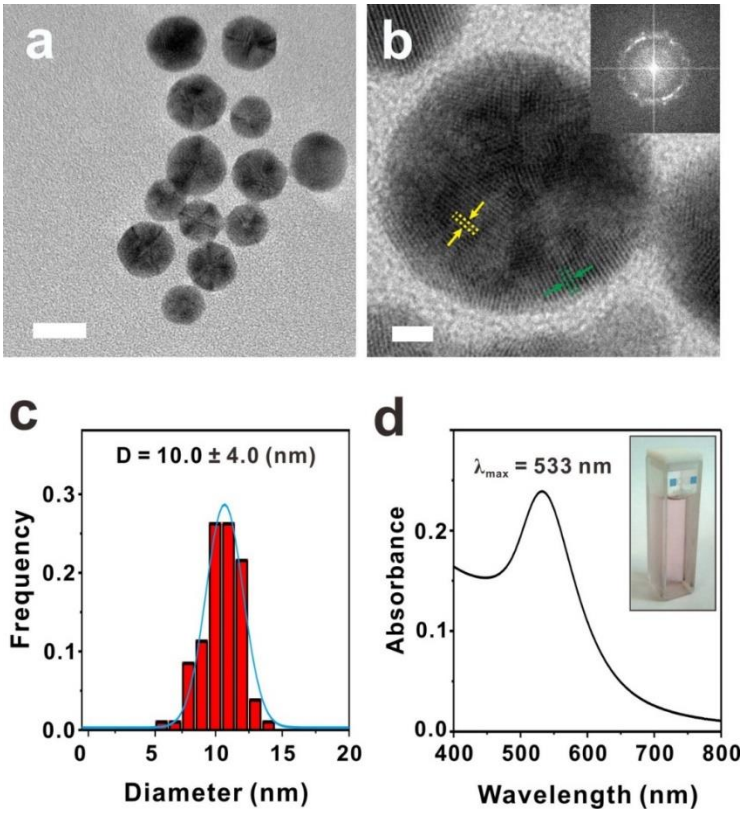

Figure 2.16. (a and b) TEM images of synthesized Au@DHBC. Scale bar in (a) represents 10 nm and (b) 2 nm. Inset in **Figure** 2b shows the crystalline lattice fringe of Au NP. (c) Corresponding size distribution histogram of as-prepared Au@DHBC NPs. (d) UV/vis spectrum of synthesized suspension of Au@DHBC NPs. Inset shows the photograph image of a suspension of Au@DHBC NPs.

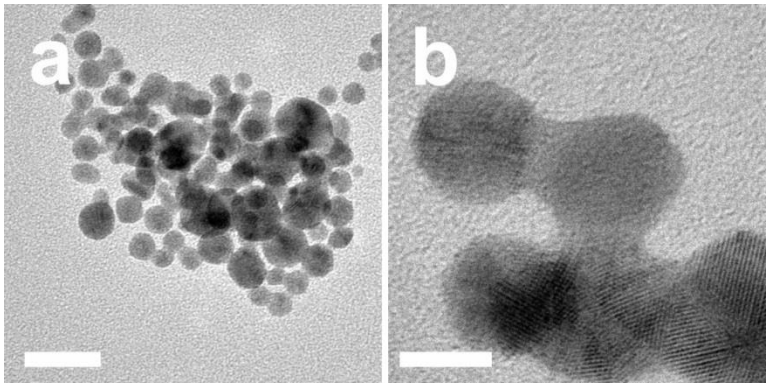

Figure 2.17. TEM images of Au@DHBC NPs before purification by centrifuge, showing the large Au aggregates. Scale bar in (a) represents 20 nm and (b) 5 nm.

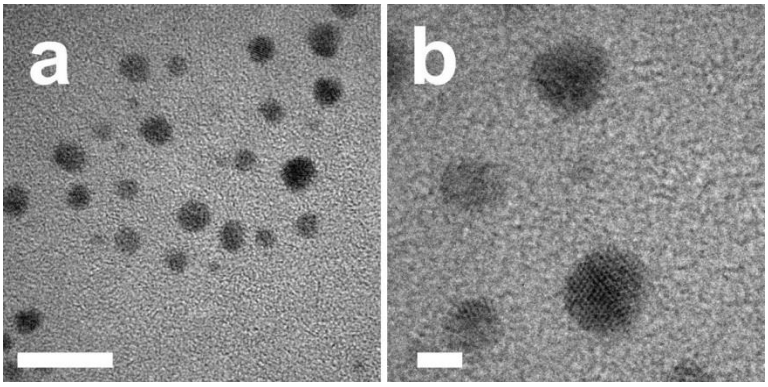

Figure 2. 18. TEM images of Au@DHBC NPs using 0.0067 mmol of $HAuCl_4 \cdot 3H_2O$. The diameter of Au NPs is ranged from 1 to 4 nm, which is smaller than that of Au@DHBC NPs used as a catalyst in the reduction of nitroarenes presented in this work. Scale bar in (a) represents 10 nm and (b) 2 nm.

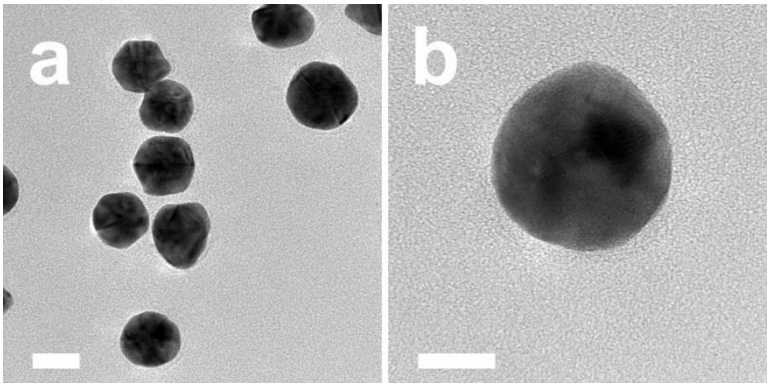

Figure 2.19. TEM images of Au@DHBC NPs reduced by ascorbic acid. The diameter of Au@DHBC NPs is ranged from 22 to 29 nm. Scale bar in (a) represents 20 nm and (b) 10 nm.

ULSAN NATIONAL INSTITUTE OF
SCIENCE AND TECHNOLOGY

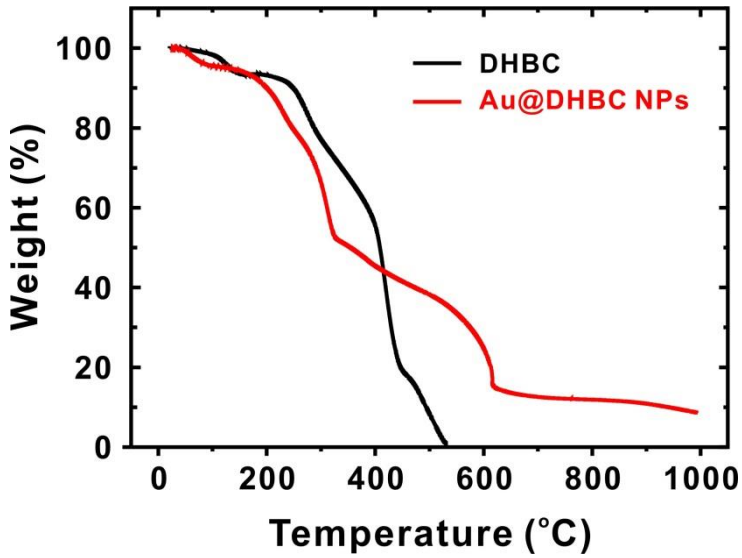

Figure 2.20. Thermogravimetric analysis (TGA) curves of (black) pure DHBC of PEO-b-PAA, and (red) synthesized Au@DHBC NPs. The samples were subjected to heating at a rate of 10 oC min-1 under air atmosphere.

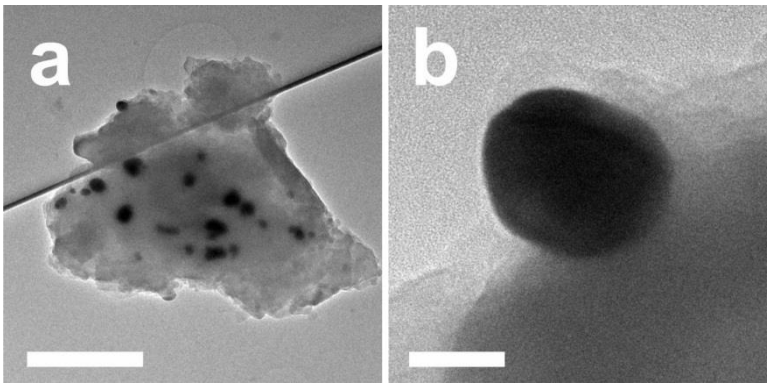

Figure 2.21. TEM images of Au@DHBC NPs annealed at 400 ºC for 2 h under Ar atmosphere. The size of Au@DHBC NPs surrounded by polymeric residue increased after thermal treatment. Scale bar in (a) represents 100 nm and (b) 20 nm

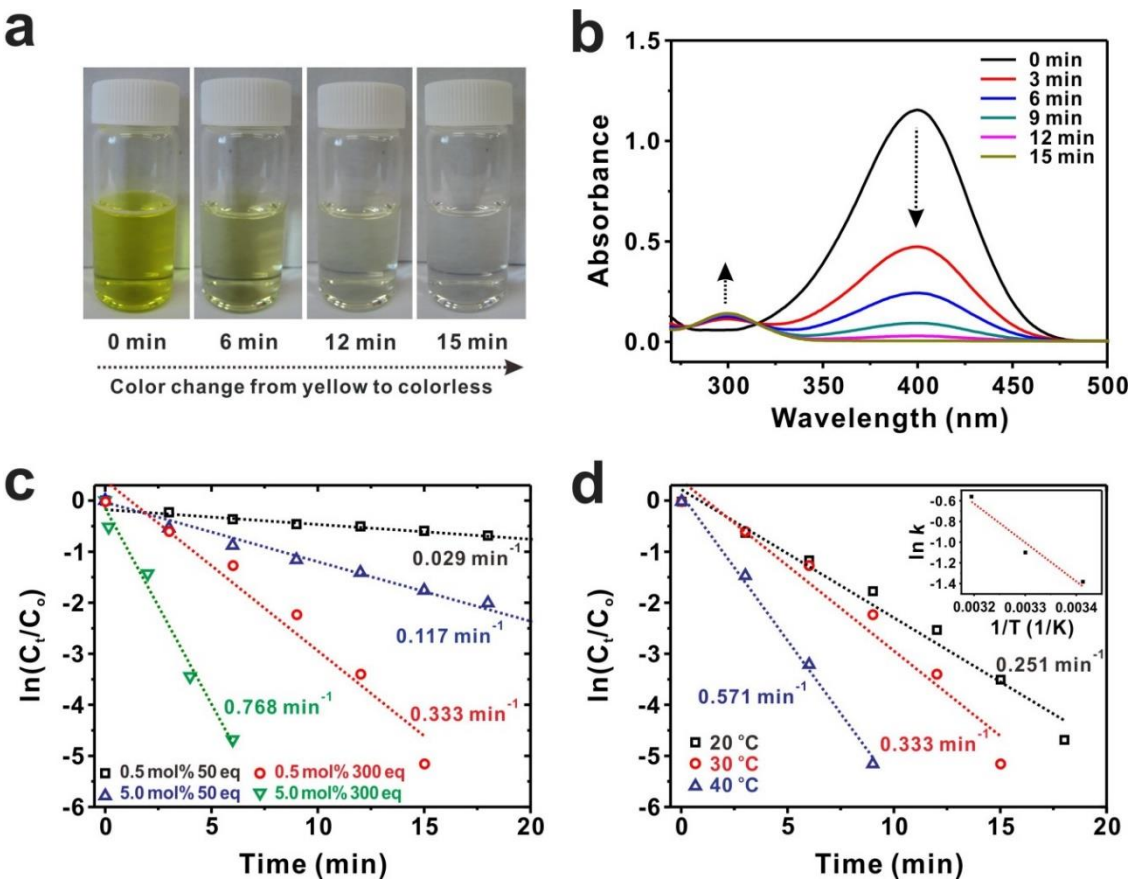

Figure 2.22. (a) The color change of 4-nitrophenol reduction with Au@DHBC NPs catalyst and $NaBH_4$. (b) Representative time-dependent UV/vis absorption spectra for the reduction of 4-nitrophenol over Au@DHBC NP catalyst in aqueous media at 303 K. (c) Plot of $\ln(C_t/C_0)$ versus time spectra for the reduction of 4-nitrophenol over Au@DHBC catalyst under different mol% of catalyst and equiv. of NaBH4 used. (d) Plot of $\ln(C_t/C_0)$ versus time for the reduction of 4-nitrophenol over Au@DHBC NP catalysts under different temperatures at 0.50 mol% of catalyst and 300 equiv. of $NaBH_4$. Inset shows the corresponding Arrhenius plot.

ULSAN NATIONAL INSTITUTE OF
SCIENCE AND TECHNOLOGY

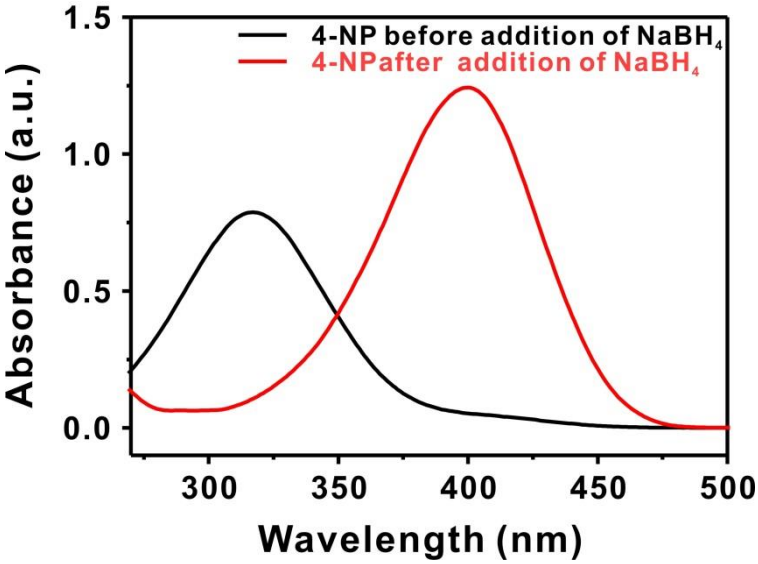

Figure 2.23. UV/vis spectra of 4-nitrophenol before and after the addition of $NaBH_4$.

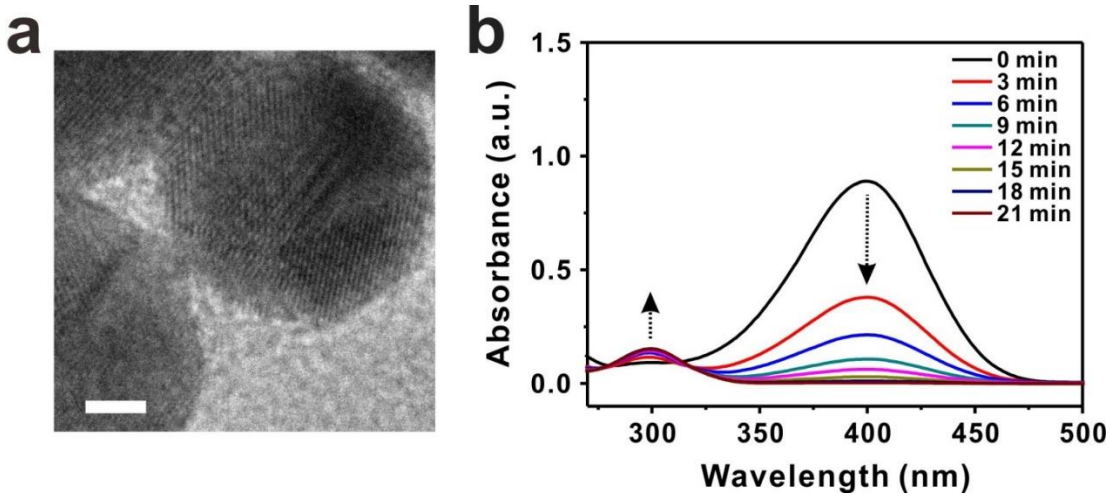

Figure 2.24. (a) TEM image of spherical Au NPs synthesized by citric acid, whose diameter is about 10.7 ± 4.3 nm (Scale bar in (a) represents 2 nm), and (b) time-dependent UV/vis spectra of 4-nitrophenol catalyzed using Au NPs synthesized by citric acid. 10 mL of 7.50×10^{-4} M 4-nitrophenol, 0.118 mL of 3.178×10^{-4} M Au catalyst (0.50 mol% with respect to the Au concentration) and 1.0 mL of 2.22 M $NaBH_4$ (300 equiv. to the substrate) were used for the reduction of 4-nitrophenol.

ULSAN NATIONAL INSTITUTE OF SCIENCE AND TECHNOLOGY

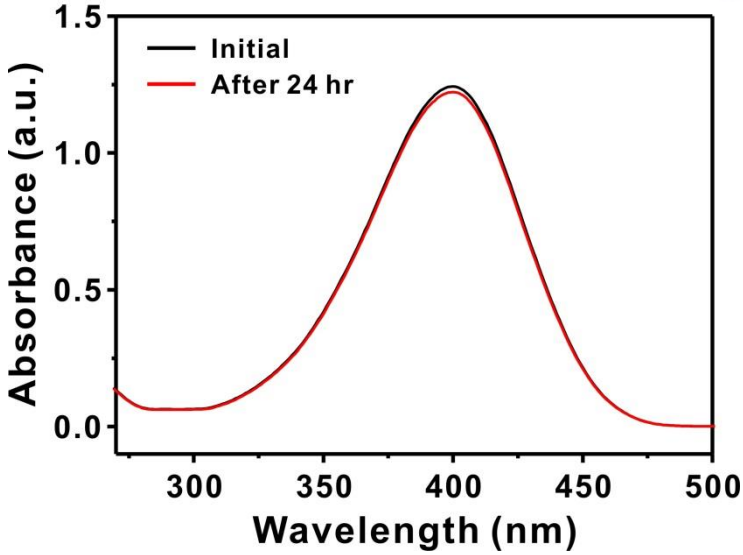

Figure 2.25. UV/vis spectra of 4-nitrophenol with $NaBH_4$ without Au@DHBC NP catalyst.

ULSAN NATIONAL INSTITUTE OF SCIENCE AND TECHNOLOGY

Table 2.2. Reduction of various nitroarenes using Au@DHBC NP catalyst[a]

Entry	Substrate	Product	Time[b]/min	TOF[c]/h^{-1}
1	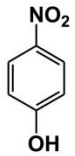	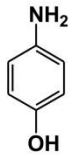	15	800
2	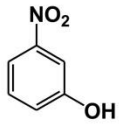	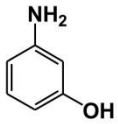	10	1200
3	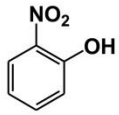	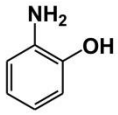	25	480
4	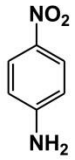	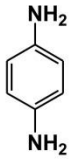	6	2000
5	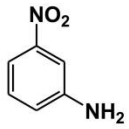	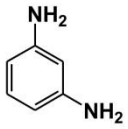	3	4000
6	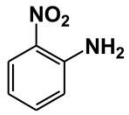	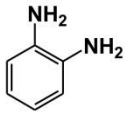	6	2000

[a]Reaction condition : 10 mL of 7.50 × 10^{-4} M nitroarenes, 0.566 mL of 6.63 × 10^{-5} M Au@DHBC NP catalyst (0.50 mol% with respect to the Au concentration), 1.0 mL of 2.22 M $NaBH_4$ (300 equiv. to the substrate).

[b]Time was determined when over 99.9% of nitroarenes were reduced.

[c]TOF is the ratio of the converted substrate to Au NPs catalyst used per unit time.

ULSAN NATIONAL INSTITUTE OF
SCIENCE AND TECHNOLOGY

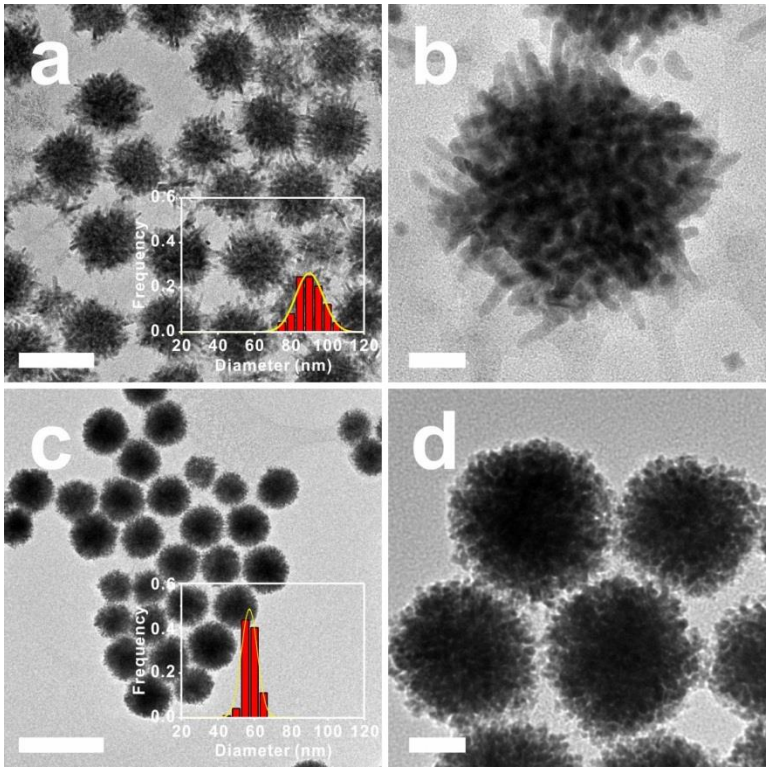

Figure 2.26. TEM images of the synthesized (a, b) Pd@DHBC NPs and (c, d) Pt@DHBC NPs with a histogram of size distribution. The average diameter is 87.9 ± 18.1 nm for Pd NPs and 55.5 ± 10.6 nm for Pt NPs, respectively. Scale bar in a and c represents 100 nm and b and d 20 nm.

ULSAN NATIONAL INSTITUTE OF SCIENCE AND TECHNOLOGY

2.4. Conclusion

We have developed a simple, facile method of synthesizing gold nanoparticles (Au NPs) using a double hydrophilic block copolymer (DHBC), PEO-*b*-PAA, as a soft template through the coordinative interactions between the carboxylate groups of PAA block of the polymer and the Au precursor. Each segment of the DHBC plays an important role in forming stable Au NPs; the PAA block of the DHBC interacts with the Au precursor to form micelle aggregates and templates Au NPs, whereas the PEO block stabilizes the NPs in aqueous solution. The synthesized Au@DHBC NPs are successfully employed in the catalytic reduction of a series of nitroarenes with an efficient catalytic activity by confined interior of polymeric shell around the Au NPs, further highlighting the importance of the DHBC template. We anticipate that Au NPs synthesized with DHBCs will broaden the application of Au NPs as heterogeneous catalysts in aqueous solutions. Moreover, the approach of synthesizing metal NPs with DHBCs can lead to a facile and general means of producing metal nanostructures with different functionalities for various applications.

ULSAN NATIONAL INSTITUTE OF SCIENCE AND TECHNOLOGY

2.5. References

(1) Skrabalak, S. E.; Chen, J.; Sun, Y.; Lu, X.; Au, L.; Cobley, C. M.; Xia, Y., Gold Nanocages: Synthesis, Properties, and Applications. *Acc. Chem. Res.* **2008,** *41*, 1587-1595.

(2) Corma, A.; Garcia, H., Supported Gold Nanoparticles as Catalysts for Organic Reactions. *Chem. Soc. Rev.* **2008,** *37*, 2096-2126.

(3) Grzelczak, M.; Pérez-Juste, J.; Mulvaney, P.; Liz-Marzán, L. M., Shape Control in Gold Nanoparticle Synthesis. *Chem. Soc. Rev.* **2008,** *37*, 1783-1791.

(4) Daniel, M. C.; Astruc, D., Gold Nanoparticles: Assembly, Supramolecular Chemistry, Quantum-Size-Related Properties, and Applications toward Biology, Catalysis, and Nanotechnology. *Chem. Rev.* **2004,** *104*, 293.

(5) Hu, M.; Chen, J.; Li, Z. Y.; Au, L.; Hartland, G. V.; Li, X.; Marquez, M.; Xia, Y., Gold Nanostructures: Engineering Their Plasmonic Properties for Biomedical Applications. *Chem. Soc. Rev.* **2006,** *35*, 1084-1094.

(6) Turkevich, J.; Stevenson, P. C.; Hillier, J., A Study of the Nucleation and Growth Processes in the Synthesis of Colloidal Gold. *Discuss. Faraday Soc.* **1951,** *11*, 55-75.

(7) Frens, G., Controlled Nucleation for the Regulation of the Particle Size in Monodisperse Gold Suspensions. *Nature* **1973,** *241*, 20-22.

(8) Brust, M.; Walker, M.; Bethell, D.; Schiffrin, D. J.; Whyman, R., Synthesis of Thiol-Derivatised Gold Nanoparticles in a Two-Phase Liquid–Liquid System. . *J. Chem. Soc., Chem. Commun.* **1994**, 801-802.

(9) Busbee, B. D.; Obare, S. O.; Murphy, C. J., An Improved Synthesis of High-Aspect-Ratio Gold Nanorods. *Adv. Mater.* **2003,** *15*, 414-416.

(10) Jana, N. R.; Gearheart, L.; Murphy, C. J., Seeding Growth for Size Control of 5-40 nm Diameter Gold Nanoparticles. *Langmuir* **2001,** *17*, 6782-6786.

(11) Sohn, B. H.; Choi, J. M.; Yoo, S. I.; Yun, S. H.; Zin, W. C.; Jung, J. C.; Kanehara, M.; Hirata, T.; Teranishi, T., Directed Self-Assembly of Two Kinds of Nanoparticles Utilizing Monolayer Films of Diblock Copolymer Micelles. *J. Am. Chem. Soc.* **2003,** *125*, 6368-6369.

ULSAN NATIONAL INSTITUTE OF SCIENCE AND TECHNOLOGY

(12) Mössmer, S.; Spatz, J. P.; Möller, M.; Aberle, T.; Schmidt, J.; Burchard, W., Solution Behavior of Poly(styrene)-*block*-Poly(2-vinylpyridine) Micelles Containing Gold Nanoparticles. *Macromolecules* **2000,** *33*, 4791-4798.

(13) Maye, M. M.; Chun, S. C.; Han, L.; Rabinovich, D.; Zhong, C. J., Novel Spherical Assembly of Gold Nanoparticles Mediated by a Tetradentate Thioether. *J. Am. Chem. Soc.* **2002,** *124*, 4958-4959.

(14) Teranishi, T.; Hasegawa, S.; Shimizu, T.; Miyake, M., Heat-Induced Size Evolution of Gold Nanoparticles in the Solid State. *Adv. Mater.* **2001,** *13*, 1699.

(15) Jana, N. R.; Gearheart, L.; Murphy, C. J., Evidence for Seed-Mediated Nucleation in the Chemical Reduction of Gold Salts to Gold Nanoparticles. *Chem. Mater.* **2001,** *13*, 2313-2322.

(16) Ji, X.; Song, X.; Li, J.; Bai, Y.; Yang, W.; Peng, X., Size Control of Gold Nanocrystals in Citrate Reduction: The Third Role of Citrate. *J. Am. Chem. Soc.* **2007,** *129*, 13939-13948.

(17) Seo, E.; Lee, T.; Lee, K. T.; Song, H. K.; Kim, B. S., Versatile Double Hydrophilic Block Copolymers: Dual Role as Synthetic Nanoreactor and Ionic and Electronic Conducting Layer for Ruthenium Oxide Nanoparticle Supercapacitors. *J. Mater. Chem.* **2012,** *22*, 11598-11604.

(18) Kim, A.; Sharma, B.; Kim, B. S.; Park, K. H., Double-Hydrophilic Block Copolymer Nanoreactor for the Synthesis of Copper Nanoparticles and for Application in Click Chemistry. *J. Nanosci. Nanotechnol.* **2011,** *11*, 6162-6166.

(19) Nakashima, K.; Bahadur, P., Aggregation of Water-Soluble Block Copolymers in Aqueous Solutions: Recent Trends. *Adv. Colloid Interface Sci.* **2006,** *123*, 75-96.

(20) Cölfen, H., Double-Hydrophilic Block Copolymers: Synthesis and Application as Novel Surfactants and Crystal Growth Modifiers. *Macromol. Rapid Commun.* **2001,** *22*, 219-252.

(21) Taubert, A.; Palms, D.; Weiss, Ö.; Piccini, M. T.; Batchelder, D. N., Polymer-Assisted Control of Particle Morphology and Particle Size of Zinc Oxide Precipitated from Aqueous Solution. *Chem. Mater.* **2002,** *14*, 2594-2601.

(22) Qi, L.; Cölfen, H.; Antonietti, M., Synthesis and Characterization of Cds Nanoparticles Stabilized by Double-Hydrophilic Block Copolymers. *Nano Lett.* **2001,** *1*, 61-65.

ULSAN NATIONAL INSTITUTE OF SCIENCE AND TECHNOLOGY

(23) Ojea-Jiménez, I.; Romero, F. M.; Bastús, N. G.; Puntes, V., Small Gold Nanoparticles Synthesized with Sodium Citrate and Heavy Water: Insights into the Reaction Mechanism. *J. Phys. Chem. C* **2010,** *114*, 1800-1804.

(24) Ivanova, B. B., Solid-State Linear-Dichroic Infrared Spectroscopic Analysis of the Dipeptide S-Phe–S-Phe and Its Mononuclear Au (III) Complex. *J. Coord. Chem.* **2005,** *58*, 587-593.

(25) Lu, Y.; Miller, J. D., Carboxyl Stretching Vibrations of Spontaneously Adsorbed and Lb-Transferred Calcium Carboxylates as Determined by Ftir Internal Reflection Spectroscopy. *J. Colloid Interface Sci.* **2002,** *256*, 41-52.

(26) Bronstein, L. M.; Huang, X.; Retrum, J.; Schmucker, A.; Pink, M.; Stein, B. D.; Dragnea, B., Influence of Iron Oleate Complex Structure on Iron Oxide Nanoparticle Formation. *Chem. Mater.* **2007,** *19*, 3624-3632.

(27) Chen, H.; Kou, X.; Yang, Z.; Ni, W.; Wang, J., Shape-and Size-Dependent Refractive Index Sensitivity of Gold Nanoparticles. *Langmuir* **2008,** *24*, 5233-5237.

(28) Vaidya, M. J.; Kulkarni, S. M.; Chaudhari, R. V., Synthesis of P-Aminophenol by Catalytic Hydrogenation of *p*-Nitrophenol. *Org. Process Res. Dev.* **2003,** *7*, 202-208.

(29) Li, H.; Jo, J. K.; Zhang, L.; Ha, C. S.; Suh, H.; Kim, I., A General and Efficient Route to Fabricate Carbon Nanotube-Metal Nanoparticles and Carbon Nanotube-Inorganic Oxides Hybrids. *Adv. Funct. Mater.* **2010,** *20*, 3864-3873.

(30) Choi, Y.; Bae, H. S.; Seo, E.; Jang, S.; Park, K. H.; Kim, B. S., Hybrid Gold Nanoparticle-Reduced Graphene Oxide Nanosheets as Active Catalysts for Highly Efficient Reduction of Nitroarenes. *J. Mater. Chem.* **2011,** *21*, 15431-15436.

(31) Lin, F.; Doong, R., Bifunctional Au-Fe_3O_4 Heterostructures for Magnetically Recyclable Catalysis of Nitrophenol Reduction. *J. Phys. Chem. C* **2011,** *115*, 6591-6598.

(32) Mahmoud, M.; Saira, F.; El-Sayed, M., Experimental Evidence for the Nanocage Effect in Catalysis with Hollow Nanoparticles. *Nano Lett.* **2010,** *10*, 3764-3769.

(33) Zeng, J.; Zhang, Q.; Chen, J.; Xia, Y., A Comparison Study of the Catalytic Properties of Au-Based Nanocages, Nanoboxes, and Nanoparticles. *Nano Lett.* **2009,** *10*, 30-35.

(34) Lee, J.; Park, J. C.; Song, H., A Nanoreactor Framework of a Au@SiO_2 Yolk/Shell Structure for Catalytic Reduction of *p*-Nitrophenol. *Adv. Mater.* **2008,** *20*, 1523-1528.

ULSAN NATIONAL INSTITUTE OF SCIENCE AND TECHNOLOGY

(35) Crooks, R.; Zhao, M., Dendrimer-Encapsulated Pt Nanoparticles: Synthesis, Characterization, and Applications to Catalysis. *Adv. Mater.* **1999,** *11*, 217-220.

(36) Zhao, M.; Crooks, R. M., Homogeneous Hydrogenation Catalysis with Monodisperse, Dendrimer-Encapsulated Pd and Pt Nanoparticles. *Angew. Chem. Int. Ed.* **1999,** *38*, 364-366.

(37) Yeung, L. K.; Crooks, R. M., Heck Heterocoupling within a Dendritic Nanoreactor. *Nano Lett.* **2001,** *1*, 14-17.

(38) Crooks, R. M.; Zhao, M.; Sun, L.; Chechik, V.; Yeung, L. K., Dendrimer-Encapsulated Metal Nanoparticles: Synthesis, Characterization, and Applications to Catalysis. *Acc. Chem. Res.* **2001,** *34*, 181-190.

(39) Chen, X.; Zhao, D.; An, Y.; Zhang, Y.; Cheng, J.; Wang, B.; Shi, L., Formation and Catalytic Activity of Spherical Composites with Surfaces Coated with Gold Nanoparticles. *J. Colloid Interface Sci.* **2008,** *322*, 414-420.

(40) Jin, Z.; Xiao, M.; Bao, Z.; Wang, P.; Wang, J. A General Approach to Mesoporous Metal Oxide Microspheres Loaded with Noble Metal Nanoparticles. *Angew. Chem. Int. Ed.* **2012**, *51*, 6406-6410.

***** *Chapter 2 is reproduced in part with permission of "Seo, E.; Kim, J.; Hong. Y.; Kim, Y. S.; Lee, D.; Kim, B.-S., J. Phys. Chem. C,* ***2013****, 117, 11686-11693" Copyright* ***2013*** *American Chemical Society.*

ULSAN NATIONAL INSTITUTE OF SCIENCE AND TECHNOLOGY

Chapter 3.

Plasmonic Transition via Interparticle Coupling of Au@Ag Core−Shell Nanostructures Sheathed in Double Hydrophilic Block Copolymer for High-Performance Polymer Solar Cell

3.1. Introduction

The emergence of plasmonics in nanoscale materials has renewed interests in the fundamental understanding of localized surface plasmons, which arise from collective and coherent oscillations of the conduction electrons in resonance with the incident light frequency on the surface of a metal nanoparticle (NP).[44-46] The creation and examination of numerous metal NPs have demonstrated the importance of each parameter, such as size, shape, and assembly, on tailoring their intrinsic plasmonic characteristics.[7, 47-57] Novel metal nanostructures and their alloys have been the subject of intensive researches owing to their interesting plasmonic behavior, including localized surface plasmon resonance (LSPR), surface-enhanced Raman scattering (SERS), and metal-enhanced fluorescence, which are useful for various applications toward biosensors, bioimaging, catalysis, thermal therapy, and optoelectronic devices, such as solar cells and light emitting diodes.[2, 58-63]

In particular, plasmonic metal NPs have received significant attention in polymer

***** Chapter 3 is reproduced in part with permission of *"Seo, E.; Ko, S.-J.; Min, S. H.; Kim, J. Y.; Kim, B.-S., Chem. Mater., **2015**, 27, 3785-3796"* Copyright **2015** American Chemical Society.

ULSAN NATIONAL INSTITUTE OF SCIENCE AND TECHNOLOGY

solar cells (PSCs) applications because their LSPR effect can lead to enhancement of incident light absorption and improvement of intrinsic scattering power for higher efficiency of solar cells. Among many novel metal NPs, gold and silver possess very effective plasmonic effects to trap incident light, which exhibit relatively strong scattering in the visible range.[64-65] However, attempts at obtaining high efficiency in PSCs by employing the SPR effect are limited because of the narrow resonant wavelength region of metal nanostructures.[45] In addition, direct integration of metal NPs into the active layer of PSCs often leads to exciton quenching in the system,[66-67] which inevitably requires surface passivation of the metal NPs.[60] In order to overcome these challenges associated with plasmonic metal NPs, it is essential to modulate the spectrum of light absorption, to improve the generation of excitons, and to prevent exciton quenching or recombination to maximize the plasmon effect on device performance.[68-72]

Numerous approaches to design the plasmonic properties of novel metal nanostructures, attributed to their size, shape and morphology, have been reported using specific surfactants or polymer capping methods. As an alternative to the traditional surfactant-based approach, block copolymer-templated syntheses can offer interesting opportunities not only for forming inorganic NPs with a controllable size and shape, but also for stabilizing the resulting NPs by forming steric or ionic barriers around the NPs in solution.[73-75] Furthermore, this block copolymer-based method offers a means to direct the spatial patterning of NPs on the surface as a result of their unique self-assembly behavior.[34, 76-78]

Most block copolymer self-assembly approaches rely on the use of entirely hydrophobic or amphiphilic block copolymers, forming various micellar structures in solution similar to the self-assembly of surfactants. On the other hand, double hydrophilic block copolymers (DHBCs) consisting of two chemically distinct segments with only hydrophilic features have recently stood out in the preparation of NPs.[79-81] Compared with hydrophobic block copolymer, all hydrophilic block copolymer shows unique feature in aqueous solution; for example, they dissolve readily in water to form molecularly dissolved solutions and induce potentially useful micellar aggregates with inorganic materials through polyion complexation in aqueous solution. These materials are important for the design of “nano-reactors” with DHBCs for ionic substances compared to the micelles of conventional amphiphilic block copolymers.[42]

ULSAN NATIONAL INSTITUTE OF SCIENCE AND TECHNOLOGY

To date, only a few reports using DHBCs for the preparation of metallic NPs have been achieved as a result of the limited tunability of size, shape or morphology. This DHBC-based synthetic approach to novel nanostructures is thus challenging because the micellization with inorganic materials via various types of polymer blocks and the corresponding mineralization for the formation of NPs are effectively controlled by many parameters such as temperature, ionic strength, pH variation and complexation in aqueous solution.[42, 82] Additionally, two different functional groups in DHBCs can be utilized to produce nanostructures, such as core-shell shapes, consisting of two or more metallic components via the seed-mediated method. In a DHBC system, one block typically exhibits a positive or negative charge in aqueous solution, which can interact with the metal precursor. On the other hand, the other block is typically neutral, but can be also employed as an active site assisting the NPs growth if oxygen atoms with abundant lone pair electrons are contained in the segment.

In this context, a DHBC-based synthesis of metal NPs offers a straightforward and versatile method to produce core-shell nanostructures under mild aqueous conditions without the use of organic solvents or thermal treatment. Furthermore, this report can shed new light on the diverse functionalities of DHBC, including (1) guidance for the controlled growth of core-shell structure, (2) coupling agent between NPs, (3) passivation for efficient introduction of surface plasmon effect directly in device, and (4) more importantly, protective layer against the energy transfer on device.

Herein, we report the synthesis of Au@Ag NPs using a soft DHBC template to prepare core-shell NPs, and investigate their potential as plasmonic nanomaterials in PSCs. Specifically, the DHBC of poly(ethylene oxide)-*block*-poly(acrylic acid) (PEO-*b*-PAA) provides a spherical Au NPs (Au@DHBC NPs) resulting from its micellar structure in aqueous solution.[83] Afterward, the Ag shell can be selectively grown on top of the Au@DHBC NPs because the PEO block interacts with the Ag^+ ions, leading to the Au@Ag@DHBC core-shell nanostructures. The shell thickness is simply controlled by the Ag precursor concentration, thus the plasmon properties of Au@Ag@DHBC NPs become highly tunable. Most interestingly, interparticle coupling is observed with the addition of high concentration of Ag^+ ions, leading to the transition of intrinsic plasmon bands of isolated individual Au@Ag@DHBC NPs to a wide range in the visible spectrum. Furthermore, coupled NPs are successfully employed as plasmonic nanomaterials to

ULSAN NATIONAL INSTITUTE OF
SCIENCE AND TECHNOLOGY

improve the light absorption window of the photoactive layer in PSCs, improving their efficiency by ~16%. Owing to the two different functional groups in the DHBC, this DHBC-based approach not only provides a unique alternative to the existing methods for preparation of core-shell metal nanostructures, but also allows for the tuning of SPR effect of novel NPs over a broad range for improved efficiency in optoelectronic devices.

ULSAN NATIONAL INSTITUTE OF SCIENCE AND TECHNOLOGY

3.2. Experimental Section

Materials. Double hydrophilic block copolymer PEO(5000)-*b*-PAA(6700) was purchased from Polymer Source, Inc. Gold(III) chloride trihydrate ($HAuCl_4 \cdot 3H_2O$), silver nitrate ($AgNO_3$), and L-ascorbic acid (AA) from Sigma-Aldrich and sodium hydroxide (NaOH) from Junsei Chemical were used without further purification.

Synthesis of Au@DHBC NPs. Au NPs with a double hydrophilic block copolymer shell (Au@DHBC NPs) were prepared according to the following protocol.[83] First, PEO(5000)-*b*-PAA(6700) (25.12 mg, 0.20 mmol of carboxylic acid groups) was dissolved under vigorous stirring in 50.0 mL of deionized water, followed by the addition of 0.10 mL of 4.0 M NaOH (0.40 mmol, 2 equiv. to carboxylic acid groups in PAA block). To this solution, 4.47×10^{-3} M $HAuCl_4 \cdot 3H_2O$ (26.2 mg, 0.067 mmol) was added. Subsequently, 2.0 mL of 1.0 M AA (2.0 mmol) was added to the resulting suspension under vigorous stirring. After a few minutes, the solution underwent a color change to transparent red. After the reaction, the solution was dialyzed against deionized water using a dialysis membrane (MWCO 12,000–14,000, SpectraPore) to remove any residuals. The prepared suspension of Au@DHBC NPs exhibited fairly good colloidal stability, which lasted more than 6 months without any precipitation.

Synthesis of Au@Ag@DHBC NPs. Gold-silver-DHBC core-shell nanostructures (Au@Ag@DHBC NPs) were synthesized via a seed-mediated method. As-prepared Au@DHBC NPs were used as seeds for the growth. A solution of as-synthesized Au@DHBC NPs (0.5 mL) was first diluted with a certain amount of water, followed by the addition of different amounts of Ag precursor ranging from 0.2 to 2.0 μmol into the solution with the total volume fixed at 1.5 mL. As-synthesized Au@Ag NPs by DHBC are denoted Au@Ag_n@DHBC, where *n* is the molar concentration of Ag precursor used for the synthesis of the NPs. For example, when 0.1 and 1.0 μmol of Ag precursor is employed in the reaction, the NPs are denoted as Au@$Ag_{0.1}$@DHBC and Au@$Ag_{1.0}$@DHBC, respectively.

Characterization. The morphology, size, and size distribution of the prepared NPs were investigated using transmission electron microscopy (TEM), high-angle annular dark field scanning transmission electron microscopy (HAADF-STEM) and energy dispersive X-ray spectroscopy (EDXS) (JEOL, JEM-2100F, accelerating voltage of 200

ULSAN NATIONAL INSTITUTE OF SCIENCE AND TECHNOLOGY

kV, Gatan CCD camera). UV-Vis spectra were recorded using a UV-Vis spectrophotometer (Shimadzu UV-1800) and size distribution analyses were performed using dynamic light scattering (DLS, BI-APD, Brookhaven Instruments, New York, USA).

Fabrication and Characterization of Solar Cells. Devices were fabricated according to the following procedure. First, the ITO/glass substrates were cleaned with detergent, then ultra-sonicated in acetone and isopropyl alcohol and subsequently dried in an oven overnight at 100 °C. Poly(3,4-ethylenedioxythiophene):polystyrene sulfonate (PEDOT:PSS) layers, which were used as the anode, were spin-coated (after passing through a 0.45 μm cellulose acetate syringe filter) at 5000 rpm for 40 s, followed by baking at 145 °C for 10 min in air. A solution of Au@Ag@DHBC NPs was spin-coated on top of the PEDOT:PSS layer and then baked at 60 °C for 5 min. For deposition of the active layer, a blend solution of poly[4,8-bis(5-(2-ethylhexyl)thiophen-2-yl)benzo[1,2-b:4,5-b'] dithiophene-co-3-fluorothieno[3,4-b] thiophene-2-carboxylate] (PTB7-Th) (1 wt%):[6,6]-phenyl-C_{71}-butyric acid methyl ester ($PC_{71}BM$) (1.5 wt%) dissolved in chlorobenzene with 3 vol% diphenylether was spin-coated on top of the PEDOT:PSS layer in a nitrogen-filled glove box. The device was pumped down in a vacuum ($<10^{-6}$ torr; 1 torr = 133 Pa), and a 100 nm thick Al electrode, for convention, was deposited on top of the active layer by thermal evaporation. The deposited Al electrode area defined the active area of the device as 13 mm^2. Measurements were performed with the solar cells inside the glove box by using a high-quality optical fiber to guide the light from the solar simulator equipped with a Keithley 2635A source measurement unit. The J-V curves for the devices were measured under AM 1.5 G illumination at 100 mW/cm^2 with masking. External quantum efficiency (EQE) measurements were also conducted in ambient air using an EQE system (Model QEX7) by PV Measurements Inc. (Boulder, Colorado). After collecting the EQE data, the software also integrated the data with the AM 1.5 G spectrum and reported the calculated J_{SC} values.

Simulation of Electric Field Distribution. The E-field enhancement and extinction cross-section for Au@Ag@DHBC NPs were calculated by a finite-difference time-domain (FDTD) method (FDTD Solutions 8.6, Lumerical). The numerical simulations were performed in a three-dimensional box with a cell size of 0.1 nm and perfectly matched layers for all boundaries. For the Au@Ag@DHBC core-shell NP model, the

ULSAN NATIONAL INSTITUTE OF
SCIENCE AND TECHNOLOGY

diameter and interparticle spacing of the NPs were adjusted according to the TEM observations. The dielectric functions of Au, Ag and DHBC in the UV-Vis region were described by a multi-coefficient fitted model of the experimental data by Palik.[84] The Au@Ag@DHBC NPs were illuminated by a total-field/scattered-field plane wave source to obtain the extinction cross section as a function of wavelength by calculating the absorption and scattering cross sections.

ULSAN NATIONAL INSTITUTE OF SCIENCE AND TECHNOLOGY

3.3. Results and Discussion

The syntheses of Au@DHBC and Au@Ag@DHBC NPs are illustrated in Scheme 3.1. The initial synthetic procedure for Au NPs as a core material was modified from the method reported in our previous research.[83] In the preparation of Au NPs by DHBC, the PAA block facilitates the micellar formation by interacting with the metal precursor, followed by forming spherical Au nanostructure with an average diameter of 17.0 ± 4.1 nm and a surface plasmon band at 522 nm (Figure 3.1a and 3.2). Simultaneously, the PEO block provides steric stabilization for the resulting Au@DHBC NPs, which are stable for a few months without any aggregation.

We then employed the Au@DHBC NPs as a seed to further synthesize core-shell nanostructures via the following process. Briefly, the Au@DHBC NPs solution is mixed with different concentrations of Ag precursor, followed by the addition of a reducing agent into the mixture to grow the Ag shell with various thicknesses on top of the Au@DHBC NPs. As-prepared core-shell NPs are denoted as Au@Ag$_n$@DHBC NPs, where n represents the moles of Ag precursor added to the Au seed solution (typically n = 0.1-2.0 μmol). As shown in Figure 3.1b and 1c, the Au core and Ag shell portions are clearly distinguishable due to their electron density contrast. Additional high-resolution dark field HADDF STEM images included in the inset of Figure 3.1 and 3.3 clearly indicate a boundary between Au core and Ag shell with varying shell thickness. In addition, both the compositional line profiles (Figure 3.1d) and the corresponding energy dispersive spectrum (EDS) point analysis (Figure 3.4) confirm the presence of Au and Ag located in the core and shell, respectively. Upon the formation of the Ag shell on top of Au@DHBC NPs, the original surface plasmon band at 522 nm gradually blue-shifted toward 505 nm (Au@Ag$_{0.1}$@DHBC NPs) and 419 nm (Au@Ag$_{0.9}$@DHBC NPs), which is characteristic of the LSPR of spherical Ag NPs.

It is worth noting that no free Ag NPs were found after the formation of the core-shell of Au@Ag@DHBC NPs. It has been previously reported that PEO plays an important role not only in forming sterically stabilized NPs in solution but also in guiding the reduction of Ag ions into metallic Ag NPs.[85-86] The role of oxygen atoms in reducing the metal salts is similarly demonstrated in the case of polyvinylpyrrolidone (PVP) in creating NPs with various structures.[87-88] Similarly, in our system, PEO block in DHBC provides an active site to bind with the Ag ions due to the lone pair electrons on oxygen, leading

ULSAN NATIONAL INSTITUTE OF SCIENCE AND TECHNOLOGY

to the ion-dipole interaction between the Ag ions and the polymer. This interaction facilitates the formation of Ag shell on the surface of Au seed because PAA block binding with Au core cannot participate in the reaction of Ag ions, and simultaneously PEO block exposed out of core interacts with Ag ions. We therefore highlight the significant role of DHBC in creating core-shell type nanostructures in a controllable manner to form a shell on top of Au@DHBC seeds.

Upon the formation of the Ag shell on top of Au@DHBC NPs, the solution of Au@Ag@DHBC NPs exhibits aprogressive color transition from red to yellow and orange (Figure 3.5a), as similarly observed in color changes of spherical Ag nanostructures with different diameters.[89] The color difference also indicates that the Ag shell is homogeneously grown without particular transformation of structures. The thickness of the Ag shell can be efficiently tuned by controlling the amount of Ag precursor in solution. For example, as the concentration of Ag precursor is increased in the range from 0.1 to 1.0 μmol at a fixed concentration of Au@DHBC core, the average Ag shell thickness grows from 1.0 ± 1.54 to 11.3 ± 2.62 nm with a concomitant increase in the overall core-shell particle sizes from 17.0 ± 1.54 to 28.3 ± 2.62 nm (Figure 3.5b).

The absorption spectra display the plasmonic properties of core-shell NPs as a function of Ag shell thickness (Figure 3.5c). An increasing ratio of the Ag precursor to the Au seed can further lead to stronger plasmon absorption, hence a new band at approximately 420 nm gradually appears, which eventually merges with the band at higher wavelengths of the Au@DHBC NPs. This result suggests that the uniform growth of the Ag shell on top of the Au@DHBC core can effectively modulate the plasmonic properties of Au@Ag@DHBC NPs. In accordance with results, we emphasize that isolated Au@Ag NPs with tunable shell thickness can be simply prepared by DHBC templates in solution. Because the SPR of metallic NPs is well known to be highly sensitive to the surrounding environment, the formation of Ag shell on Au@DHBC NPs with tunable size can significantly influence the local electric field of Au@Ag@DHBC NPs. Thus, we simulated the electric field distribution using the three-dimensional finite-difference time-domain (FDTD) method to explore the electric field enhancement created by the Ag shell (Figure 3.6).[90] The results indicate that the plasmonic band changes of Au@Ag@DHBC NPs are in good agreement with those of the simulated spectra with Mie extinction calculations, even though the subtle differences between them are likely

ULSAN NATIONAL INSTITUTE OF SCIENCE AND TECHNOLOGY

to arise from the polydispersity in the size and shape of the resulting NPs.

Interestingly, the SPR band at 420 nm gradually increases with the growth of the Ag shell up to a certain point, and then a new plasmon band at 520 nm begins to appear for Au@$Ag_{1.0}$@DHBC NPs. The former is attributed to the dipole oscillation of the isolated Au@Ag@DHBC NPs, whereas the latter is considered as a discrete plasmon absorption that requires more characterization to understand completely. Thus, we further investigated the structures and plasmonic properties of Au@Ag@DHBC NPs at higher concentrations of Ag precursor.

In the low concentration range (n < 0.9), the shell thickness of the isolated NPs consistently increased up to 11.1 nm (n = 0.9), which was similar to the theoretical chain length of the PEO block used in this study (~9.1 nm) (see Supporting Information for theoretical calculation).[91] In contrast, at the loading of 0.9 μmol Ag precursor, the shell growth was slowed down, and the isolated NPs began to form disordered string-like nanostructures in solution (Figure 3.7). It continued to grow into large-sized clusters with increase in concentration of Ag precursor as shown in Figure 3.8. In the high concentration range (n > 0.9), the PEO block no longer assists the shell growth, but rather it provides a nanobridge between NPs, resulting in the interparticle coupling. Consequently, the coupled Au@Ag@DHBC NPs form cluster-like nanostructure instead of bulk agglomerates by the nanobridge between NPs. Thus, the PEO blocks in DHBC also play an essential role in this morphological transition of NPs as well as the Ag shell growth. This morphological change of NPs is significantly correlated with their plasmon feature, which will be discussed in the following section.

Recently, numerous studies on plasmon transition of NPs with their morphology have been reported. Single NPs generally have their intrinsic plasmonic absorption, e.g. a plasmon band at 520 nm of Au NP.[19] A dimer system with a nanogap generates new longitudinal mode, whose dipolar response consistently red-shifts due to plasmon coupling when the particle separation is reduced further.[92] Because dimeric-like structure with nanogap is not physically contacted with neighboring NPs, no charge can be completely separated, leading to low-frequency mode attributed to the diverse plasmon mode such as antibonding dipolar, bonding dipolar and quadrupolar mode.[93] These unphysical modes evolve into physical modes when the particle contact is made in the overlapping interparticles at a point. This overlapped particles show the low-frequency

ULSAN NATIONAL INSTITUTE OF SCIENCE AND TECHNOLOGY

mode which is a true dipolar mode, giving rise to the charge transfer in the conductive junction of interparticles. Additionally, this mode blue-shifts when overlap region is increased.[94-97] Similarly, in our Au@Ag@DHBC NPs, new plasmon mode over 520 nm is expected to be induced by generation of conductive junction and corresponding diverse dipolar mode and charge separation (yellow region in Figure 3.9a). However, in contrast to the dimeric system with physically contact, this low-frequency mode of Au@Ag@DHBC NPs consistently red-shifted towards near-infrared region the concentration of Ag ions increases (C line in Figure 3.9b). One possible explanation is that Ag ions are consumed mostly to produce new junction between neighboring NPs as well as to increase the shell thickness of NPs at a high concentration of Ag precursor. It is supported that no significant change is observed in the vertical length of junction, when comparing with Au@Ag@DHBC NPs synthesized at high concentration of Ag precursor. (Figure 3.10). On the other hand, the transverse plasmon mode remains steady (T line in Figure 3.9b) as the NPs maintains their spherical-like structure regardless of the increased concentration of Ag precursor. This morphological transition is accompanied by a colorimetric response of NPs, as a result of the change in plasmon coupling. The color of the solution turns to dark brown, which confirms the clustering of NPs. With a further increase in the concentration of Ag precursor ($n > 1.6$), the solution becomes transparent because the larger clusters eventually begin to precipitate out of the solution (inset in Figure 3.9b). Therefore, our current study can provide a method using DHBC templates for preparation of two types of Au@Ag@DHBC nanostructure including isolated NPs with different shell thickness and coupled NPs with tunable plasmon bands in solution.

We then studied the transition of core-shell Au@Ag@DHBC NPs via interparticle coupling to elucidate the detailed mechanism by collecting a series of TEM images and size distribution data using dynamic light scattering (DLS) at specific intervals. Au@$Ag_{1.6}$@DHBC NPs are employed as a model system because they exhibit two apparent and distinguishable absorption peaks. The collected solution at a specific time is diluted 40 times with water to quench the reaction, immediately followed by dropping the solution on a TEM grid and dried in vacuum. As shown in Figure 3.11a, the Ag shell is uniformly grown on the surface of the Au@DHBC NPs without any by-products after 5 min. Thereafter, new NPs with a diameter of several nanometers, which have rarely been observed in the growth of isolated Au@Ag@DHBC NPs, began to appear near the

ULSAN NATIONAL INSTITUTE OF SCIENCE AND TECHNOLOGY

growing Au@Ag@DHBC NPs, while the thickness of the Ag shell consistently increased (10 min in Figure 3.11a). It is apparent that newly nucleated NPs consist of metallic Ag since their average diameter is much smaller than that of the Au seeds, and their electron density contrast is similar to that of the Ag shell of Au@Ag@DHBC NPs.

During the growth reaction from 15 to 30 min, it was observed that the population of the newly nucleated Ag NPs decreased, indicating that the Ag NPs independently moving in solution were absorbed and eventually merged into the Ag shell of Au@Ag@DHBC NPs. This integration is strongly attributed to Ostwald ripening, which is a dynamic process in solution to further grow the Ag shells. After the Ag shell had grown to a specific thickness, Ag NPs diffused into the adjacent Au@Ag@DHBC NPs at the same time, leading to coupling between isolated NPs after 45 min, as presented in Figure 3.11a. Each of the reaction steps, such as shell growth, new Ag NPs formation and their integration into the Ag shell and interparticle coupling, obviously proceed at different time scales. However, we have discovered that these processes were not completely separated because small NPs less than 10.0 nm as well as large NPs of tens to hundreds of nanometers in size were observed according to the DLS measurements (10 and 30 min in Figure 3.11c). Furthermore, two strong size distributions at 60 min suggest the presence of isolated NPs as well as the formation of coupled NPs with various cluster sizes, indicating the heterogeneous interparticle coupling.

Considering all of these results, we propose a mechanism for the growth of core-shell type nanostructures and the further coupling of NPs based on the role of DHBC. At the initial stage, Au ions bind with the carboxylate groups of the PAA block through coordinative bonding, forming the micellar structure for spherical Au@DHBC NPs. Subsequently, the PEO block provides an active site to guide the formation of Ag shell on top of the Au core via ion-dipole interactions. Furthermore, free Ag NPs are nucleated from excess Ag ions in the solution and merged into the Ag shell of adjacent Au@Ag@DHBC NPs by Ostwald ripening, leading to the interparticle coupling assisted by the presence of DHBC.

To evaluate the plasmonic effect of Au@Ag@DHBC NPs in PSCs, devices were fabricated with both isolated NPs (Au@$Ag_{0.9}$@DHBC NPs) and coupled NPs (Au@$Ag_{1.6}$@DHBC NPs) and the control device was prepared without plasmonic NPs. To achieve high device performance, the devices were prepared by blending low band

ULSAN NATIONAL INSTITUTE OF SCIENCE AND TECHNOLOGY

gap polymers, poly[4,8-bis(5-(2-ethylhexyl) thiophen-2-yl)benzo[1,2-b:4,5-b'] dithiophene-co-3-fluorothieno[3,4-b] thiophene-2-carboxylate] (PTB7-Th) as a donor and [6,6]-phenyl-C_{71}-butyric acid methyl ester ($PC_{71}BM$) as an acceptor, for the active layer. The information on the synthesis and photovoltaic properties of PTB7-Th has recently been reported.[98] The device structures are ITO/PEDOT:PSS/active layer/Al for the control device and ITO/PEDOT:PSS/Au@Ag@DHBC NPs/active layer/Al for the testing device (Figure 3.12a). More than 350 devices were prepared to optimize the device performance by controlling the concentration of NPs in the PTB7-Th:$PC_{71}BM$-based PSCs. Any specific distinction in the morphology and thickness of active layer is not observed after the incorporations of NPs into the system, which is confirmed using atomic force microscope (AFM) and surface profiler (Figure 3.13).

Figures 3.12b and c show current density-voltage (J-V) characteristics and incident photon-to-electron efficiency (IPCE), respectively, and the device parameters are summarized in Table 3.1. The best control device shows a short-circuit current (J_{SC}) of 14.53 mA/cm^2, an open-circuit voltage (V_{OC}) of 0.78 V, a fill factor of 0.68, and a power conversion efficiency (PCE) of 7.77%. The device with isolated NPs has a J_{SC} of 15.78 mA/cm^2, V_{OC} of 0.78 V, FF of 0.69 and PCE of 8.51%. The PCE value with approximately 9.5% enhancement for the device with isolated NPs can be primarily attributed to the increase in J_{SC}, which is caused by IPCE improvement in the 400-700 nm range, as shown in Figure 3.12c, whereas the FF is slightly increased. Furthermore, the device with coupled NPs shows a J_{SC} of 16.28 mA/cm^2, V_{OC} of 0.79 V, FF of 0.70, and PCE of 9.00%, exhibiting ~16% enhancement in the PCE value. The enhanced PCE of the device with coupled NPs is attributed to the plasmon transition resulting from interparticle coupling, which is effective at broadening the absorption region as well as inducing stronger photon absorption and light scattering. Since little change in conductivity is expected by the addition of metal NPs,[64] the plasmonic effect of the NPs is considered as a main factor of the significant increases in PCE. We tested the device with Au@DHBC NPs only without Ag shell to confirm the plasmonic effect on device. As similar to device performance with Au@Ag@DHBC NPs, the device incorporating with Au@DHBC NPs show the enhanced IPCE (3.1% enhancement) (Figure 3.14 and Table 3.2).

To clarify the plasmonic effect of isolated and coupled NPs on the photogeneration of charge carriers, we compared the enhanced IPCE (ΔIPCE) and absorbance (Δabsorbance)

ULSAN NATIONAL INSTITUTE OF SCIENCE AND TECHNOLOGY

of the devices (Figure 3.12d). The IPCE enhancement of both devices with isolated and coupled NPs was found to show not only a strong absorption near 400 nm but also an extended absorption with broad visible and near-infrared region, which is consistent with the peaks in the difference of the absorbance spectrum.

For isolated NPs, the absorbance near 420 nm in solution is a unique feature, contributing to the enhancement of absorption near 400 nm on device. Interestingly, the device with isolated NPs exhibits two discrete light absorption near 530 nm and over 700 nm (Figure 3.12d), which may be attributed to the arrangement due to close spacing between the isolated NPs deposited on the film during device fabrication,[99] as characterized by AFM (Figure 3.15). Particularly, the absorbance of the film near 530 nm leads to the improvement of light absorption on device, which is considered to enhance the efficiency of device with isolated NPs (Figure 3.16). The enhanced light absorption over 700 nm hardly contributes to the device efficiency because the light absorption by active layer in the near-infrared region is significantly lower than in the visible region (Figure 3.12c). On the other hand, the device with coupled NPs shows higher absorption in full visible region (Figure 3.12d), compared with the device with isolated NPs. Moreover, it exhibits similar to tendency of change in the difference of ICPE, which is in agreement with absorption of coupled NPs in solution. Therefore, the incorporation of coupled NPs into the device is more advantageous for the enhancement of efficiency in PSCs, since an extended absorption into visible region on the device with isolated NPs practically has a moderate effect on the device efficiency.

The light absorption in PSCs can be enhanced by light trapping by NPs with surface plasmon and scattering the absorbed light by NPs.[45] To explore the contribution of absorption and scattering caused by NPs, we simulated the effect of NPs with different arrangements on device. The results indicate that the incident light is simultaneously absorbed and scattered by NPs, but the effect of absorption of NPs on device is much higher than that of light scattering (Figure 3.17). It implied the contribution of light absorption by NPs is relatively dominant for efficiency improvement in PSCs.[100]

It is remarkable that as-prepared NPs can be directly integrated into an active layer. We recently presented Ag NPs surrounded with a silica shell (Ag@SiO_2 NPs) to prevent exciton quenching[60] which often occurs when plasmonic NPs without any passivation layer come into direct contact with an active layer medium. However, we have found in

ULSAN NATIONAL INSTITUTE OF SCIENCE AND TECHNOLOGY

our system that both isolated and coupled NPs can be successfully employed at the active interface with the aid of DHBC layers. To clearly elucidate the distinct feature of DHBC surrounding NPs against the quenching effect, we measured steady-state photoluminescence (PL) on film with the same thickness, including structures of Super Yellow (SY), PEDOT:PSS/SY and PEDOT:PSS/isolated or coupled NPs/SY films coated on glass substrates. As a control test, SY films are fabricated with free Ag and Au NP of similar diameter without DHBC (see Experimental section and Figure 3.18). The PL intensity of PEDOT:PSS/isolated or coupled NPs/SY film is ~7.4% and 11.0% higher than that of control PEDOT:PSS/SY film, respectively, whereas the PEDOT:PSS/free Ag or Au NPs/SY film show relatively lower PL intensity (decrease of 8.9 and 12.4%) than the film without NPs because of considerable exciton quenching at the interface of PEDOT:PSS/SY by the metal NPs (Figure 3.19).

Additionally, we measured the photoluminescence quantum efficiency (PLQE) of SY film of the same thickness for all samples to specifically support the PL results. The PLQE of SY films with isolated and coupled NPs exhibited higher values (12.36% and 13.64%, respectively) than those of the films with free Ag and Au NPs (10.78% and 10.07%, respectively), though the PLQE of the films with isolated and coupled NPs is lower than that of bare SY film due to strong exciton quenching effect induced by PEDOT:PSS layer (Table 3.3). This is in good agreement with steady-state PL results because the tendency of PLQE with and without NPs is well matched with that of PL spectra. It is obvious that PL quenching does not occur on devices incorporated with isolated and coupled NPs at the interface of PEDOT:PSS and active layer. This indicates that DHBC chains, which form a very thin layer on the surface of the NPs, provide a protective layer against exciton quenching, resulting in plasmonic NPs that can be effectively integrated to a device. Therefore, we highlight that Au@Ag@DHBC NPs with a thin polymer layer can maximize the plasmonic effect via interparticle coupling within the active interface of PSCs, resulting in enhanced performance in PSC.

ULSAN NATIONAL INSTITUTE OF SCIENCE AND TECHNOLOGY

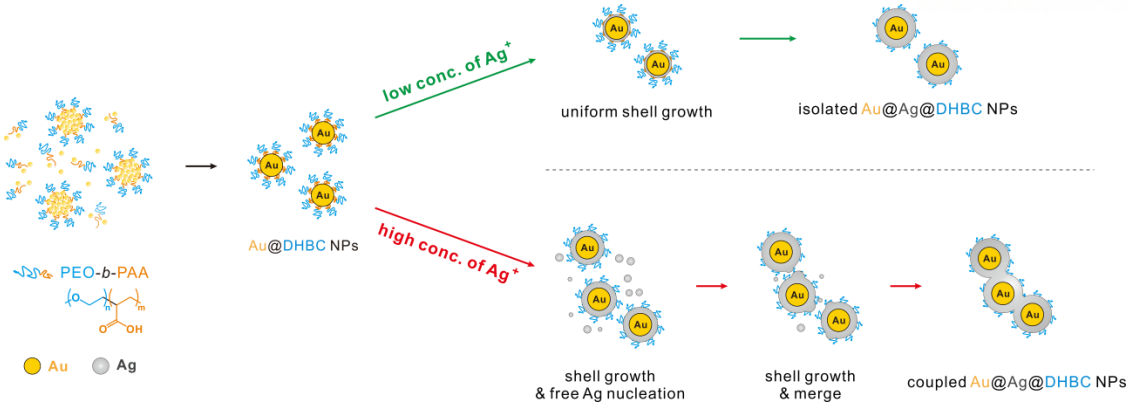

Scheme 3.2. Schematic Illustration of the Synthesis of Au-Ag Core-Shell NPs Using a Double Hydrophilic Block Copolymer Template (Au@Ag@DHBC NPs). Isolated and Coupled Au@Ag@DHBC NPs via a Seed Growth Method Are Determined by the Concentration of Ag Precursor.

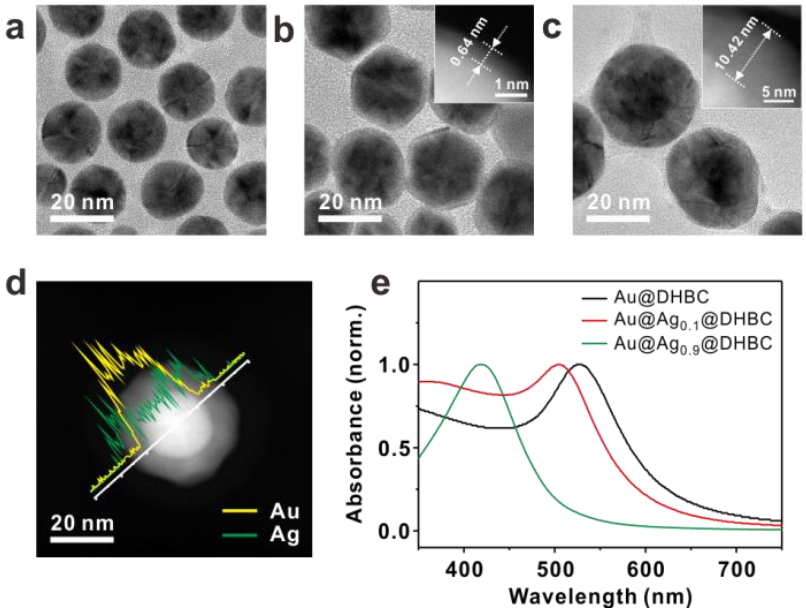

Figure 3.20. Isolated Au@Ag NPs by DHBC. TEM images of (a) Au@DHBC NPs and (b, c) Au@Ag@DHBC NPs synthesized by 0.1 and 0.9 μmol $AgNO_3$, denoted as Au@$Ag_{0.1}$@DHBC NPs and Au@$Ag_{0.9}$@DHBC NPs, respectively. Inset Figures in b and c show the dark field STEM images of Au@Ag@DHBC NPs. (d) Compositional line profiles of representative Au@Ag@DHBC NPs shown in Figure 1c. (e) UV-Vis spectra of Au@DHBC NPs and Au@Ag@DHBC NPs.

ULSAN NATIONAL INSTITUTE OF SCIENCE AND TECHNOLOGY

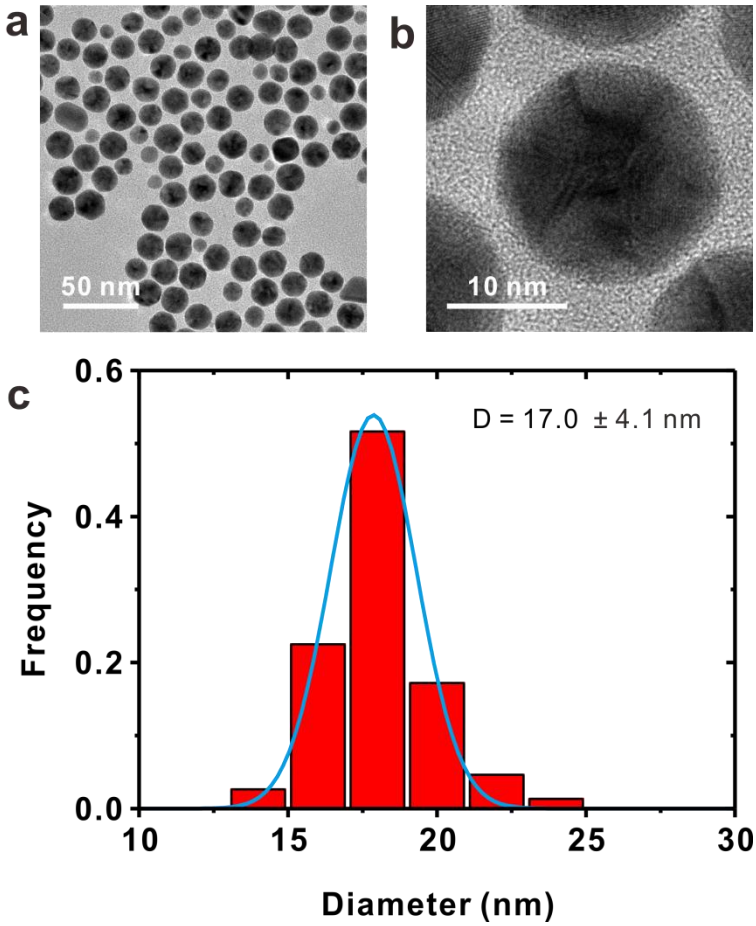

Figure 3.21. (a, b) Representative TEM images and (c) size distribution of Au@DHBC NPs prepared by modified method.[83] Specifically, the DHBC poly(ethylene oxide)-*block*-poly(acrylic acid) (PEO-*b*-PAA) is used as both a template and stabilizer for Au NPs. Typically, the carboxylate group of the PAA block interacts with the Au precursor via coordinative bonding between the metal precursor and the carboxylate group. Then, the PAA blocks segregate to form micellar structures in solution. Once the micelle formation is induced, the PEO-*b*-PAA micelle acts as a nanoreactor to template the growth of the Au NP within the micellar core upon the addition of a reducing agent, *L*-ascorbic acid. As the Au precursor is reduced to Au NPs, the transparent yellow solution turns reddish, indicating the formation of Au NPs. The average diameter of the Au NPs formed within the DHBC template (Au@DHBC NPs) is 17.0 ± 4.1 nm.

ULSAN NATIONAL INSTITUTE OF SCIENCE AND TECHNOLOGY

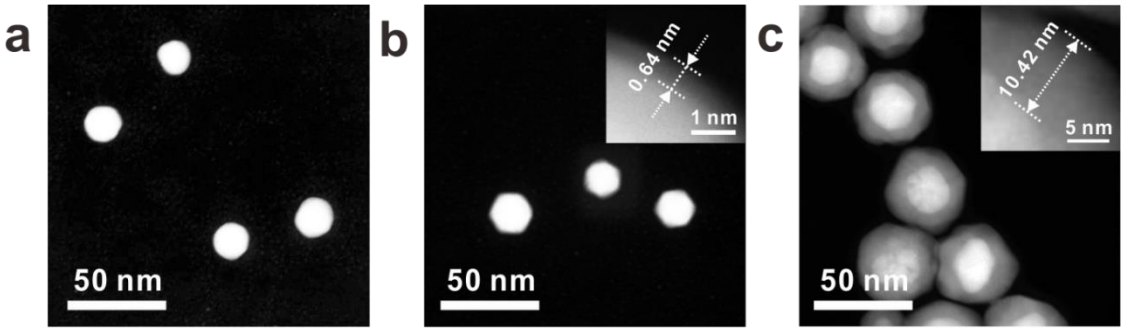

Figure 3.22. Low-magnification dark field HAADF STEM images of (a) Au@DHBC NPs, (b) Au@$Ag_{0.1}$@DHBC NPs, and (c) Au@$Ag_{0.9}$@DHBC NPs. Insets in b and c show the high resolution dark field TEM images of Au@Ag@DHBC NPs.

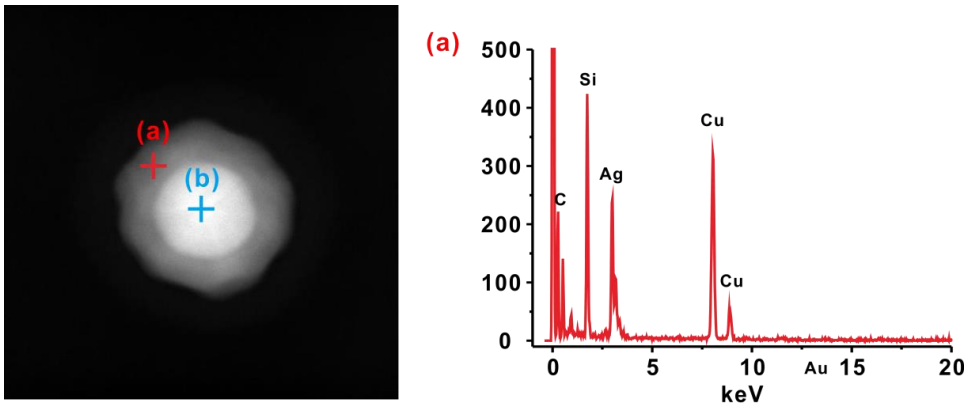

(a)

Element	Wt%
Ag	97.16
Au	2.84

(b)

Element	Wt%
Ag	13.56
Au	86.44

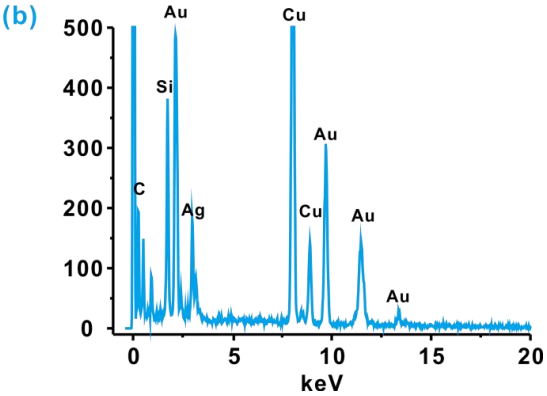

Figure 3.23. STEM analysis of representative Au@Ag@DHBC NPs. (a-b) Energy dispersive X-ray spectroscopy data of core-shell structure showing the component of Au and Ag at the different site of nanoparticles. The other atoms are observed because of the TEM grid.

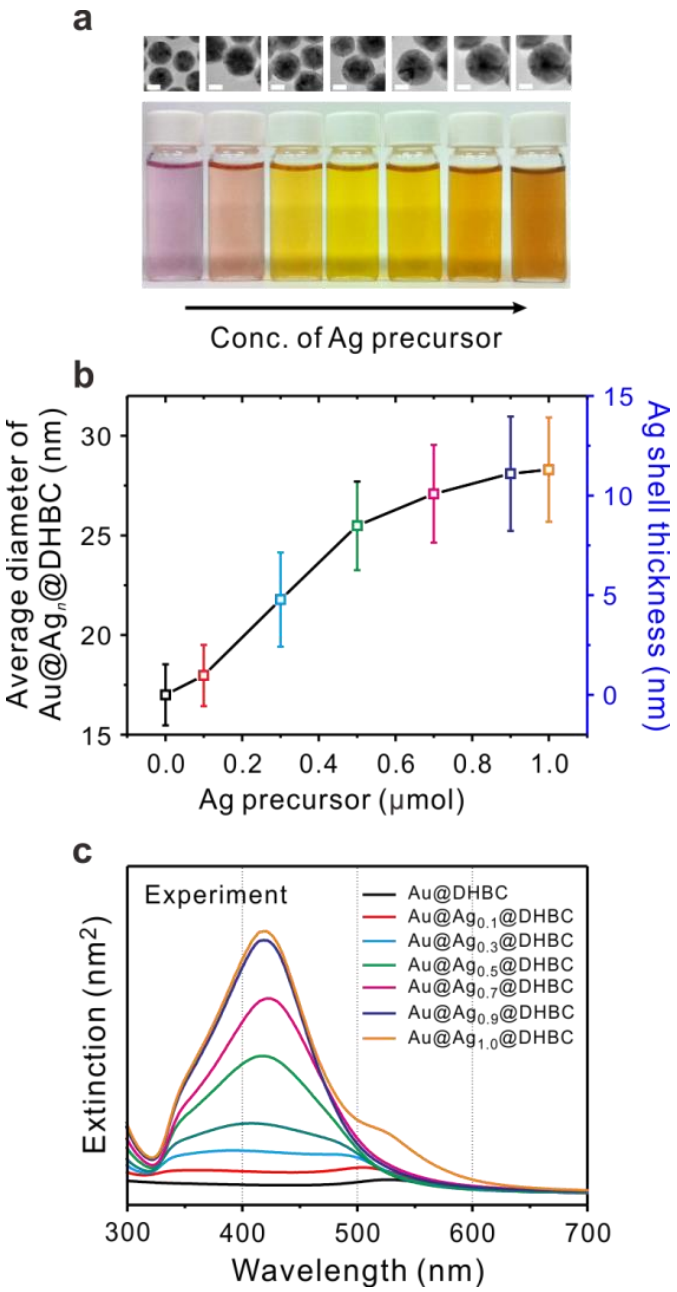

Figure 3.24. (a) (top) A series of TEM images and (bottom) their corresponding photographs of the Au@Ag@DHBC solution. The scale bar in the TEM images is 10 nm. (b) Average size of Au@Ag$_n$@DHBC NPs as a function of the concentration of Ag precursors (n = 0.0-1.0) and their corresponding Ag shell thickness. (c) UV-Vis spectra collected for Au@Ag$_n$@DHBC NPs produced with different concentrations of Ag precursor (n = 0.0-1.0).

ULSAN NATIONAL INSTITUTE OF SCIENCE AND TECHNOLOGY

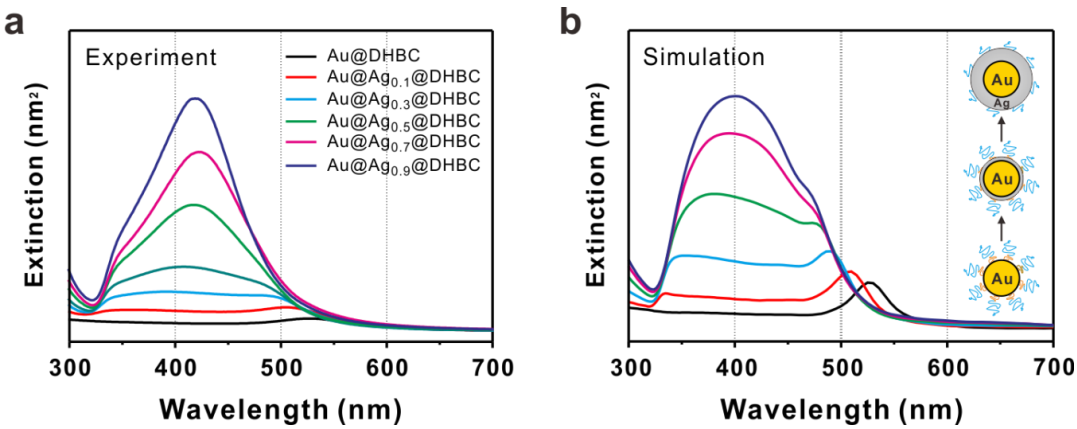

Figure 3.25. A comparison of the (a) UV-Vis spectra and (b) FDTD simulation results collected for Au@Ag$_n$@DHBC NPs produced with different concentrations of Ag precursor (n = 0.0 – 0.9). The experiment data indicates that the plasmon bands of the NPs initially blue-shifted and then exhibited strong absorption with increasing Ag shell thickness, showing a similar trend as the simulation data.

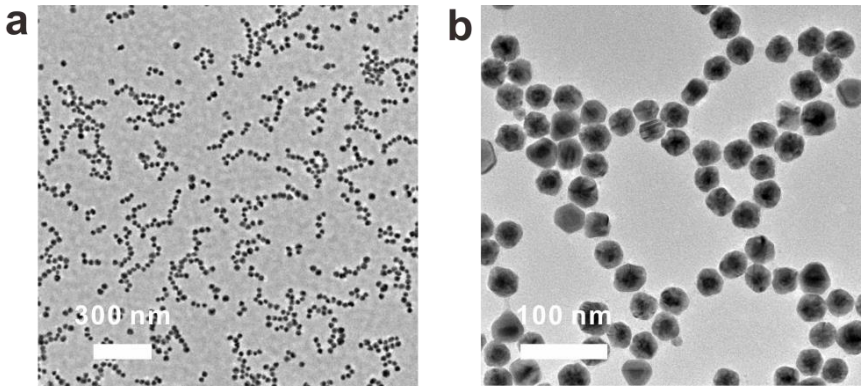

Figure 3.26. (a) Low and (b) high-resolution TEM images of Au@Ag$_{0.9}$@DHBC NPs.

ULSAN NATIONAL INSTITUTE OF SCIENCE AND TECHNOLOGY

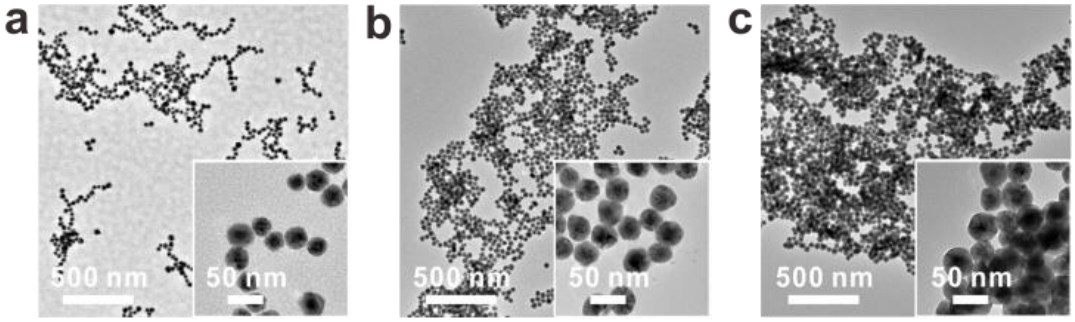

Figure 3.27. Coupled Au@Ag NPs by DHBC. (a-c) TEM images of Au@Ag@DHBC NPs synthesized by (a) 1.0, (b) 1.4 and (c) 1.8 μmol of Ag precursor, denoted as Au@$Ag_{1.0}$@DHBC, Au@$Ag_{1.4}$@DHBC and Au@$Ag_{1.8}$@DHBC, respectively.

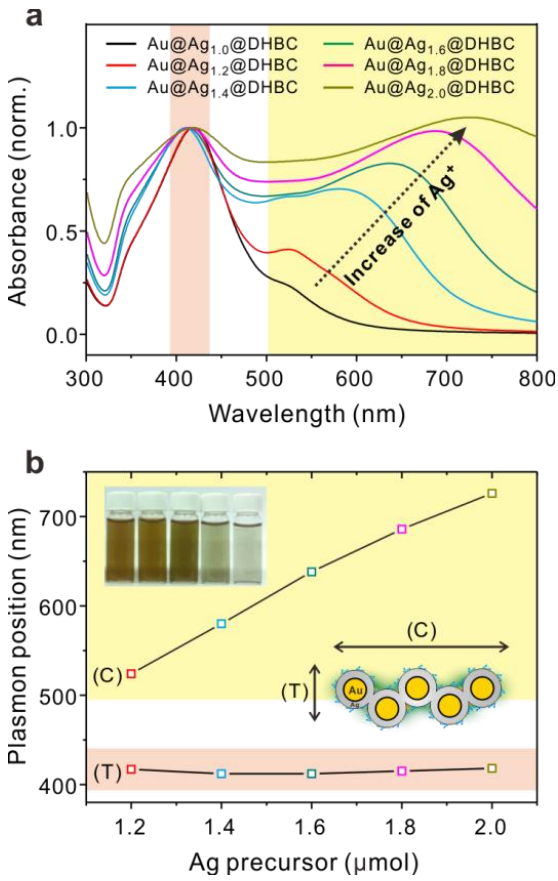

Figure 3.28. (a) UV-Vis absorption spectra of Au@Ag@DHBC with Ag precursor concentrations in the range of 1.0 to 2.0 μmol and (b) the corresponding plasmon band plots of Au@Ag@DHBC NPs by transverse absorption (line T) and plasmon coupling (line C).

ULSAN NATIONAL INSTITUTE OF SCIENCE AND TECHNOLOGY

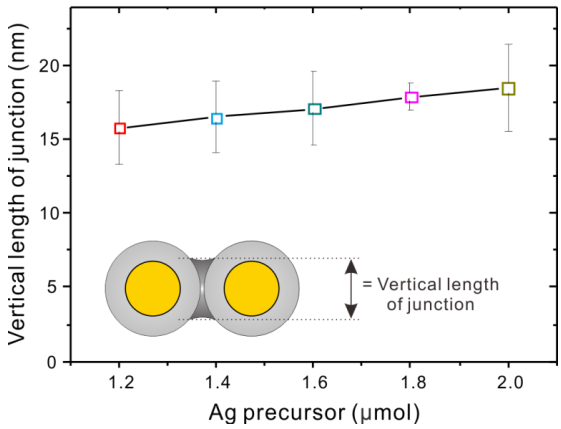

Figure 3.29. The plot showing vertical length of junction formed between NPs as a function of Ag precursor. Inset indicating the area of junction and corresponding vertical length.

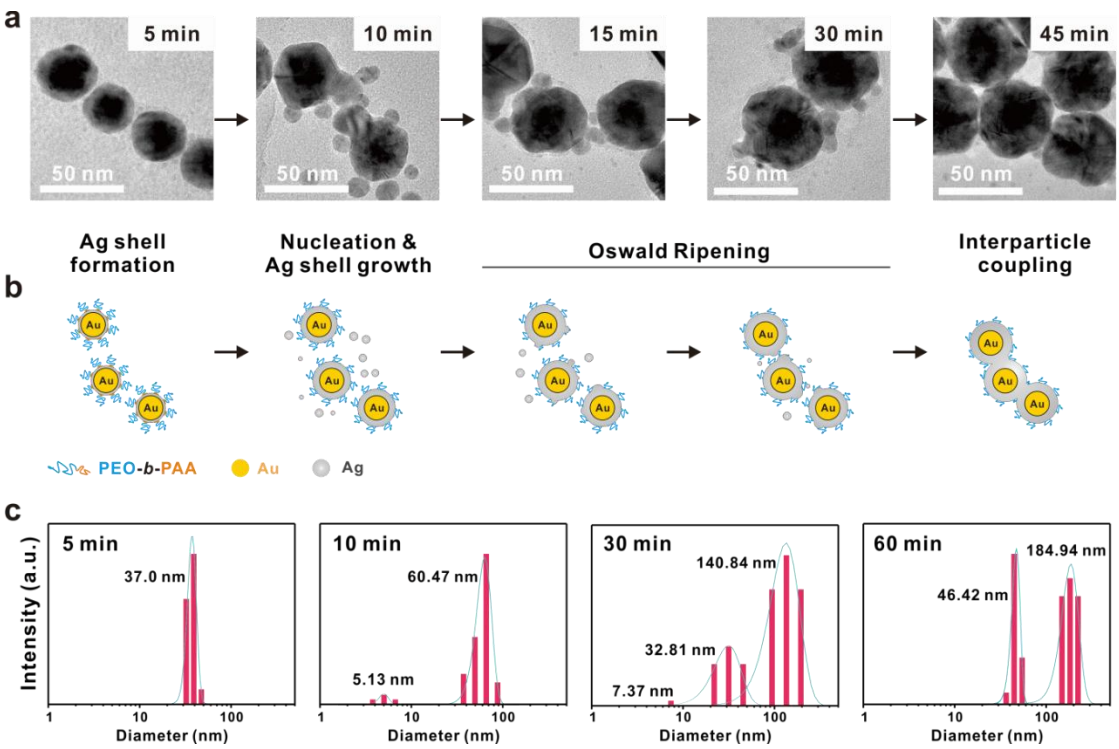

Figure 3.30. (a) A series of TEM images of Au@$Ag_{1.6}$@DHBC as a function of reaction time (5, 10, 15, 30, and 45 min). (b) Schematic drawings of the growth of the Ag layer and interparticle coupling. (c) Dynamic light scattering (DLS) analysis showing the hydrodynamic diameter changes during the growth of Au@$Ag_{1.6}$@DHBC NPs.

ULSAN NATIONAL INSTITUTE OF SCIENCE AND TECHNOLOGY

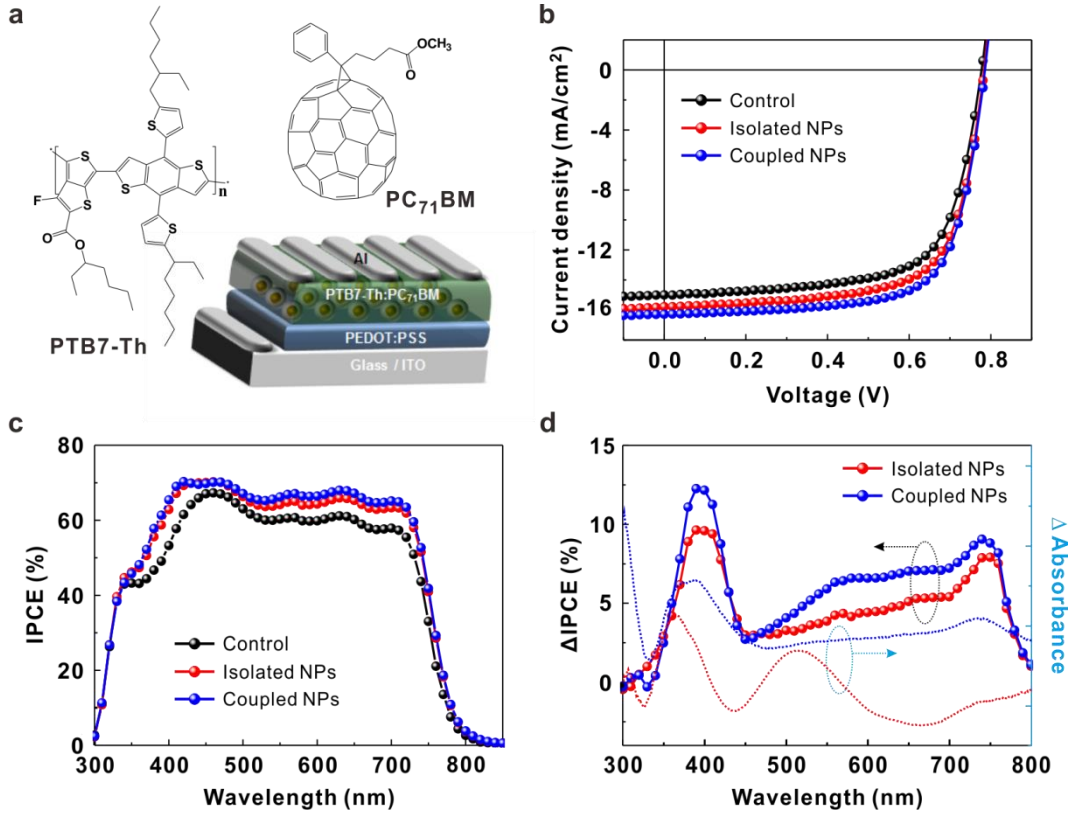

Figure 3.31. Device characteristics and spectral responses of plasmonic PSCs. (a) Schematic of polymer solar cell with chemical structures of PTB7-Th and $PC_{71}BM$, (b) current density-voltage (J-V) characteristics and (c) IPCE of a control device (black circles) and the best plasmonic PSCs with embedded Au@Ag@DHBC NPs (red and blue circles). (d) Comparison of enhanced IPCE and absorbance by Au@Ag@DHBC NPs.

ULSAN NATIONAL INSTITUTE OF SCIENCE AND TECHNOLOGY

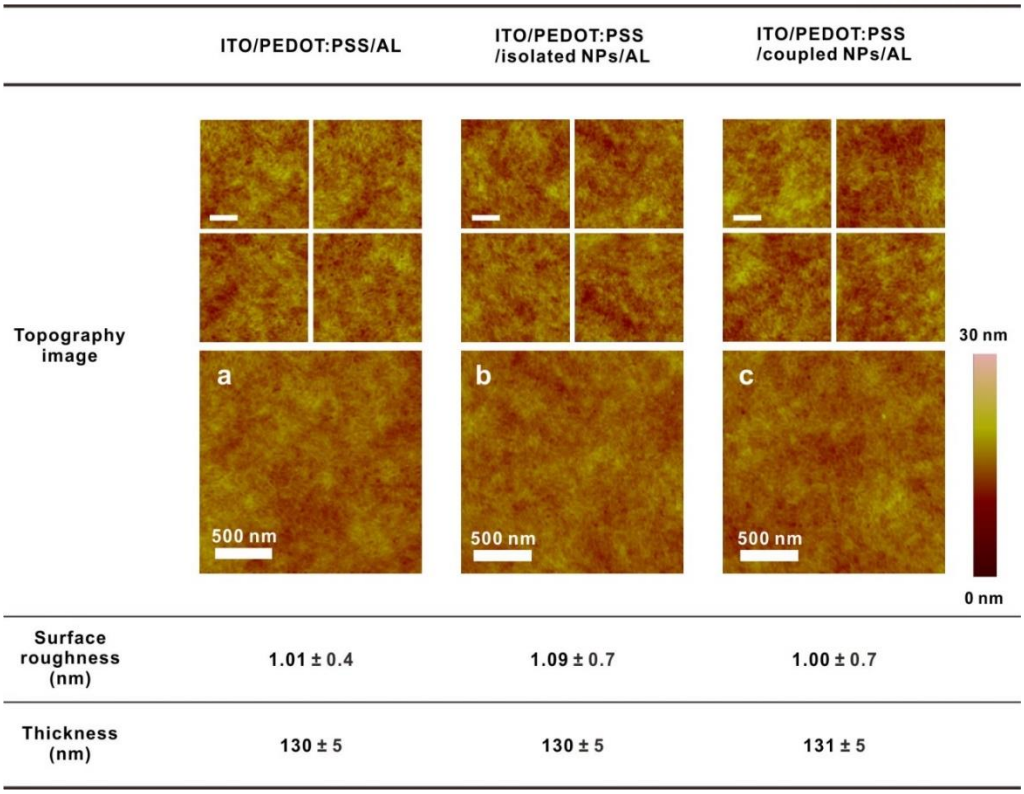

Figure 3.32. AFM images of active layer with configurations of (a) ITO/PEDOT:PSS/active layer, (b) ITO/PEDOT:PSS/isolated NPs/active layer, and (c) ITO/PEDOT:PSS/coupled NPs/active layer. Scale bar in all images represents 500 nm. The thickness of the films was measured with profilometer.

Table 3.4. Device Characteristics of PTB7-Th:$PC_{71}BM$-based PSCs with Au@Ag@DHBC NPs

Device configuration	Plasmonic NPs		J_{SC} (mA/cm^2)	V_{OC} (V)	FF	PCE (%)	J_{SC} [cal.] (mA/cm^2)
ITO/PEDOT:PSS/ AL[a]/Al	None (control)	Best	14.53	0.78	0.68	7.77	14.41
		Average	14.12 ± 0.41	0.78 ± 0.00	0.67 ± 0.01	7.37 ± 0.40	
ITO/PEDOT:PSS/ isolated NPs/AL[a]/Al	Au@$Ag_{0.9}$@DHBC	Best	15.78	0.78	0.69	8.51	15.65
		Average	15.38 ± 0.40	0.78 ± 0.00	0.69 ± 0.00	8.35 ± 0.19	
ITO/PEDOT:PSS/ coupled NPs/AL[a]/Al	Au@$Ag_{1.6}$@DHBC	Best	16.28	0.79	0.70	9.00	16.08
		Average	16.04 ± 0.24	0.78 ± 0.01	0.69 ± 0.01	8.74 ± 0.26	

[a] AL: active layer consisting of PTB7-Th and $PC_{71}BM$

ULSAN NATIONAL INSTITUTE OF SCIENCE AND TECHNOLOGY

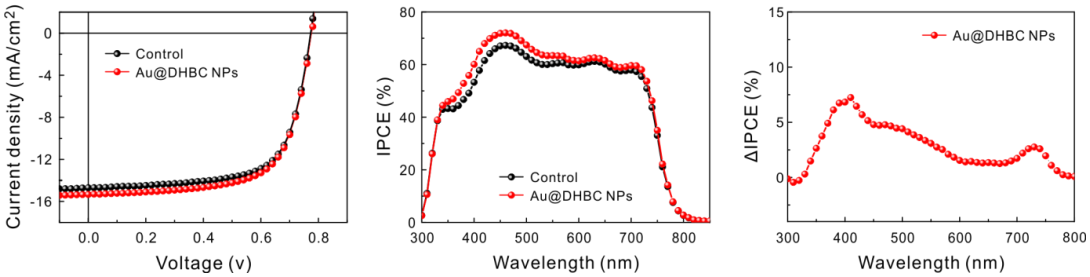

Figure 3.33. Device characteristics and spectral responses of plasmonic PSCs with and without Au@DHBC NPs. (a) Current density-voltage (J-V)w characteristics and (b) IPCE of a control device (black circles) and the best plasmonic PSCs with embedded Au@DHBC NPS (red circle). (c) Enhanced IPCE of device with Au@DHBC NPs in comparison with control device.

Table 3.5. Device Characteristics of PTB7-Th:$PC_{71}BM$-based PSCs with Au@DHBC NPs.

Device configuration	Plasmonic NPs		J_{SC} (mA/cm^2)	V_{OC} (V)	FF	PCE (%)	J_{SC} [cal.] (mA/cm^2)
ITO/PEDOT:PSS/AL[a]/Al	None (control)	Best	14.53	0.78	0.68	7.77	14.41
		Average	14.12 ± 0.41	0.78 ± 0.00	0.67 ± 0.01	7.37 ± 0.40	
ITO/PEDOT:PSS/ Au@DHBC NPs/AL[a]/Al	Au@DHBC NPs	Best	15.30	0.78	0.67	8.01	15.18
		Average	15.12 ± 0.18	0.77 ± 0.01	0.69 ± 0.00	7.86 ± 0.15	

[a] AL: active layer consisting of PTB7-Th and $PC_{71}BM$

ULSAN NATIONAL INSTITUTE OF
SCIENCE AND TECHNOLOGY

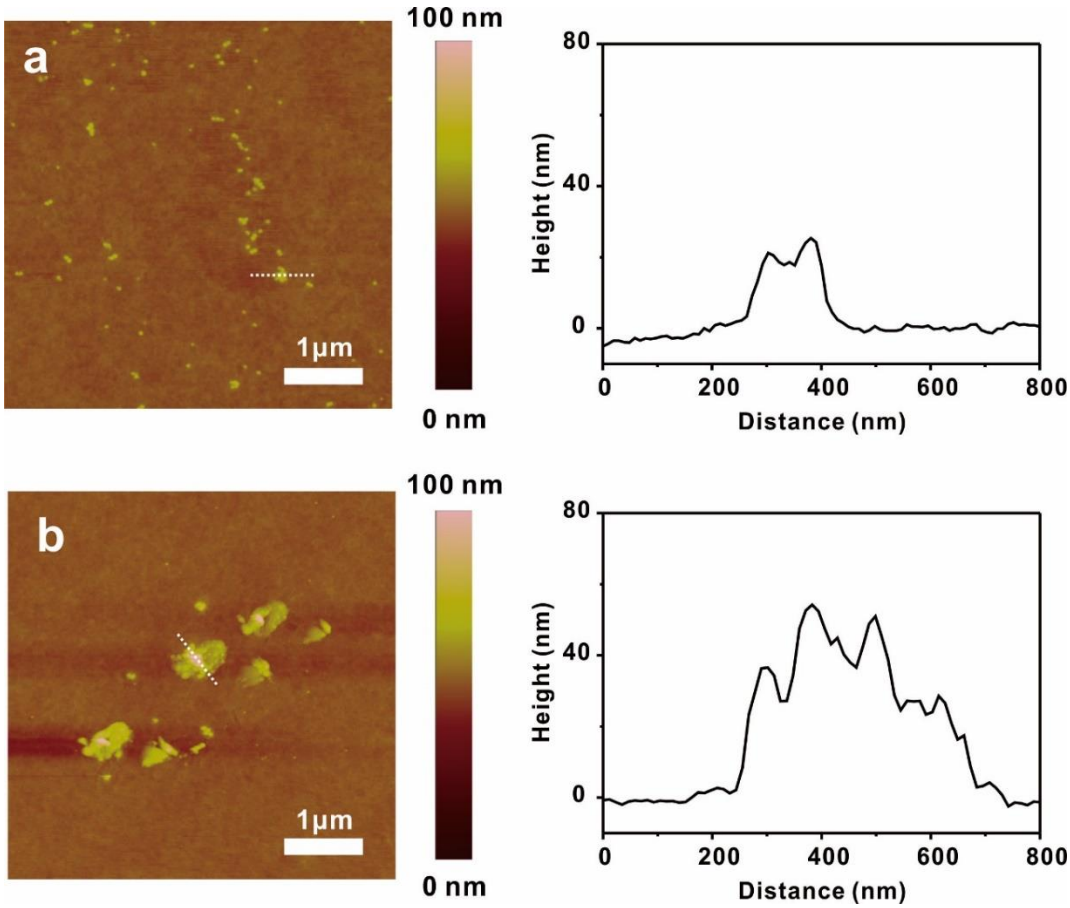

Figure 3.34. Representative height-mode AFM images of PEDOT:PSS film coated with (a) isolated Au@$Ag_{0.9}$@DHBC NPs and (b) coupled Au@$Ag_{1.6}$@DHBC NPs. The images were taken with NPs solutions after filtration.

ULSAN NATIONAL INSTITUTE OF
SCIENCE AND TECHNOLOGY

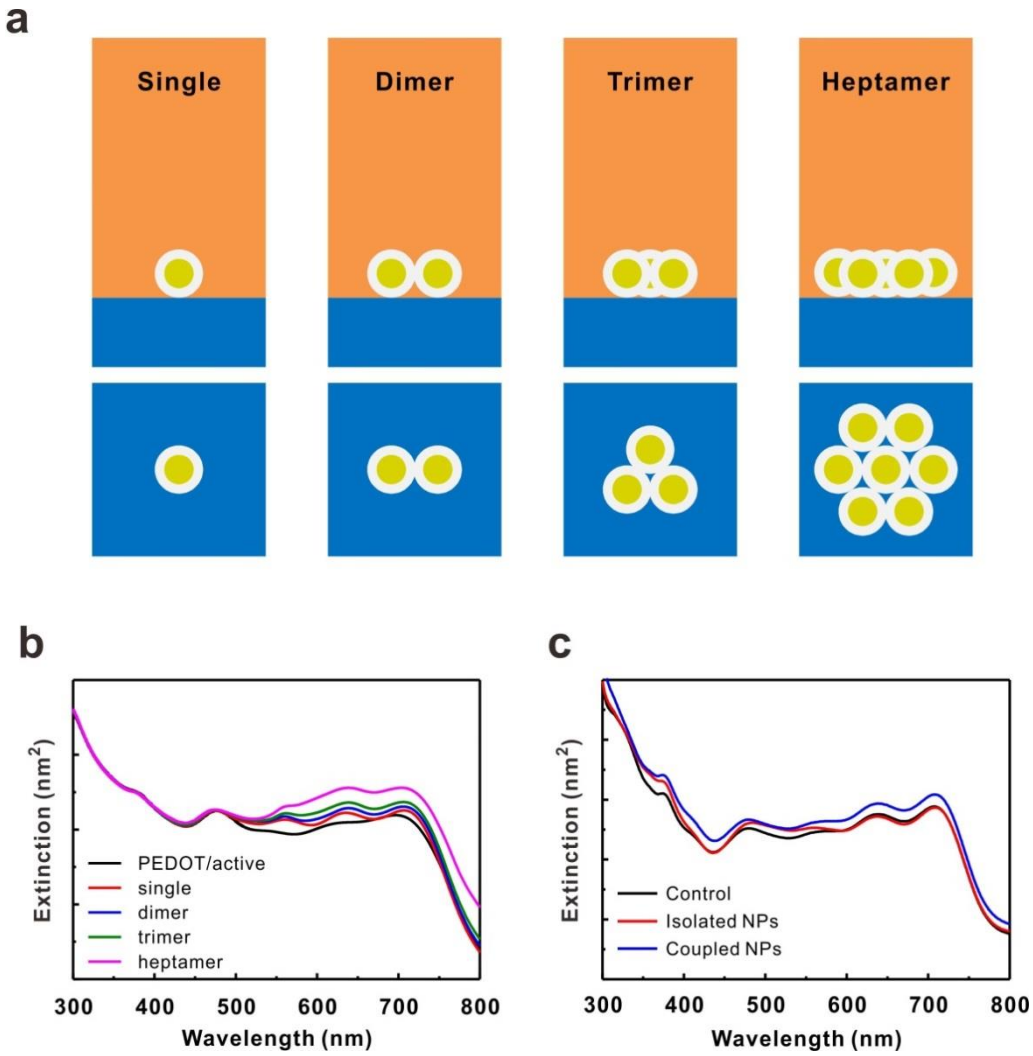

Figure 3.35. (a) Schematic description of different arrangement of plasmonic Au@Ag@DHBC NPs embedded within active layer on the device and (b) corresponding FDTD simulated extinction. (c) UV-Vis spectra of PTB7/$PC_{71}BM$ without NPs and with isolated Au@$Ag_{0.9}$@DHBC NPs or coupled Au@$Ag_{1.6}$@DHBC NPs.

ULSAN NATIONAL INSTITUTE OF
SCIENCE AND TECHNOLOGY

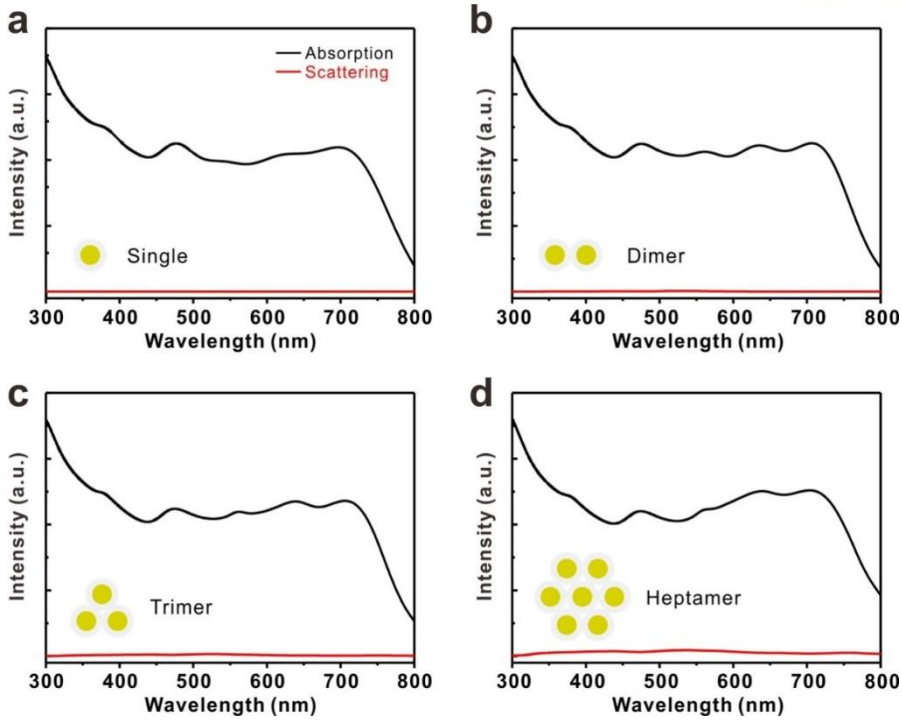

Figure 3.36. The absorption and scattering spectra on the device with plasmonic Au@Ag core-shell NPs, which is analyzed using FDTD simulation.

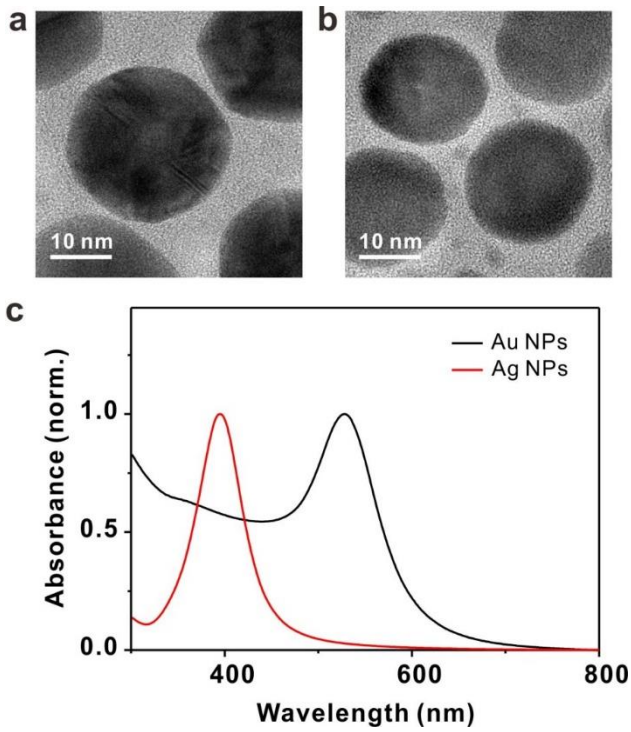

Figure 3.37. (a, b) Representative TEM images of (a) free Au and (b) free Ag NPs without DHBC and (c) normalized UV-vis spectra of Au and Ag NP solutions.

ULSAN NATIONAL INSTITUTE OF SCIENCE AND TECHNOLOGY

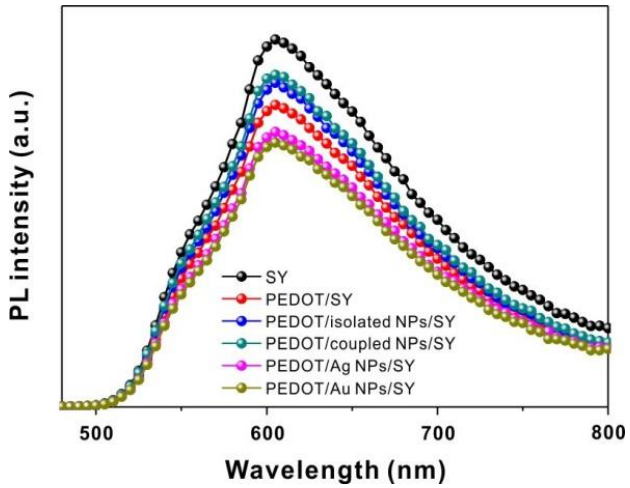

Figure 3.38. Steady-state photoluminescence (PL) spectra of fluorescence of SY films by the effect of isolated and coupled NPs (Au@$Ag_{0.9}$@DHBC and Au@$Ag_{1.6}$@DHBC NPs, respectively) and free Au and Ag NPs synthesized without DHBC template.

Table 3.6. PL quantum efficiency (PLQE) of films with different configurations measured inside an integrating sphere with an excitation wavelength of 470 nm.

Configuration	PLQE (%)
Glass/SY[a]	19.79
Glass/PEDOT:PSS/SY	11.83
Glass/PEDOT:PSS/isolated NPs/SY	12.36
Glass/PEDOT:PSS/coupled NPs/SY	13.64
Glass/PEDOT:PSS/Ag NPs/SY	10.78
Glass/PEDOT:PSS/Au NPs/SY	10.07

[a] Thickness of SY film: 30 nm

ULSAN NATIONAL INSTITUTE OF SCIENCE AND TECHNOLOGY

3.4. Conclusion

We have developed core-shell nanostructures using the double hydrophilic block copolymer (DHBC), PEO-*b*-PAA, as a soft template through coordinative and ion-dipole interactions between metal precursors and each segment of the DHBC. The DHBC used in this work is highly suitable to form core-shell nanostructures via the seed-mediated growth of NPs under mild ambient condition. The PAA block of the DHBC forms micellar structures with the Au precursor and then induces a spherical Au core, whereas the PEO block provides the stability for nanoparticles in aqueous solution as well as guidance for uniform Ag shell growth. Moreover, this PEO block facilitates interparticle coupling, which leads to the transition of new plasmon mode in the wide visible regions. The synthesized Au@Ag@DHBC NPs were successfully employed as plasmonic nanomaterials at the interface of an active layer, which considerably improved the efficiency of PSCs. We anticipate that DHBC-templated Au@Ag NPs would be widely applied as plasmonic materials in optoelectronic devices. In addition, this synthetic approach for the formation of NPs with DHBCs can lead to a facile and general method of producing core-shell nanostructures and tuning the intrinsic plasmonic effect of novel metal NPs for a variety of applications.

ULSAN NATIONAL INSTITUTE OF SCIENCE AND TECHNOLOGY

3.5. References

(1) Mayer, K. M.; Hafner, J. H. Localized Surface Plasmon Resonance Sensors. *Chem. Rev.* **2011**, *111*, 3828-3857.

(2) Atwater, H. A.; Polman, A. Plasmonics for Improved Photovoltaic Devices. *Nat. Mater.* **2010**, *9*, 205-213.

(3) Fan, J. A.; Wu, C.; Bao, K.; Bao, J.; Bardhan, R.; Halas, N. J.; Manoharan, V. N.; Nordlander, P.; Shvets, G.; Capasso, F. Self-Assembled Plasmonic Nanoparticle Clusters. *Science* **2010**, *328*, 1135-1138.

(4) Jana, N. R.; Gearheart, L.; Murphy, C. J. Seed-Mediated Growth Approach for Shape-Controlled Synthesis of Spheroidal and Rod-like Gold Nanoparticles Using a Surfactant Template. *Adv. Mater.* **2001**, *13*, 1389-1393.

(5) Zhao, Q.; Ji, M.; Qian, H.; Dai, B.; Weng, L.; Gui, J.; Zhang, J.; Ouyang, M.; Zhu, H. Controlling Structural Symmetry of a Hybrid Nanostructure and Its Effect on Efficient Photocatalytic Hydrogen Evolution. *Adv. Mater.* **2014**, *26*, 1387-1392.

(6) Wiley, B. J.; Im, S. H.; Li, Z.-Y.; McLellan, J.; Siekkinen, A.; Xia, Y. Maneuvering the Surface Plasmon Resonance of Silver Nanostructures through Shape-Controlled Synthesis. *J. Phys. Chem. B* **2006**, *110*, 15666-15675.

(7) DeSantis, C. J.; Weiner, R. G.; Radmilovic, A.; Bower, M. M.; Skrabalak, S. E. Seeding Bimetallic Nanostructures as a New Class of Plasmonic Colloids. *J. Phys. Chem. Lett.* **2013**, *4*, 3072-3082.

(8) Feng, Y.; He, J.; Wang, H.; Tay, Y. Y.; Sun, H.; Zhu, L.; Chen, H. An Unconventional Role of Ligand in Continuously Tuning of Metal–Metal Interfacial Strain. *J. Am. Chem. Soc.* **2012**, *134*, 2004-2007.

(9) Kang, Y.; Erickson, K. J.; Taton, T. A. Plasmonic Nanoparticle Chains via a Morphological, Sphere-to-String Transition. *J. Am. Chem. Soc.* **2005**, *127*, 13800-13801.

(10) Mulvihill, M. J.; Ling, X. Y.; Henzie, J.; Yang, P. Anisotropic Etching of Silver Nanoparticles for Plasmonic Structures Capable of Single-Particle SERS. *J. Am. Chem. Soc.* **2009**, *132*, 268-274.

(11) Cho, E. C.; Choi, S.-W.; Camargo, P. H.; Xia, Y. Thiol-Induced Assembly of Au Nanoparticles into Chainlike Structures and Their Fixing by Encapsulation in Silica Shells or Gelatin Microspheres. *Langmuir* **2010**, *26*, 10005-10012.

ULSAN NATIONAL INSTITUTE OF SCIENCE AND TECHNOLOGY

(12) Yang, M.; Chen, G.; Zhao, Y.; Silber, G.; Wang, Y.; Xing, S.; Han, Y.; Chen, H. Mechanistic Investigation into the Spontaneous Linear Assembly of Gold Nanospheres. *Phys. Chem. Chem. Phys.* **2010**, *12*, 11850-11860.

(13) Peng, S.; McMahon, J. M.; Schatz, G. C.; Gray, S. K.; Sun, Y. Reversing the Size-Dependence of Surface Plasmon Resonances. *Proc. Natl. Acad. Sci.* **2010**, *107*, 14530-14534.

(14) Jiang, R.; Chen, H.; Shao, L.; Li, Q.; Wang, J. Unraveling the Evolution and Nature of the Plasmons in (Au Core)–(Ag Shell) Nanorods. *Adv. Mater.* **2012**, *24*, OP200-OP207.

(15) Kelly, K. L.; Coronado, E.; Zhao, L. L.; Schatz, G. C. The Optical Properties of Metal Nanoparticles: The Influence of Size, Shape, and Dielectric Environment. *J. Phys. Chem. B* **2003**, *107*, 668-677.

(16) Jang, L. W.; Jeon, D. W.; Kim, M.; Jeon, J. W.; Polyakov, A. Y.; Ju, J. W.; Lee, S. J.; Baek, J. H.; Yang, J. K.; Lee, I. H. Investigation of Optical and Structural Stability of Localized Surface Plasmon Mediated Light-Emitting Diodes by Ag and Ag/SiO_2 Nanoparticles. *Adv. Funct. Mater.* **2012**, *22*, 2728-2734.

(17) Zhang, L.; Song, Y.; Fujita, T.; Zhang, Y.; Chen, M.; Wang, T. H. Large Enhancement of Quantum Dot Fluorescence by Highly Scalable Nanoporous Gold. *Adv. Mater.* **2013**, *26*, 1289-1294.

(18) Choi, H.; Lee, J.-P.; Ko, S.-J.; Jung, J.-W.; Park, H.; Yoo, S.; Park, O.; Jeong, J.-R.; Park, S.; Kim, J. Y. Multipositional Silica-Coated Silver Nanoparticles for High-Performance Polymer Solar Cells. *Nano Lett.* **2013**, *13*, 2204-2208.

(19) Sotiriou, G. A.; Sannomiya, T.; Teleki, A.; Krumeich, F.; Vörös, J.; Pratsinis, S. E. Non-Toxic Dry-Coated Nanosilver for Plasmonic Biosensors. *Adv. Funct. Mater.* **2010**, *20*, 4250-4257.

(20) Nam, J.; Won, N.; Jin, H.; Chung, H.; Kim, S. pH-Induced Aggregation of Gold Nanoparticles for Photothermal Cancer Therapy. *J. Am. Chem. Soc.* **2009**, *131*, 13639-13645.

(21) Wang, Y.; Liu, Y.; Luehmann, H.; Xia, X.; Wan, D.; Cutler, C.; Xia, Y. Radioluminescent Gold Nanocages with Controlled Radioactivity for Real-Time in vivo Imaging. *Nano Lett.* **2013**, *13*, 581-585.

(22) Samal, A. K.; Polavarapu, L.; Rodal-Cedeira, S.; Liz-Marzán, L. M.; Pérez-Juste, J.; Pastoriza-Santos, I. Size Tunable Au@Ag Core–Shell Nanoparticles: Synthesis and

ULSAN NATIONAL INSTITUTE OF SCIENCE AND TECHNOLOGY

Surface-Enhanced Raman Scattering Properties. *Langmuir* **2013**, *29*, 15076-15082.

(23) Yang, J.; You, J.; Chen, C.-C.; Hsu, W.-C.; Tan, H.-r.; Zhang, X. W.; Hong, Z.; Yang, Y. Plasmonic Polymer Tandem Solar Cell. *ACS Nano* **2011**, *5*, 6210-6217.

(24) Lu, L.; Luo, Z.; Xu, T.; Yu, L. Cooperative Plasmonic Effect of Ag and Au Nanoparticles on Enhancing Performance of Polymer Solar Cells. *Nano Lett.* **2012**, *13*, 59-64.

(25) Wang, D. H.; Park, K. H.; Seo, J. H.; Seifter, J.; Jeon, J. H.; Kim, J. K.; Park, J. H.; Park, O. O.; Heeger, A. J. Enhanced Power Conversion Efficiency in PCDTBT/$PC_{70}BM$ Bulk Heterojunction Photovoltaic Devices with Embedded Silver Nanoparticle Clusters. *Adv. Energy Mater.* **2011**, *1*, 766-770.

(26) Wang, D. H.; Kim, D. Y.; Choi, K. W.; Seo, J. H.; Im, S. H.; Park, J. H.; Park, O. O.; Heeger, A. J. Enhancement of Donor-Acceptor Polymer Bulk Heterojunction Solar Cell Power Conversion Efficiencies by Addition of Au Nanoparticles. *Angew. Chem., Int. Ed.* **2011**, *50*, 5519-5523.

(27) Baek, S.-W.; Park, G.; Noh, J.; Cho, C.; Lee, C.-H.; Seo, M.-K.; Song, H.; Lee, J.-Y. Au@Ag Core-Shell Nanocubes for Efficient Plasmonic Light Scattering Effect in Low Bandgap Organic Solar Cells. *ACS Nano* **2014**, *8*, 3302-3312.

(28) Jankovic, V.; Yang, Y.; You, J.; Dou, L.; Liu, Y.; Cheung, P.; Chang, J. P. Active Layer-Incorporated, Spectrally Tuned Au/SiO_2 Core/Shell Nanorod-Based Light Trapping for Organic Photovoltaics. *ACS Nano* **2013**, *7*, 3815-3822.

(29) Wu, J.-L.; Chen, F.-C.; Hsiao, Y.-S.; Chien, F.-C.; Chen, P.; Kuo, C.-H.; Huang, M. H.; Hsu, C.-S. Surface Plasmonic Effects of Metallic Nanoparticles on the Performance of Polymer Bulk Heterojunction Solar Cells. *ACS Nano* **2011**, *5*, 959-967.

(30) Li, X.; Choy, W. C. H.; Lu, H.; Sha, W. E.; Ho, A. H. P. Efficiency Enhancement of Organic Solar Cells by Using Shape-Dependent Broadband Plasmonic Absorption in Metallic Nanoparticles. *Adv. Funct. Mater.* **2013**, *23*, 2728-2735.

(31) Choi, H.; Ko, S. J.; Choi, Y.; Joo, P.; Kim, T.; Lee, B. R.; Jung, J. W.; Choi, H. J.; Cha, M.; Jeong, J. R.; Hwang, I. W.; Song, M. H.; Kim, B. S.; Kim, J. Y. Versatile Surface Plasmon Resonance of Carbon-Dot-Supported Silver Nanoparticles in Polymer Optoelectronic Devices. *Nat. Photonics* **2013**, *7*, 732-738.

(32) Xu, H.; Xu, Y.; Pang, X.; He, Y.; Jung, J.; Xia, H.; Lin, Z. A General Route to Nanocrystal Kebabs Periodically Assembled on Stretched Flexible Polymer Shish. *Sci.*

ULSAN NATIONAL INSTITUTE OF SCIENCE AND TECHNOLOGY

Adv. **2015**, *1*, e1500025.

(33) Pang, X.; Zhao, L.; Feng, C.; Lin, Z. Novel Amphiphilic Multiarm, Starlike Coil–Rod Diblock Copolymers via a Combination of Click Chemistry with Living Polymerization. *Macromolecules* **2011**, *44*, 7176-7183.

(34) Xu, H.; Pang, X.; He, Y.; He, M.; Jung, J.; Xia, H.; Lin, Z. An Unconventional Route to Monodisperse and Intimately Contacted Semiconducting Organic–Inorganic Nanocomposites. *Angew. Chem.* **2015**, *127*, 4719-4723.

(35) Mistark, P. A.; Park, S.; Yalcin, S. E.; Lee, D. H.; Yavuzcetin, O.; Tuominen, M. T.; Russell, T. P.; Achermann, M. Block-Copolymer-Based Plasmonic Nanostructures. *ACS Nano* **2009**, *3*, 3987-3992.

(36) Shin, D. O.; Mun, J. H.; Hwang, G.-T.; Yoon, J. M.; Kim, J. Y.; Yun, J. M.; Yang, Y.-B.; Oh, Y.; Lee, J. Y.; Shin, J.; Lee, K. J.; Park, S.; Kim, J. U.; Kim, S. O. Multicomponent Nanopatterns by Directed Block Copolymer Self-Assembly. *ACS Nano* **2013**, *7*, 8899-8907.

(37) Leong, W. L.; Lee, P. S.; Lohani, A.; Lam, Y. M.; Chen, T.; Zhang, S.; Dodabalapur, A.; Mhaisalkar, S. G. Non-Volatile Organic Memory Applications Enabled by in situ Synthesis of Gold Nanoparticles in a Self-Assembled Block Copolymer. *Adv. Mater.* **2008**, *20*, 2325-2331.

(38) Wang, L.; Yamauchi, Y. Autoprogrammed Synthesis of Triple-Layered Au@Pd@Pt Core-Shell Nanoparticles Consisting of a Au@Pd Bimetallic Core and Nanoporous Pt Shell. *J. Am. Chem. Soc.* **2010**, *132*, 13636-13638.

(39) Pang, X. C.; Zhao, L.; Han, W.; Xin, X. K.; Lin, Z. Q. A General and Robust Strategy for the Synthesis of Nearly Monodisperse Colloidal Nanocrystals. *Nat. Nanotechnol.* **2013**, *8*, 426-431.

(40) Bastakoti, B. P.; Guragain, S.; Yusa, S.; Nakashima, K. Novel Synthesis Route for Ag@SiO_2 Core-Shell Nanoparticles via Micelle Template of Double Hydrophilic Block Copolymer. *RSC Adv.* **2012**, *2*, 5938-5940.

(41) Bastakoti, B. P.; Sukegawa, H.; Wu, K. C. W.; Yamauchi, Y. Synthesis of Porous Iron Oxide Microspheres by a Double Hydrophilic Block Copolymer. *RSC Adv.* **2014**, *4*, 9986-9989.

(42) Nakashima, K.; Bahadur, P. Aggregation of Water-Soluble Block Copolymers in Aqueous Solutions: Recent Trends. *Adv. Colloid Interface Sci.* **2006**, *123*, 75-96.

ULSAN NATIONAL INSTITUTE OF SCIENCE AND TECHNOLOGY

(43) Colfen, H. Double-Hydrophilic Block Copolymers: Synthesis and Application as Novel Surfactants and Crystal Growth Modifiers. *Macromol. Rapid Commun.* **2001**, *22*, 219-252.

(44) Seo, E.; Kim, J.; Hong, Y.; Kim, Y. S.; Lee, D.; Kim, B.-S. Double Hydrophilic Block Copolymer Templated Au Nanoparticles with Enhanced Catalytic Activity toward Nitroarene Reduction. *J. Phys. Chem. C* **2013**, *117*, 11686-11693.

(45) Palik, E. D. *Handbook of Optical Constants of Solids*; Academic press, 1998; Vol. 3.

(46) Luo, C.; Zhang, Y.; Zeng, X.; Zeng, Y.; Wang, Y. The Role of Poly(ethylene glycol) in the Formation of Silver Nanoparticles. *J. Colloid Interface Sci.* **2005**, *288*, 444-448.

(47) Voronov, A.; Kohut, A.; Vasylyev, S.; Peukert, W. Mechanism of Silver Ion Reduction in Concentrated Solutions of Amphiphilic Invertible Polyesters in Nonpolar Solvent at Room Temperature. *Langmuir* **2008**, *24*, 12587-12594.

(48) Jeong, S.; Woo, K.; Kim, D.; Lim, S.; Kim, J. S.; Shin, H.; Xia, Y.; Moon, J. Controlling the Thickness of the Surface Oxide Layer on Cu Nanoparticles for the Fabrication of Conductive Structures by Ink-Jet Printing. *Adv. Funct. Mater.* **2008**, *18*, 679-686.

(49) Washio, I.; Xiong, Y.; Yin, Y.; Xia, Y. Reduction by the End Groups of Poly(vinyl pyrrolidone): A New and Versatile Route to the Kinetically Controlled Synthesis of Ag Triangular Nanoplates. *Adv. Mater.* **2006**, *18*, 1745-1749.

(50) Zhang, Q.; Xie, J.; Yang, J.; Lee, J. Y. Monodisperse Icosahedral Ag, Au, and Pd Nanoparticles: Size Control Strategy and Superlattice Formation. *ACS Nano* **2009**, *3*, 139-148.

(51) Wen, F.; Ye, J.; Liu, N.; Van Dorpe, P.; Nordlander, P.; Halas, N. J. Plasmon Transmutation: Inducing New Modes in Nanoclusters by Adding Dielectric Nanoparticles. *Nano Lett.* **2012**, *12*, 5020-5026.

(52) He, J.; Liu, Y.; Babu, T.; Wei, Z.; Nie, Z. Self-Assembly of Inorganic Nanoparticle Vesicles and Tubules Driven by Tethered Linear Block Copolymers. J. Am. Chem. Soc. 201**2**, *134*, 11342-11345.

(53) Jana, N. R.; Gearheart, L.; Murphy, C. J. Seeding Growth for Size Control of 5-40 nm Diameter Gold Nanoparticles. *Langmuir* **2001**, *17*, 6782-6786.

(54) Talley, C. E.; Jackson, J. B.; Oubre, C.; Grady, N. K.; Hollars, C. W.; Lane, S. M.;

ULSAN NATIONAL INSTITUTE OF SCIENCE AND TECHNOLOGY

Huser, T. R.; Nordlander, P.; Halas, N. J. Surface-Enhanced Raman Scattering from Individual Au Nanoparticles and Nanoparticle Dimer Substrates. *Nano Lett.* **2005**, *5*, 1569-1574.

(55) Lee, H.; Lee, J.-H.; Jin, S. M.; Suh, Y. D.; Nam, J.-M. Single-Molecule and Single-Particle-Based Correlation Studies between Localized Surface Plasmons of Dimeric Nanostructures with ～1 nm Gap and Surface-Enhanced Raman Scattering. *Nano Lett.* **2013**, *13*, 6113-6121.

(56) Atay, T.; Song, J.-H.; Nurmikko, A. V. Strongly Interacting Plasmon Nanoparticle Pairs: From Dipole-Dipole Interaction to Conductively Coupled Regime. *Nano Lett.* **2004**, *4*, 1627-1631.

(57) Lassiter, J. B.; Aizpurua, J.; Hernandez, L. I.; Brandl, D. W.; Romero, I.; Lal, S.; Hafner, J. H.; Nordlander, P.; Halas, N. J. Close Encounters between Two Nanoshells. *Nano Lett.* **2008**, *8*, 1212-1218.

(58) Lee, J.-H.; You, M.-H.; Kim, G.-H.; Nam, J.-M. Plasmonic Nanosnowmen with a Conductive Junction as Highly Tunable Nanoantenna Structures and Sensitive, Quantitative and Multiplexable Surface-Enhanced Raman Scattering Probes. *Nano Lett.* **2014**, *14*, 6217-6225.

(59) Romero, I.; Aizpurua, J.; Bryant, G. W.; García De Abajo, F. J. Plasmons in Nearly Touching Metallic Nanoparticles: Singular Response in the Limit of Touching Dimers. *Opt. Express* **2006**, *14*, 9988-9999.

(60) Liao, S.-H.; Jhuo, H.-J.; Cheng, Y.-S.; Chen, S.-A. Fullerene Derivative-Doped Zinc Oxide Nanofilm as the Cathode of Inverted Polymer Solar Cells with Low-Bandgap Polymer (PTB7-Th) for High Performance. *Adv. Mater.* **2013**, *25*, 4766-4771.

(61) Nakayama, K.; Tanabe, K.; Atwater, H. A. Plasmonic Nanoparticle Enhanced Light Absorption in GaAs Solar Cells. *Appl. Phys. Lett.* **2008**, *93*, 121904.

(62) Ko, S.-J.; Choi, H.; Lee, W.; Kim, T.; Lee, B. R.; Jung, J.-W.; Jeong, J.-R.; Song, M. H.; Lee, J. C.; Woo, H. Y.; Kim, J. Y. Highly Efficient Plasmonic Organic Optoelectronic Devices based on a Conducting Polymer Electrode Incorporated with Silver Nanoparticles. *Energy Environ. Sci* **2013**, *6*, 1949-1955.

***** *Chapter 3 is reproduced in part with permission of "Seo, E.; Ko, S.-J.; Min, S. H.; Kim, J. Y.; Kim, B.-S., Chem. Mater.,* ***2015****, 27, 3785-3796" Copyright* ***2015*** *American Chemical Society.*

ULSAN NATIONAL INSTITUTE OF SCIENCE AND TECHNOLOGY

Chapter 4.

Highly Stable Au Nanoparticle Sheathed in Double Hydrophilic Block Copolymer

4.1. Introduction

The tremendous efforts in the design of nanomaterials and the development of distinct characteristic from bulk have been devoted in the last couple of decades, allowing for the controlled syntheses and functionalization of materials in the nanometer scale.[1-2] Among many metal nanoparticles, colloidal gold nanoparticles (Au NPs) have been used in many biological and biomedical application including as biological labels, visualizing reporters, and agents for thermal therapy.[3-5] Albeit with their superior stability in bulk, attempts at preserving and enhancing nanoscale properties of Au NPs in various biological environments such as high pH and ionic strength have received a significant attention for successful translation of their interesting properties into wider potential areas.[6]

Typically, Au NPs can be prepared with a controlled size ranging from a few to several hundreds of nanometer through either adsorption or chemical binding of single molecules such as citric acid, or thiol-functionalized chemical species as surfactants and stabilizers (Scheme 4.1).[7-8] Furthermore, introduction of polymers for surface passivation of as-prepared NPs enhances the colloidal stability by strong inhibition of the non-specific adsorption of biomolecules such as peptide and protein.[9] In particular, polymeric ligand with the characteristic of water-solubilizing (i.e. poly(ethylene glycol)) can not only interrupt undesired interactions with natural materials, but also provide an antifouling effect by surface organization of copolymers on NP.[10-12]

ULSAN NATIONAL INSTITUTE OF SCIENCE AND TECHNOLOGY

In recent years, block copolymers have been studied as highly attractive materials that can improve the stabilization of NPs.[13-15] Among them, double hydrophilic block copolymer (DHBC) facilitates not only the formation and controlled growth of nanostructure, but also high tunability of NPs by chemically different functionalities of each block.[16-19] Biocompatible group such as PEG segment in DHBC can additionally provide an extended biological application. Emrick and co-workers have reported that hydrophilic zwitterionic copolymer passivating on surface of Au nanorods can provide a great stability of nanorods in solution, and enhanced cytocompatibility in live cells.[20] In other example, brush-like PDMAEA-based copolymers can provide a simple approach to form nanostructure because such copolymers can serve as a reducing agent as well as a stabilizer in single step[21] Although the coverage of such polymeric ligand can provide long-term colloidal stability in a broad range of pH, the surface of NP can be still damaged by exposure to high temperature, pH, light, and external chemicals[15] due to weak interactions between polymer and surface and/or a relatively low density of thiol group which is inefficient for complete passivation.

In terms of synthesis of NP, direct utilization of DHBC as a template as well as stabilizer has been recently stood out as an efficient alternative to the conventional surfactant-based method or post-functionalization with macromolecular ligands. Specifically, the DHBCs can induce micellar structures with inorganic reactants through polyionic complexation in water.[22-24] With the aid of the DHBC on the surface of NPs, the intrinsic properties of colloidal NPs under specific environments could be preserved (Scheme 4.1).

In a DHBC system, the extension of these copolymers in wide applications is still challenging because micellization and corresponding mineralization during NP growth processes are highly dependent on various factors; for example, internal parameters such as types of polymers, the molecular weight of polymers, and the ratio of reactants, as well as the external conditions such as pH, temperature, ionic strength, and specific complexation in solution are critical in the synthesis of NP. However, only a few studies on the effect of such various parameters on the stability of NP have been reported.

Herein, we investigate the effect of controlled molecular weight in PEO-*b*-PAA copolymer on the formation and corresponding stability of NPs. Specifically, the DHBC of poly(ethylene oxide)-*block*-poly(acrylic acid) (PEO-*b*-PAA) is synthesized via Cu-

ULSAN NATIONAL INSTITUTE OF
SCIENCE AND TECHNOLOGY

based atom transfer radical polymerization (Cu-ATRP) method with various molecular weights ranging from 9.5 kg/mol to 31.5 kg/mol. This DHBC template can lead to a formation of spherical Au NPs through the complexation of carboxylate groups of PAA block with Au precursor and subsequent reduction, while the PEO shell can enhance the stability of NP in various biological conditions (Scheme 4.3).

ULSAN NATIONAL INSTITUTE OF SCIENCE AND TECHNOLOGY

4.2. Experimental Section

Materials. PEO (M_n: 5000 g·mol^{-1}), *tert*-butyl acrylate (*t*BA), *N,N,N',N'',N''*-pentamethyl diethylenetriamine (PMDETA), 2-bromoisobutyryl bromide, and trifluoroacetic acid (TFA) were purchased from Sigma-Aldrich and used as received. Gold(III) chloride trihydrate ($HAuCl_4 \cdot 3H_2O$), and L-ascorbic acid (AA) from Sigma-Aldrich and sodium hydroxide (NaOH) from Junsei Chemical were used without further purification.

Preparation of PEO-Br macroinitiator. The typical procedure to synthesize PEO-Br macroinitiator can be introduced as follow; first, 5.0 g (0.10 mol) of α-methoxy-ω-hydroxy poly(ethylene oxide) (MeO-PEO-OH, M_n: 5000) is added into 30.0 mL of anhydrous THF. After cooling the flask down to 0 °C using ice-bath, 2-bromoisobutyryl bromide was slowly added into reaction flask for 1.0 h via a syringe pump with constant pressure. Then, the reaction solution gradually became warm up to room temperature and stirred overnight. The solvent was removed by rotary evaporation, and then, the mixture was extracted with dichloromethane (DCM) after dissolved into water, dried over magnesium sulfate. The solution was filtrated and concentrated through rotary evaporation. The crude product was precipitated and in diethyl ether and filtrated three times to obtained pure macroinitiator.

Synthesis of PEO-*b*-P*t*BA. The polymerization was carried out under an inert atmosphere of dry argon in a reaction vial and *tert*-butyl acrylate (*t*BA) monomer was passed through a plug of basic alumina to remove inhibitors before polymerization. Anhydrous toluene was prepared by molecular sieve and argon bubbling. First, PEO-Br macroinitiator and CuBr were added into a 40 mL of reaction vial, and the reaction vial was subjected to vacuum-argon filling cycles three times. *t*BA monomer, PMDETA, and anhydrous toluene were added into via argon purged syringe. The monomer concentration was varied to control the molecular weight of the resulting P*t*BA block. After the mixture became homogeneous, the polymerization was conducted at 80 °C under argon atmosphere. After reaction, the solution was filtered through the basic alumina column to remove the Cu catalyst. The filtrate was evaporated and the crude polymer was dried under vacuum.

ULSAN NATIONAL INSTITUTE OF SCIENCE AND TECHNOLOGY

Synthesis of PEO-*b*-PAA via hydrolysis. PEO-*b*-P*t*BA was first dissolved in DCM in round bottom flask, and then TFA was slowly added into the flask at 0 °C. The solution was stirred at room temperature overnight. After hydrolysis, the solvent was completely removed via rotary evaporation. The crude product was dissolved in THF and dialyzed against deionized water to remove reactant residues. The pure white product, PEO-*b*-PAA was obtained through freeze-drying process.

Synthesis of Au NPs by PEO-*b*-PAA copolymers. Au NPs with a double hydrophilic block copolymer shell (Au@DHBC NPs) were prepared according to the following protocol. First, PEO-*b*-PAA (0.20 mmol carboxylic acid groups) was dissolved under vigorous stirring in 50.0 mL of deionized water, followed by the addition of 0.10 mL of 4.0 M NaOH (0.40 mmol, 2 equiv. to carboxylic acid groups in PAA block). To this solution, $HAuCl_4 \cdot 3H_2O$ (26.2 mg, 0.067 mmol) was added. Subsequently, 2.0 mL of 1.0 M AA (2.0 mmol) was added to the resulting suspension under vigorous stirring. After a few min, the solution underwent a color change to transparent red. After the reaction, the solution was dialyzed against deionized water using a dialysis membrane (MWCO 12,000–14,000, SpectraPore) to remove any residuals. The prepared suspension of Au@DHBC NPs exhibited fairly good colloidal stability, which lasted more than 6 months without any precipitation.

Thermal stability of Au@citrate and Au@PEO-*b*-PAA NPs. Preparation of agarose gel composite. Agarose powder was dispersed in water. Agarose solution in flask was heated using a microwave for 1.0 min until the agarose powder was completely dissolved. After removing from microwave, the agarose solution was gently shaken. The solution was additionally heated for 5.0 min, while Au NPs were added into the flask when the temperature in the agarose solution became 95 or 60 ºC. At 60 ºC, the agarose mixture with Au NPs was transferred into the container and cooled to room temperature.

Stability in various buffers. Au NPs synthesized citrate and $PEO_{5.0k}$-*b*-$PAA_{6.9k}$ copolymer were dialyzed against various buffers, including Tris buffer (10 mM, pH 7.0), carbonate buffer (25 mM, pH 10.5), MES buffer (50 mM, pH 6.1), and phosphate buffer (0.10 M, pH 7 and 8), individually. The UV-vis spectra of these buffer with Au NPs were measured after 24 h to investigate stability

Etching of Au NPs by cyanide ions. Au@citrate and Au@DHBC NP solution (2.0 nM), and KCN solution (24.0 mM) were separately prepared. 1.0 mL of Au NPs was

ULSAN NATIONAL INSTITUTE OF SCIENCE AND TECHNOLOGY

mixed with 1.0 mL of KCN solution in 4.0 mL of vial. Absorbance of the mixture of A and KCN solution was measured in specific interval using UV-vis spectrophotometer. To observe the stability of Au@citrate and Au@DHBC NPs, the absorption intensity at 520 nm of wavelength was selectively plotted.

Characterizations. ^{1}H NMR spectroscopy was recorded on a Varian 600 MHZ instrument, and reported in δ units, parts per million (ppm). All polymers were measured relative to the signals for residual deuterated chloroform (7.26 ppm) or deuterated water (4.79 ppm). Size-exclusion chromatography (SEC) traces and polydispersity index (PDI) of polymers were measured by Waters Alliance HPLC System equipped with a Waters 2414 refractive index detector using a mixture of chloroform and trimethylamine or dimethylformamide (DMF) with LiBr. The poly(methyl matacrylate) (PMMA) homopolymers were used as a standard materials for calibration. As-synthesized copolymers are denoted PEO_{114}-*b*-PAA_m, where 114 is the number based on the information from Sigma Aldrich, and *m* is the value of degree of PAA (DP) block calculated from the molecular weight analyzed by ^{1}H NMR. The morphology, size, and size distribution of the prepared NPs were investigated using transmission electron microscopy (TEM), (JEOL, JEM-2100, accelerating voltage of 200 kV, Gatan CCD camera). UV-Vis spectra were recorded using a UV-Vis spectrophotometer (Shimadzu UV-1800) and size distribution analyses were performed using dynamic light scattering (DLS, BI-APD, Brookhaven Instruments, New York, USA). Hydrodynamic diameters (D_h) of Au@DHBC NPs in aqueous solution were measured by dynamic light scattering (DLS).

ULSAN NATIONAL INSTITUTE OF SCIENCE AND TECHNOLOGY

4.3. Results and Discussion

Synthesis and characterization of PEO-*b*-PAA copolymer. To establish the effect of the PAA block on the growth of NP and corresponding colloidal stability, we prepared a series of PEO-*b*-PAA copolymers through Cu-ATRP method. The synthetic processes are schematically described in Figure 4.1a. Briefly, the PEO macroinitiator is prepared through the esterification of α-methoxy-ω-hydroxy-poly(ethylene oxide) (MeO-PEO-OH, M_n: 5000) with 2-bromoisobutyryl bromide. Because alkyl bromide is very active moiety in ATRP method, bromide-functionalized PEO macroinitiator is effective to polymerize *tert*-butyl acrylate monomer as a second block. PEO macroinitiator with a bromide chain end was confirmed by ^{1}H NMR (top line in Figure 4.1b). PEO-*b*-P*t*BA copolymer was prepared via ATRP of *tert* -butyl acrylate (*t*BA) initiated by PEO macroinitiator in the presence of CuBr as a catalyst and PMDETA as a ligand at 80 °C in anhydrous toluene under argon atmosphere.[25] (ref. Matyjaszewski, Macromolecules 2000, 33, 4039) In ^{1}H NMR spectrum of PEO-*b*-P*t*BA (middle line in Figure 4.1b), the conversion of *t*BA monomer and the degree of polymerization of poly *tert*-butyl acrylate (P*t*BA) were confirmed by calculating signals of 1.43 ppm (*tert*-butyl group in P*t*BA) and 3.36 ppm (methyl group in PEO), respectively. Finally, the hydrolysis of *tert*-butyl ester moieties in PEO-*b*-P*t*BA copolymer was conducted with trifluoroacetic acid (TFA) in DCM. The completely disappearance of the peak *g* assigned at 1.43 ppm suggested the removal of *tert*-butyl group, leading to the formation of desired DHBC of PEO-*b*-PAA (bottom line in Figure 4.1b).

With the same PEO macroinitiator, the molecular weight of P*t*BA block in copolymers was controlled by varying the molar concentration of *t*BA monomer in reaction. Relative molecular weight and distribution of copolymers was compared by SEC measurement (Figure 4.2). The SEC traces of copolymers move toward higher molecular weight, which is consistent with the increase in the amount of the incorporated PAA block. Monomer conversion over ca. 85% and narrow polydispersity (M_w/M_n < 1.16) of molecular weight distribution of copolymer all indicate the controlled polymerization of desired polymers (Table 4.1 and Figure 4.3).

Synthesis of Au NPs using PEO-*b*-PAA copolymers. The DHBCs have been previously employed in the controlled growth of inorganic minerals, such as $CaCO_3$,

ULSAN NATIONAL INSTITUTE OF SCIENCE AND TECHNOLOGY

$BaSO_4$, and $Ca_3(PO_4)_2$, with unusual structural complexity[19] or in the hybrid polyion complexes with metal ions (e.g. Cu^{2+}, Zn^{2+}, Ca^{2+}, Al^{3+}, La^{3+}, and Ga^{3+}). In many cases, hybrid polyion complexes use the electrostatic interaction, resulting from the addition of oppositely charged polyvalent metal ions. On the other hand, metal anions (i.e. $AuCl_4^-$) can bind with negative-charged polyions via a coordinative bonding in this study.[26] Therefore, we have attempted to quantitatively investigate the formation of micelle and NP as a function of the molar ratio of metal ion and copolymer.

In PEO-*b*-PAA system, because a carboxylate group mainly contributes to the NP growth, we have first employed the acetate as a model molecule to investigate their interaction with metal ions. The interaction between sodium acetate and metal precursor was evaluated by mixing them in methanol-d_4, and analyzed by ^{1}H NMR. The proton *a* assignable to the methyl shifted to downfield, supporting that acetate ion efficiently interacted with Au ions (Figure 4.4). The stoichiometry of the interaction was also found to be *ca*. 2:1 (one metal ion per two acetate molecules), as determined by Job's method based on the chemical shift change of the acetate proton (from peak *a* to peak *a*' in Figure 4.4b) and the molar fraction of acetate units (χ): [NaOAc]/[$HAuCl_4$] = 1/0-0/1, [NaOAc] + [$HAuCl_4$] = 10.0 mM (Figure SXc): the plot showed a maximum at $\chi = 0.667$.

As it was difficult to find a specific peak shifting through their interaction of metal ions with PEO-*b*-PAA system, we employed DLS and TEM analysis. The micellar structures and corresponding NPs depending on the molar ratio (*R*) of acrylic acid (AA) in copolymer to metal ions were characterized by DLS and TEM analysis, respectively. At a low concentration of copolymer, micelles become larger by the increase in the amount of copolymer, which then saturated after a certain concentration. It suggests that unstable micellar structure becomes more stable as a function of the concentration of copolymer (Figure 4.5 and Table 4.2). After the formation of NP, in the range of high concentration of copolymer ($R \geq 3$), spherical Au NPs were observed, and these NPs are individually present in solution, while the heterogeneous nanostructure are formed at low value ($R \leq 2$) (Figure 4.5).

Although it was shown that the ratio between the acetate to metal ions is 2 from Job plot, we found that a higher amount of copolymers is required for the synthesis of Au@DHBC NPs. In case of copolymer, steric hindrance due to long chain length and molecular repulsion in solution can induce low consumption of active species in polymer,

ULSAN NATIONAL INSTITUTE OF SCIENCE AND TECHNOLOGY

leading to low accessibility of polymer to metal ions. On the basis of this result from NP formation, it is found that even though the size of micelles does not change from the R value of 1.5, this micellar structure is not as stable at a low concentration of copolymer. On the other hand, very stable micellar structure can be formed in the range of *R* from 3.0, leading to the stable Au NP templated by PEO-*b*-PAA copolymer. Therefore, the R value of 3 was employed for further synthesis of Au NPs using a variety of copolymers to form stable Au NPs.

Five different copolymers were employed to investigate the effect of molecular weight on the formation of NPs. In the presence of PEO-*b*-PAA copolymer in solution, the induced micellar formation by the interaction with PAA block and metal ions leads to the spherical Au NP after the reduction (Figure 4.6a). All Au NP remains stable in solution with assistance from PEO block sterically protecting the resulting NPs. For example, Au NPs prepared by PEO_{5k}-*b*-$PAA_{6.9k}$ copolymer show an average size of 16.7 ± 3.3 nm by TEM analysis and 26.2 nm by DLS (Figure 4.6c and Table 4.3). The result of DLS measurement yields a slightly larger size than that of TEM, which supports the presence of thin polymeric layer surrounding the NP.

Interestingly, the synthesized Au NPs have similar diameter ranging between 16.3 and 19.2 nm, which is not significantly different although the molecular weights of the copolymers are controlled in a wide range from 9.6 kg/mol to 31.7 kg/mol. In other words, the difference of molecular weight is about 20 kg/mol, but the size difference is only 3 nm. This result indicates the size of NP does not depend on the chain length of copolymer (type 1 in Scheme 4.2). On the other hand, it is believed that size of resulting NP can be determined by constant ratio of metal ions to active species participating in the NP growth (type 2 in Scheme 4.2). Based on this evidence, it is inferred that the density of second block, PEO in copolymer could be tunable depending on the length of PAA block in NP. To evaluate the effect of copolymers in NPs, we first observed the stability difference of between NPs by citrate and PEO_{5k}-b-$PAA_{6.7k}$ copolymer against biological conditions.

The effect of copolymers on the stability of NPs. As a conventional manner, surfactant-based approach for the synthesis of NP, e.g. citrate, requires additional modification using macromolecule, our DHBC-based synthesis is more efficient because it requires no further modification in terms of synthesizing a stable NP. Moreover, PEO block is covalently bound to PAA, this PEO is not detached from the surface, resulting in

ULSAN NATIONAL INSTITUTE OF SCIENCE AND TECHNOLOGY

durable NPs. To investigate the stability of NPs by PEO block, citrate-based Au NPs (Au@citrate NPs) with a similar diameter (17.0 nm) were synthesized as a control experiment.

To confirm the thermal stability of the NPs in an aqueous medium, we first observed the change of Au NP at 95 ^{o}C (Figure 4.7a). The absorbance of Au@P2 NPs varies little over 24 h, and no change in the size and shape of the NPs is observed. It indicates that the Au@P2 NP does not flocculate at high temperature. The slight increase in absorbance intensity of Au@P2 NP can be attributed to evaporation of water over time. In case of Au@citrate, however, aggregation of NP occurs immediately at 95 ^{o}C, resulting in precipitation in solution.

With this superior thermal and colloidal stability of Au@DHBC NPs, we produced a hydrogel containing Au@DHBC NPs as well (Figure 4.7b). Au@P2 NPs could be readily suspended in a hot and aqueous solution of agarose polysaccharide and then cooled to form a hydrogel complex. The image in Figure 4.7 show clearly that Au@P2 NP is well-dispersed in a gel matrix, while the Au@citrate is very unstable in the gel because of low stability at 95 ^{o}C.

Stability in various biological buffers. It is also confirmed that PEO-*b*-PAA copolymer around Au NPs can preserve the stability of resulting NPs against a variety of buffer solutions including sodium and potassium phosphate, Tris and MES, and carbonate. On the contrary, the stability of Au@citrate NPs is significantly diminished even at a low concentration of salts in buffers, leading to the agglomerate through the interparticle coupling or ionization of NPs. This result also leads to the decrease in their absorption with a concomitant color change from red to purple or transparent (Figure 4.8a).

Even though the buffers are introduced into Au@PEO-*b*-PAA NPs, the solution color and absorption intensity at 520 nm of NPs still does not change, shown in Figure 4.8a. Upon the addition of HCl and NaOH into each solution (Figure 4.8b), the absorption intensity of Au@DHBC NPs is almost identical, while Au@citrate NPs exhibited the decrease in the absorbance at 520 nm. Such contrast highlights the importance of outer PEG shell in colloidal stability.

In accordance with results, it is noteworthy that the method using DHBC enables the synthesis of very stable NPs without additional process such as conventional polymer-based surface modification. Furthermore, each controlled block constituting DHBC is

ULSAN NATIONAL INSTITUTE OF SCIENCE AND TECHNOLOGY

expected to contribute not only to the physical properties of the NPs produced, but also to the changes in chemical properties, such as particle stability.

Effect of molecular weight of copolymers on nanoparticle stability against thermal treatment and etching. As it was experimentally found that a number of PEO chains surrounding NP surface can be controlled by the molecular weight of PAA block, we have investigated its effect on the stability of Au@DHBC NPs. All Au@DHBC NPs exhibited an outstanding thermal stability at 95 ^{o}C over several hours, whereas Au@citrate NP is easily degradable under the identical thermal treatment. However, the difference between copolymers with respect to its thermal stability is hardly observed (Figure 4.9a). It is known that Au@citrate NPs slowly degrade in solution with potassium cyanide (KCN), completely degrade within the reaction time from a few to several tens of minutes. Such degradation of NPs could be prevented via the modification of surface by PEG-based polymers, leading to enhanced colloidal stability. Cyanide ions can attack the Au metal to from the complexation of Au and cyanide in the presence of oxygen on the basis of Elsner's equation. In the study of the NPs against cyanide digestion, it was shown that the higher packing density of the ligand exhibit better barrier to prevent the cyanide complex into the Au atoms. Similarly, in our system, because of higher number of PEG chains in Au@P1 NPs, the digestion rate of Au NPs attributed to cyanide ions becomes fairly slow, while the low PEG density in Au@P5 NPs facilitates their Au-CN complexation, leading to fast digestion.

Considering all of these results including NP synthesis and etching test, we propose a mechanism for the effect of chain length of copolymers on the formation of NPs and corresponding colloidal stability as described in Scheme 4.4. Carboxylate group in PAA block acts as an active site to form the Au core, and PEO block does not directly participate in growth of NP. It is supposed that because the size of all NPs is similar, the carboxylate group participating in the formation of NPs might be also similar, leading to different molar concentration of PAA in each copolymer. This result means that number of PEO chain surrounding the surface of each NP depends on the mole of PAA because molecular weight of PEO is same as 5 kg/mol in all copolymers we prepared here. Briefly described, the density of PEO in Au@LP NP is higher than in Au@HP NP. HP and LP indicate high and low molecular weight of copolymer, respectively. Additionally, this difference results in relatively "condense" packed ligand layer on the Au@LP NP and

ULSAN NATIONAL INSTITUTE OF
SCIENCE AND TECHNOLOGY

thus more shielding of the NP surface, which can protect NP against external attack, while the Au@HP NP has a “loosely” packed ligand. Because citrate-based NPs is low molecular weight and has a rather loose ligand shell, such NP could be easily destroyed or accumulated under various conditions.

ULSAN NATIONAL INSTITUTE OF SCIENCE AND TECHNOLOGY

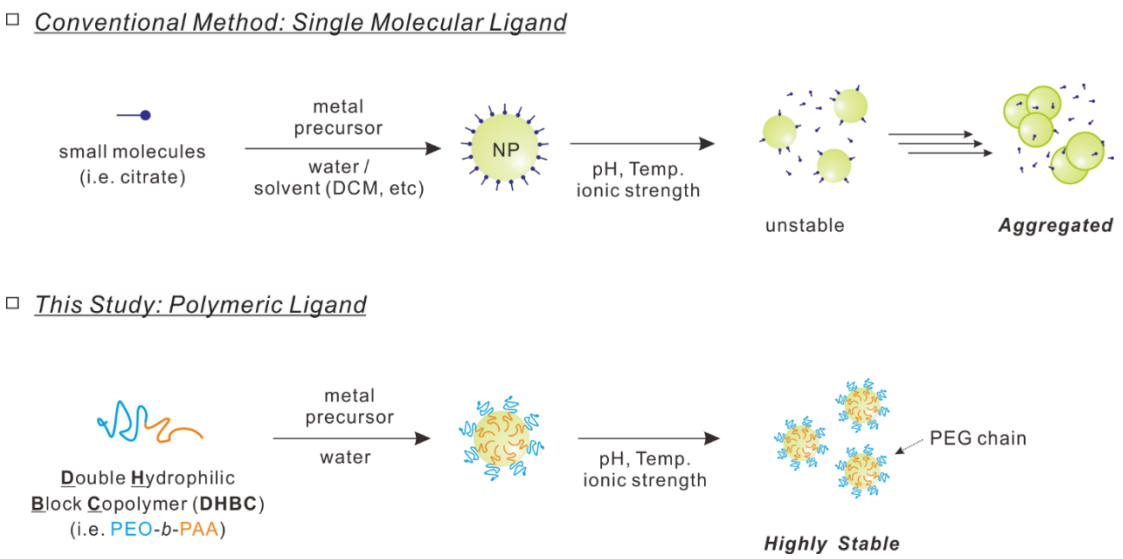

Scheme 4.5. Synthetic approaches of Au nanoparticle and corresponding stability in various conditions.

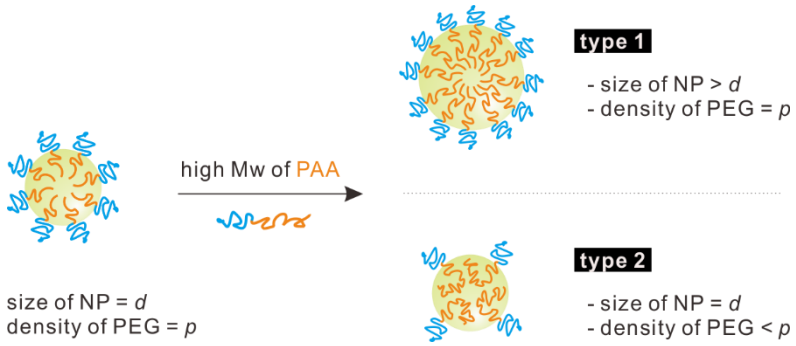

Scheme 4.6. Proposed formation of nanoparticles synthesized by different molecular weight of PAA block

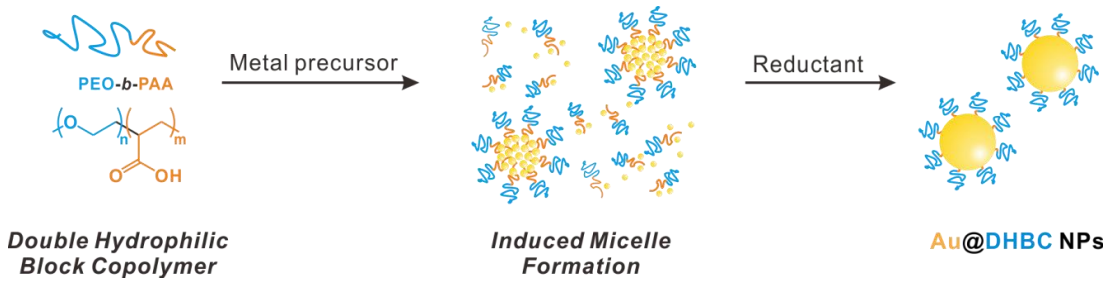

Scheme 4.7. Synthesis of Au@DHBC NPs through micelle complexation between double hydrophilic block copolymer (DHBC), PEO-*b*-PAA, and metal precursor, hydrated $HAuCl_4$.

ULSAN NATIONAL INSTITUTE OF SCIENCE AND TECHNOLOGY

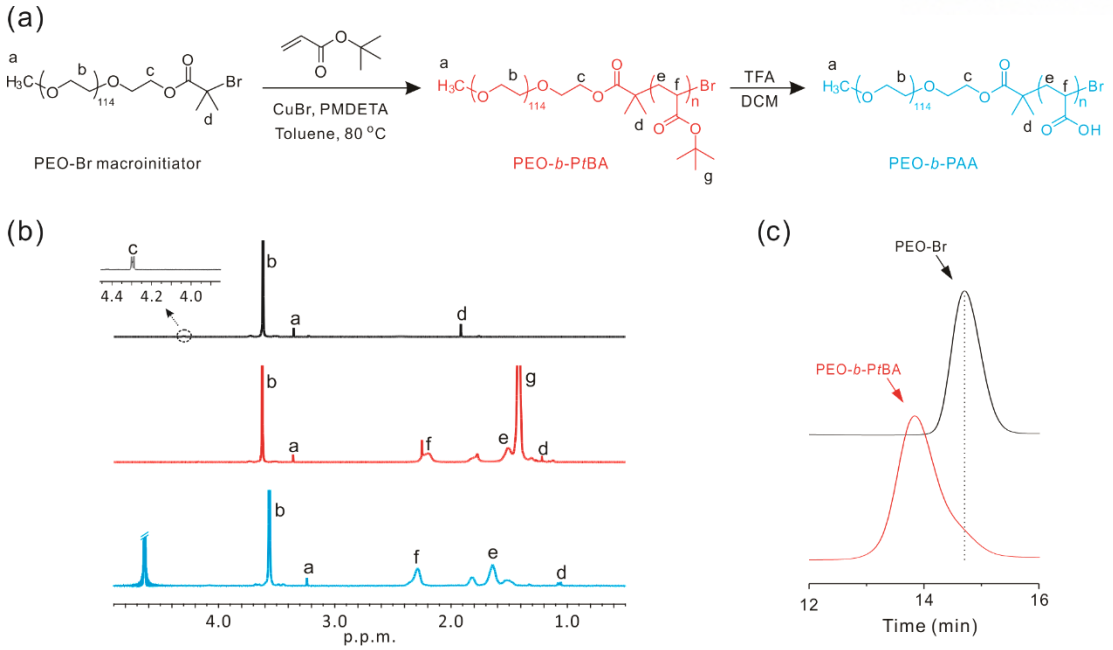

Figure 4.10. (a) Synthetic Scheme of the representative double hydrophilic block copolymer (DHBC), $PEO_{5.0k}$-*b*-$PAA_{6.9k}$. (b) ^1H NMR of spectra of PEO-Br macroinitiator (black), PEO-*b*-P*t*BA copolymer (red), and PEO-*b*-PAA (blue). (c) GPC traces of PEO-Br macroinitiator (black) and PEO-*b*-P*t*BA (red) in $CHCl_3$.

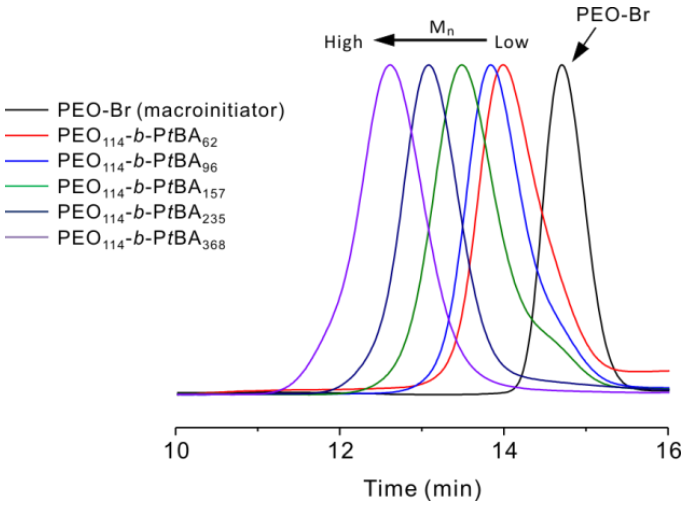

Figure 4.11. SEC traces of PEO macroinitiator and PEO-*b*-P*t*BA copolymers in Chloroform GPC analysis. PMMA was used as a standard to obtain the molecular weight and molecular weight distribution shown in Table 1.

ULSAN NATIONAL INSTITUTE OF SCIENCE AND TECHNOLOGY

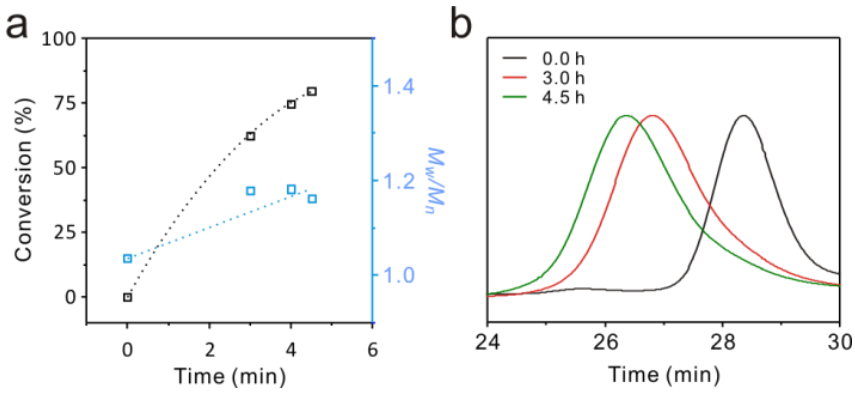

Figure 4.12. (a) Monomer conversion and polydispersity index and (b) SEC traces of PEO_{5k}-*b*-P*t*$BA_{6.9k}$ copolymer (P1) as a function of reaction time.

Table 4.4. Characterization of PEO-b-PAA copolymers

Entry	Composition	N_{PEO}	N_{PAA}[a]	$M_{n,\ NMR}$ PEO-*b*-P*t*BA	$M_{n,\ SEC}$[b] PEO-*b*-P*t*BA	$M_{n,\ NMR}$ PEO-*b*-PAA	M_w/M_n[b]
P1	PEO_{5k}-*b*-$PAA_{4.5k}$	114	62	13 100	16 300	9 600	1.09
P2	PEO_{5k}-*b*-$PAA_{6.9k}$	114	96	17 400	18 000	12 100	1.11
P3	PEO_{5k}-*b*-$PAA_{11.3k}$	114	157	25 300	23 000	16 500	1.16
P4	PEO_{5k}-*b*-$PAA_{16.9k}$	114	235	35 300	34 800	22 100	1.12
P5	PEO_{5k}-*b*-$PAA_{26.5k}$	114	368	52 300	48 100	31 700	1.16

[a]Degree of polymerization (DP) of PAA was calculated by ^{1}H NMR. [b]Number-averaged molecular weight (M_n) and molecular weight distribution (M_w/M_n) were determined by size-exclusion chromatography (SEC) in chloroform with TEA (chloroform:TEA (v/v) = 98:2) and PMMA was used as a standard.

ULSAN NATIONAL INSTITUTE OF SCIENCE AND TECHNOLOGY

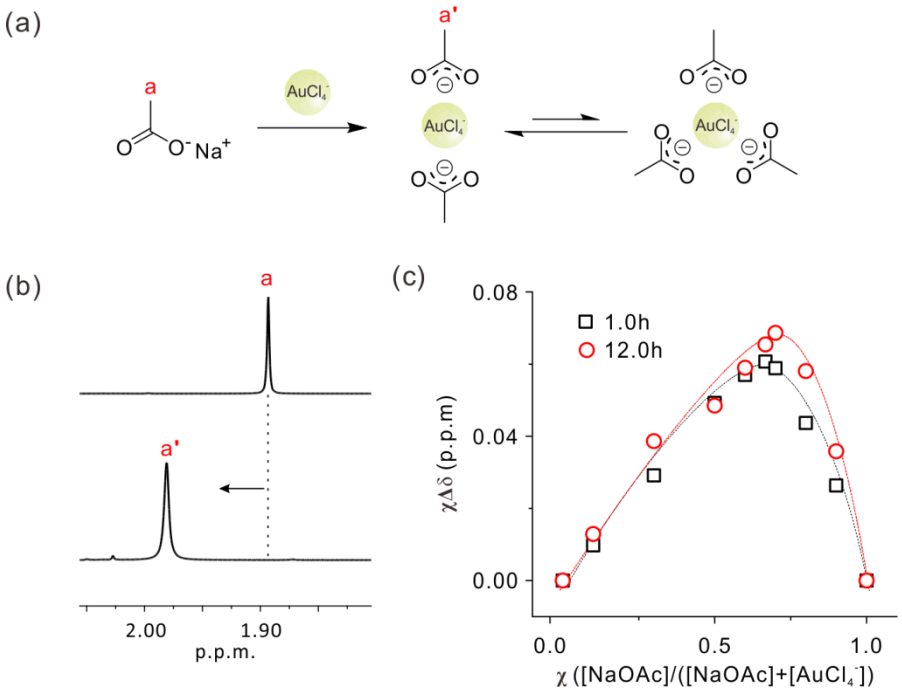

Figure 4.13. (a) Scheme of reaction between sodium acetate and gold precursor. (b) ^{1}H NMR spectra of pure sodium acetate (upper) and (b) complex with Au precursor in methanol-d_4 at room temperature. The proton signal of the sodium acetate shifted to downfield by the complexation with gold precursor. (c) Job plots were investigated at reaction time of 1.0 h and 12.0 h after complexation with sodium acetate and Au precursor, showing efficient interaction when the ratio of sodium acetate to Au precursor was 0.667:0.333.

ULSAN NATIONAL INSTITUTE OF SCIENCE AND TECHNOLOGY

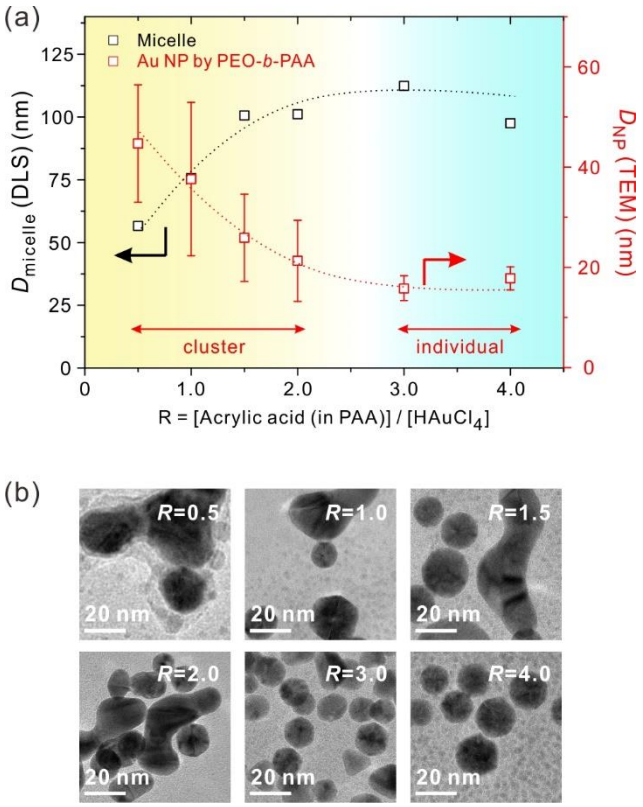

Figure 4.14. Average diameter of (a) micelle of PEO_{5k}-*b*-$PAA_{6.9k}$ and Au precursor (before reduction) and (b) Au NP by PEO_{5k}-*b*-$PAA_{6.9k}$ (after reduction by ascorbic acid), depending on the molar ratio, *R* of acrylic acid unit in PEO_{5k}-*b*-$PAA_{6.9k}$ to Au precursor

Table 4.5. Characterization of Au NPs by PEO_{5k}-*b*-$PAA_{6.9k}$ copolymer

R[a]	0.5	10	1.5	2.0	3.0	4.0
Micelle (nm)	56.6	75.7	100.6	101.1	112.4	97.5
NP (mn)	44.7 ± 11.7	37.6 ± 15.3	25.9 ± 8.7	21.3 ± 8.1	16.7 ± 3.3	17.8 ± 2.3

[a]The ratio of acrylic acid in copolymer to Au precursor is denoted as *R*.

ULSAN NATIONAL INSTITUTE OF SCIENCE AND TECHNOLOGY

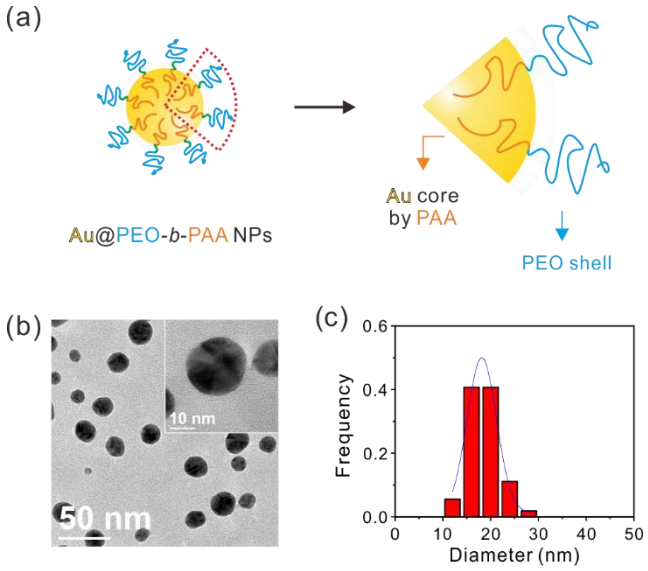

Figure 4.15. Schematic description of Au NPs sheathed in double hydrophilic block copolymer, PEO_{5k}-*b*-$PAA_{6.9k}$. (b) TEM image and (c) Size distribution of Au@PEO-*b*-PAA NPs. Inset in Figure b is a high-resolution TEM image of representative Au@PEO-*b*-PAA NPs.

Table 4.6. Characterization of Au NPs prepared by citrate and PEO-*b*-PAA copolymers

Entry	Molecules used in NP synthesis	d_{NP} (nm) (TEM)	R_d (nm) (DLS)
Au@citrate	Citric acid	17.1 ± 1.2	-
Au@P1	PEO_{5k}-*b*-$PAA_{4.5k}$	17.3 ± 3.1	31.6
Au@P2	PEO_{5k}-*b*-$PAA_{6.9k}$	16.7 ± 3.3	26.2
Au@P3	PEO_{5k}-*b*-$PAA_{11.3k}$	19.2 ± 3.8	27.6
Au@P4	PEO_{5k}-*b*-$PAA_{16.9k}$	15.8 ± 3.0	29.4
Au@P5	PEO_{5k}-*b*-$PAA_{26.5k}$	16.3 ± 3.5	31.6

ULSAN NATIONAL INSTITUTE OF SCIENCE AND TECHNOLOGY

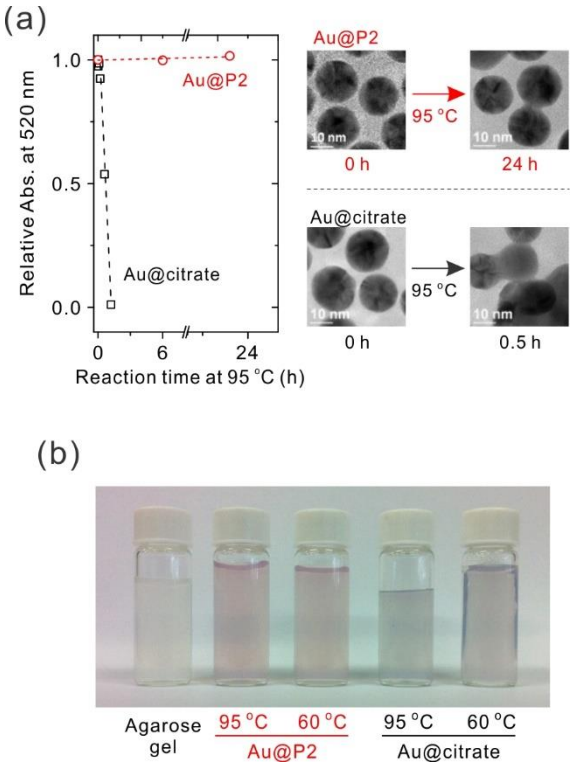

Figure 4.16. Thermal stability of (a) Au@P2 and Au@citrate NPs depending on the reaction time at 95 °C in oven. TEM images of each Au NP were measured before and after thermal annealing. (b) Photograph of agarose gel without and with Au@P2 or Au@citrate NPs. The particle concentration of Au solution in gel solution was fixed at 0.10 nM.

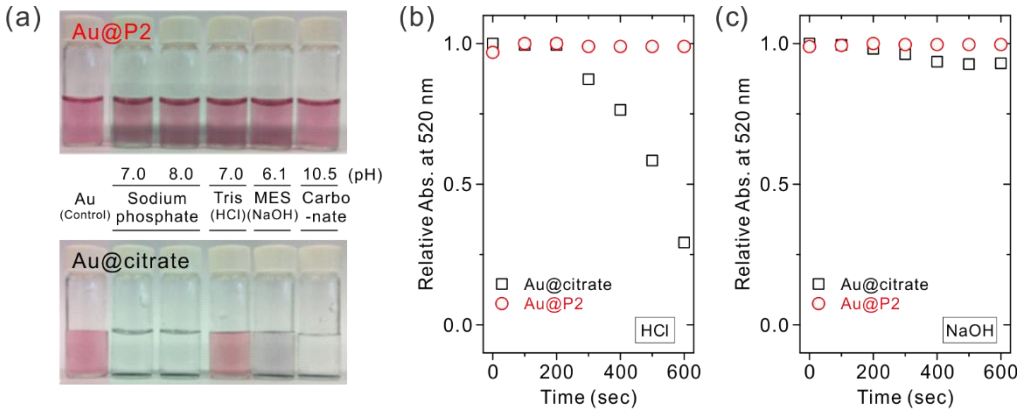

Figure 4.17. Photographs (a) Au@P2 and Au@citrate NP in various buffer solutions with different pH. (b, c) Relative stability of Au@P2 NPs in acid and basic conditions.

ULSAN NATIONAL INSTITUTE OF SCIENCE AND TECHNOLOGY

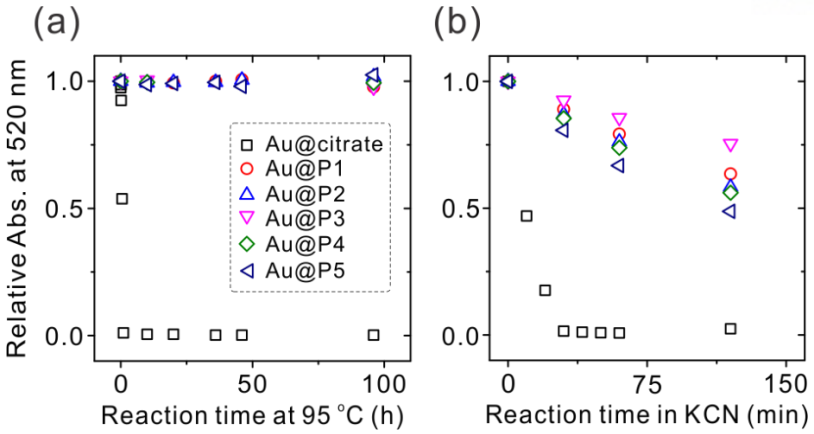

Figure 4. 18. Thermal stability at 95 ºC and (b) cyanide digestion in KCN solution (12 mM) of Au@citrate and Au NPs by various PEO-*b*-PAA copolymers..

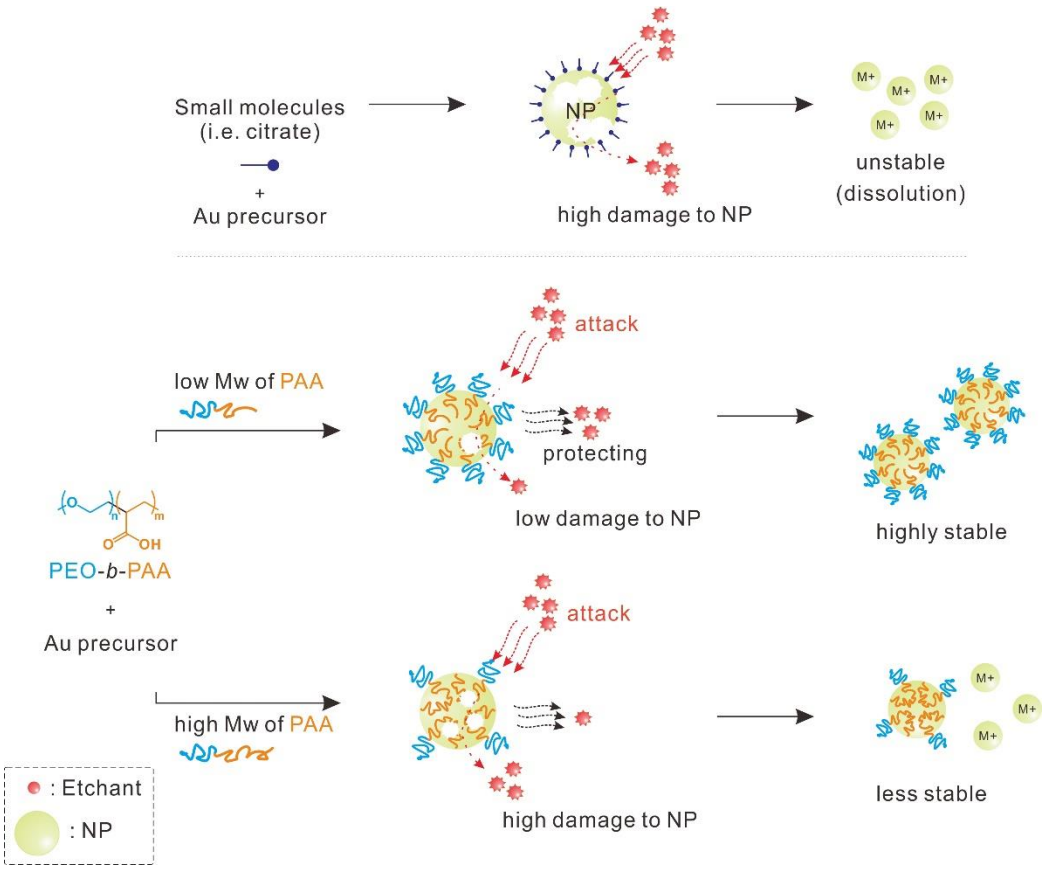

Scheme 4.8. Proposed description of NP and its property, depending on both the different molecular weight of PAA block and corresponding density of PEO block on the surface of NP.

ULSAN NATIONAL INSTITUTE OF SCIENCE AND TECHNOLOGY

4.4. Conclusion

In this report, we have investigated the structural role of the double hydrophilic block copolymer (DHBC) in the synthesis of nanoparticle (NPs). In PEO-*b*-PAA copolymer-based synthesis, it has been found that stable gold nanoparticle (Au NP) can be formed because of the presence of PEO shell on the surface after the growth of NP by PAA block. The synthesis of such DHBC-based NPs can be sufficiently substituted for existing synthetic methods that require surface modification. In general, PEO-*b*-PAA system has two functional blocks; first block, PAA is capable of binding metal ions and second block, PEO imparts stability. Although the molecular weight of PAA in the copolymers is not a factor that determines the size of NPs, it shows the difference in the density of PEO present on the surface of NP depending on the molecular weight of PAA. This difference show that it is possible to synthesize NP with stability that can be controlled according to the molecular weight of the copolymers. The use of DHBC with both hydrophilic and biocompatible components for the synthesis of NPs is expected to be applicable to biological applications.

4.5. References

(1) Crooks, R. M.; Zhao, M.; Sun, L.; Chechik, V.; Yeung, L. K., Dendrimer-Encapsulated Metal Nanoparticles: Synthesis, Characterization, and Applications to Catalysis. *Acc. Chem. Res.* **2001**, *34*, 181-190.

(2) Pérez-Juste, J.; Pastoriza-Santos, I.; Liz-Marzán, L. M.; Mulvaney, P., Gold Nanorods: Synthesis, Characterization and Applications. *Coord. Chem. Rev.* **2005**, *249*, 1870-1901.

(3) Lin, C.-A. J.; Yang, T.-Y.; Lee, C.-H.; Huang, S. H.; Sperling, R. A.; Zanella, M.; Li, J. K.; Shen, J.-L.; Wang, H.-H.; Yeh, H.-I., Synthesis, Characterization, and Bioconjugation of Fluorescent Gold Nanoclusters toward Biological Labeling Applications. *ACS nano* **2009**, *3*, 395-401.

(4) Daniel, M.-C.; Astruc, D., Gold Nanoparticles: Assembly, Supramolecular Chemistry, Quantum-Size-Related Properties, and Applications toward Biology, Catalysis, and Nanotechnology. *Chem. Rev.* **2004**, *104*, 293-346.

(5) Murphy, C. J.; Gole, A. M.; Stone, J. W.; Sisco, P. N.; Alkilany, A. M.; Goldsmith, E. C.; Baxter, S. C., Gold Nanoparticles in Biology: Beyond Toxicity to Cellular Imaging. *Acc. Chem. Res.* **2008**, *41*, 1721-1730.

(6) Dreaden, E. C.; Alkilany, A. M.; Huang, X.; Murphy, C. J.; El-Sayed, M. A., The Golden Age: Gold Nanoparticles for Biomedicine. *Chem. Soc. Rev.* **2012**, *41*, 2740-2779.

(7) Sau, T. K.; Murphy, C. J., Room Temperature, High-Yield Synthesis of Multiple Shapes of Gold Nanoparticles in Aqueous Solution. *J. Am. Chem. Soc.* **2004**, *126*, 8648-8649.

(8) Jana, N. R.; Gearheart, L.; Murphy, C. J., Seeding Growth for Size Control of 5-40 Nm Diameter Gold Nanoparticles. *Langmuir* **2001**, *17*, 6782-6786.

(9) Kobayashi, K.; Wei, J.; Iida, R.; Ijiro, K.; Niikura, K., Surface Engineering of Nanoparticles for Therapeutic Applications. *Polym. J.* **2014**, *46*, 460-468.

(10) Roberts, M.; Bentley, M.; Harris, J., Chemistry for Peptide and Protein Pegylation. *Adv. Drug Deliv. Rev.* **2012**, *64*, 116-127.

(11) Banerjee, I.; Pangule, R. C.; Kane, R. S., Antifouling Coatings: Recent Developments in the Design of Surfaces That Prevent Fouling by Proteins, Bacteria, and Marine Organisms. *Adv. Mater.* **2011**, *23*, 690-718.

(12) Stewart, M. H.; Susumu, K.; Mei, B. C.; Medintz, I. L.; Delehanty, J. B.; Blanco-

ULSAN NATIONAL INSTITUTE OF SCIENCE AND TECHNOLOGY

Canosa, J. B.; Dawson, P. E.; Mattoussi, H., Multidentate Poly(ethylene glycol) Ligands Provide Colloidal Stability to Semiconductor and Metallic Nanocrystals in Extreme Conditions. *J. Am. Chem. Soc.* **2010**, *132*, 9804-9813.

(13) Kang, Y.; Taton, T. A., Controlling Shell Thickness in Core-Shell Gold Nanoparticles Via Surface-Templated Adsorption of Block Copolymer Surfactants. *Macromolecules* **2005**, *38*, 6115-6121.

(14) Chen, Y.; Cho, J.; Young, A.; Taton, T. A., Enhanced Stability and Bioconjugation of Photo-Cross-Linked Polystyrene-Shell, Au-Core Nanoparticles. *Langmuir* **2007**, *23*, 7491-7497.

(15) Que, Y.; Feng, C.; Zhang, S.; Huang, X., Stability and Catalytic Activity of Peg-B-Ps-Capped Gold Nanoparticles: A Matter of Ps Chain Length. *J. Phys. Chem. C* **2015**, *119*, 1960-1970.

(16) Pang, X.; Zhao, L.; Han, W.; Xin, X.; Lin, Z., A General and Robust Strategy for the Synthesis of Nearly Monodisperse Colloidal Nanocrystals. *Nat. nanotechnol.* **2013**, *8*, 426-431.

(17) Bastakoti, B. P.; Guragain, S.; Yusa, S.-i.; Nakashima, K., Novel Synthesis Route for Ag@SiO_2 Core–Shell Nanoparticles Via Micelle Template of Double Hydrophilic Block Copolymer. *RSC Adv.* **2012**, *2*, 5938-5940.

(18) Nakashima, K.; Bahadur, P., Aggregation of Water-Soluble Block Copolymers in Aqueous Solutions: Recent Trends. *Adv. Colloid Interface Sci.* **2006**, *123*, 75-96.

(19) Cölfen, H., Double-Hydrophilic Block Copolymers: Synthesis and Application as Novel Surfactants and Crystal Growth Modifiers. *Macromol. Rapid Commun.* **2001**, *22*, 219-252.

(20) Chen, X.; Lawrence, J.; Parelkar, S.; Emrick, T., Novel Zwitterionic Copolymers with Dihydrolipoic Acid: Synthesis and Preparation of Nonfouling Nanorods. *Macromolecules* **2012**, *46*, 119-127.

(21) Feng, C.; Shen, Z.; Li, Y.; Gu, L.; Zhang, Y.; Lu, G.; Huang, X., PNIPAM-*b*-(PEA-*g*-PDMAEA) Double-Hydrophilic Graft Copolymer: Synthesis and Its Application for Preparation of Gold Nanoparticles in Aqueous Media. *J. Polym. Sci., Part A: Polym. Chem.* **2009**, *47*, 1811-1824.

(22) Boudier, A.; Aubert-Pouëssel, A.; Louis-Plence, P.; Gérardin, C.; Jorgensen, C.; Devoisselle, J.-M.; Bégu, S., The Control of Dendritic Cell Maturation by *p*H-Sensitive

ULSAN NATIONAL INSTITUTE OF SCIENCE AND TECHNOLOGY

Polyion Complex Micelles. *Biomaterials* **2009**, *30*, 233-241.

(23) Sanson, N.; Bouyer, F.; Gérardin, C.; In, M., Nanoassemblies Formed from Hydrophilic Block Copolymers and Multivalent Ions. *Phys. Chem. Chem. Phys.* **2004**, *6*, 1463-1466.

(24) Sanson, N.; Bouyer, F. d. r.; Destarac, M.; In, M.; Gérardin, C., Hybrid Polyion Complex Micelles Formed from Double Hydrophilic Block Copolymers and Multivalent Metal Ions: Size Control and Nanostructure. *Langmuir* **2012**, *28*, r3773-3782.

(25) Davis, K. A.; Matyjaszewski, K., Atom Transfer Radical Polymerization of *tert*-Butyl Acrylate and Preparation of Block Copolymers. *Macromolecules* **2000**, *33*, 4039-4047.

(26) Seo, E.; Kim, J.; Hong, Y.; Kim, Y. S.; Lee, D.; Kim, B.-S., Double Hydrophilic Block Copolymer Templated Au Nanoparticles with Enhanced Catalytic Activity toward Nitroarene Reduction. *J. Phys. Chem. C* **2013**, *117*, 11686-11693.

ULSAN NATIONAL INSTITUTE OF SCIENCE AND TECHNOLOGY

Chapter 5.

Versatile Double Hydrophilic Block copolymer: Dual Role as Synthetic Nanoreactor and Ionic and Electronic Conduction Layer for Ruthenium Oxide Nanoparticle Supercapacitor

5.1. Introduction

Supercapacitors are gathering considerable attention as attractive electrochemical energy storage and conversion devices with the growing demand for future portable devices and electric vehicles due to their complementary performance to secondary batteries and fuel cells.[1-6] Comparing with other power sources like secondary batteries, supercapacitors exhibit a number of distinctive features such as higher power density (10 kW/kg), faster charge/discharge capability (within seconds), long cycle life (>10^5), wide thermal operating range, and low maintenance cost.[7]

Depending on their charge storage mechanism and the active materials used, supercapacitors are generally classified into two major types; (1) electric double-layer capacitors (EDLCs) which store the electrical charges at the interface of porous electrode (typically, carbon-based materials) and electrolyte based on the non-Faradaic reaction and (2) pseudocapacitors which utilize the Faradaic reaction of redox-active materials such as conducting polymers and metal oxides. Among various electrode materials, ruthenium

***** Chapter 5 is reproduced in part with permission of *"Seo, E.; Lee, T.; Lee, K. T.; Song, H. K.; Kim, B. S., J. Mater. Chem.2012, 22, 11598−11604".* Copyright 2012, Royal Society of Chemistry.

ULSAN NATIONAL INSTITUTE OF SCIENCE AND TECHNOLOGY

oxide (RuO_2) based supercapacitors are clearly noteworthy, displaying superior specific capacitance, reversible charge-discharge feature with a good electrical conductivity, despite its high cost. [8-12]

It has been suggested that the electrical and electrochemical properties of RuO_2-based materials are highly dependent on their degree of crystallinity, hydration, and surface area. For instance, amorphous and hydrous ruthenium oxide ($RuO_2 \cdot xH_2O$) exhibited a superior specific capacitance of 600 – 900 F/g by virtue of highly reversible redox transitions based on the high proton conductivity near the interface with electrolyte, while that of crystalline and anhydrous RuO_2 is only about 200 F/g.[13-16] Nevertheless, the relatively low electronic conductivity of hydrous $RuO_2 \cdot xH_2O$ (89 S/cm) is still an obstacle to balance the electronic and proton conduction channels for achieving the high power supercapacitor electrode.

In order to address these issues, recent progresses include the annealing of hydrous $RuO_2 \cdot xH_2O$ near to the crystallization temperature,[17] combining with other conductive nanomaterials such as activated carbon, carbon nanotubes, graphene,[18-24] and designing new architectures like nanotubes,[9,25] nanofibers of conductive networks.[17] Many of these approaches find their utilities in enhancing the specific capacitance; however, it is still challenging to retain the high capacitance of RuO_2 while achieving both good proton permeation and electronic conduction without an additional matrix.

Herein, we present the unique use of double hydrophilic block copolymer (DHBC) both as a soft template to prepare the hydrous RuO_2 nanoparticles with a controlled dimension and as a surface modifier to significantly increase the ionic conductivity of the resulting nanoparticles after the thermal annealing. In specific, the DHBC of poly(ethylene oxide)-*block*-poly(acrylic acid) (PEO-*b*-PAA) was employed to form a micelle upon addition of the ruthenium precursor, $RuCl_3 \cdot xH_2O$, which then transformed into hydrous RuO_2 nanoparticles of a controlled dimension using a reducing agent (**Scheme** 1). Furthermore, upon annealing of as-prepared RuO_2 nanoparticles at 400 ^oC, we find that the crystallinity of RuO_2 nanoparticles increases with a simultaneous transformation of the surrounding DHBC into ionic and electronic conducting buffer layer atop RuO_2 nanoparticles, which contribute to the significant enhancement of the overall specific capacitance of 962 F/g at a scan rate of 10 mV/s with excellent cycle life.

This DHBC-based method offers a unique and facile solution-based synthesis of

ULSAN NATIONAL INSTITUTE OF SCIENCE AND TECHNOLOGY

nanoparticles under mild conditions and does not require any foreign materials to increase the capacitance as well as to improve the rate capability during charging/discharging process. To the best of our knowledge, this is *the first example* of employing DHBCs in the synthesis of RuO_2 nanoparticles and its application in supercapacitor. Because the self-assembly of DHBC with metal precursor relies solely on the electrostatic interactions, we argue that this method can be readily extended to other nanoparticles of controlled dimension and structures. We envision that the DHBC will provide a facile and general tool in creating functional nanostructures for various applications.

ULSAN NATIONAL INSTITUTE OF SCIENCE AND TECHNOLOGY

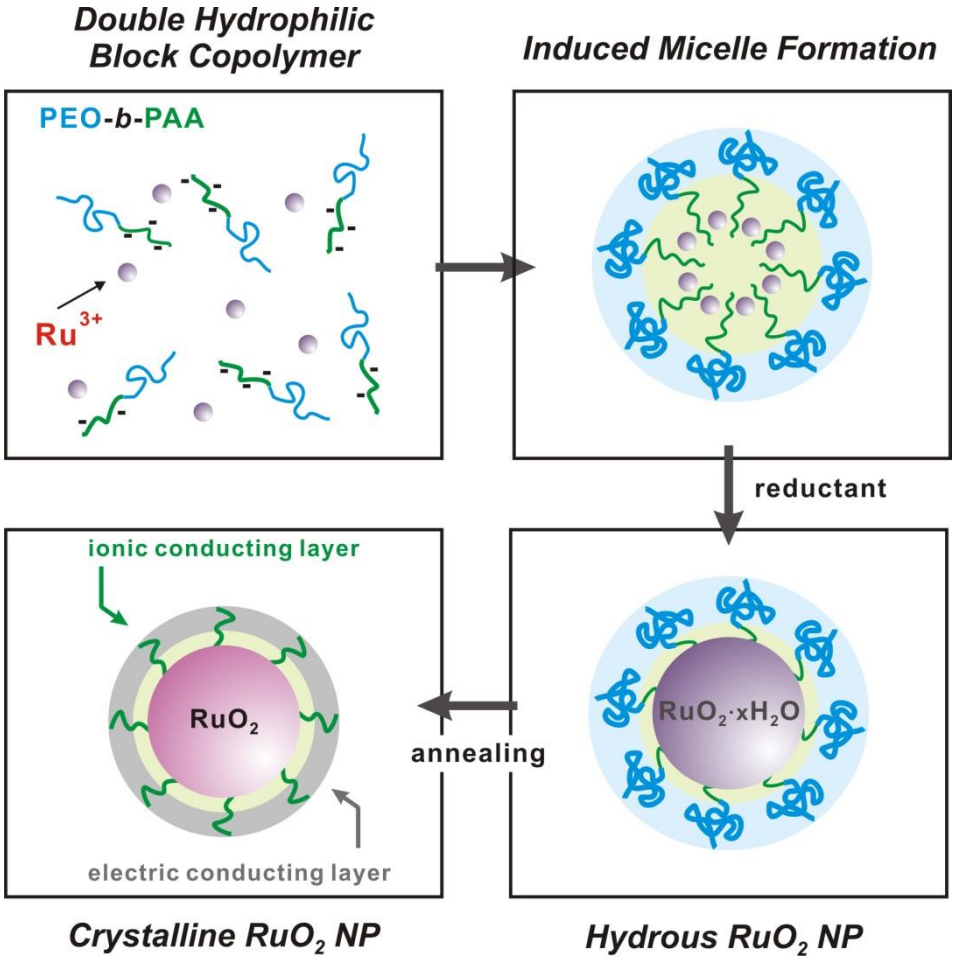

Scheme 5.1. Schematic illustration of synthesis of RuO_2 nanoparticles using double hydrophilic block copolymer as a template and resulting nanostructures after annealing at high temperature.

ULSAN NATIONAL INSTITUTE OF SCIENCE AND TECHNOLOGY

5.2. Experimental Section

Materials. Ruthenium(III) chloride hydrate ($RuCl_3 \cdot xH_2O$) and hydrazine (NH_2NH_2) were purchased from Aldrich and used without further purification. Double hydrophilic block copolymer of PEO(5000)-*b*-PAA(6700) was purchased from Polymer Source, Inc.

Synthesis of hydrous $RuO_2 \cdot xH_2O$ nanoparticles. The ruthenium oxide nanoparticles were prepared according to the following protocols. First, double hydrophilic block copolymer PEO(5000)-*b*-PAA(6700) (25.12 mg, 0.20 mmol of carboxylic acid groups) and $RuCl_3 \cdot xH_2O$ (17.8 mg, 0.10 mmol) in 5.0 mL of deionized water were prepared separately and mixed under vigorous stirring. To this solution mixture, 0.10 mL of 4.0 M NaOH (0.40 mmol, 2 equiv. to carboxylic acid groups) was added and the color in the solution was changed from black to dark cyan. Subsequently, 0.10 mL of 10.0 M hydrazine (1.0 mmol) was added dropwise to the resulting suspensions under vigorous stirring. As soon as the hydrazine is added, the solution color turns into light cyan. After 30 min of vigorous stirring, the solution mixture was centrifuged to remove large aggregates of nanoparticles (1500 rpm, 15 min), and then the recovered supernatant was dialyzed against deionized water using a dialysis membrane (MWCO 12000 – 14000, SpectraPore) for 6 h to remove any by-product and residuals. The prepared suspension of $RuO_2 \cdot xH_2O$ nanoparticles exhibited a fairly good colloidal stability more than 6 months without any precipitation. For annealing, the RuO_2 powder was first obtained by using a freeze dryer and this powder was subjected to annealing at different temperatures for 2 h in a muffle furnace under air atmosphere.

Characterization. The morphology, size, and size distributions of the prepared nanoparticles were investigated using a transmission electron microscopy (TEM, JEOL JEM-2100, accelerating voltage of 200 kV, Gatan CCD camera). X-ray diffraction measurements (XRD) were carried out with a high-power x-ray diffractometer (Rigaku Co., D/MAZX 2500V/PC) from 10° to 90°. X-ray photoelectron spectroscopy (XPS) measurements were performed on a Thermo Fisher, K-alpha. Thermogravimetric analysis (TGA) was conducted in air atmosphere at a heating rate of 10 ^oC/min using a thermogravimetric analyzer (Q200, TA Instrument). Fourier-transform infrared (FT-IR) spectra were obtained with a FT-IR spectraphotometer (Varian).

ULSAN NATIONAL INSTITUTE OF SCIENCE AND TECHNOLOGY

Electrochemical measurements. The working electrode was prepared by loading the prepared sample on the surface of quartz crystal microbalance (QCM) substrate coated with gold. Then, the weight of RuO_2 loaded on the surface of electrode is calculated from the frequency of eQCM (SEIKO, EG&G, QCA922-00). The electrochemical properties of RuO_2 electrodes were characterized by means of cyclic voltammetry and galvanostat (BioLogic, VSP) at ambient temperature. The CV measurements were carried out using a three-electrode cell, in which a platinum wire was used as counter-electrode and saturated calomel electrode (SCE) as a reference electrode, in the potential range of between -0.1 and +0.9 V with scan rates from 10 to 200 mV/s in an aqueous 1.0 M H_2SO_4 solution. The charge/discharge galvanostatic tests were performed at current densities from 3 to 20 A/g.

ULSAN NATIONAL INSTITUTE OF SCIENCE AND TECHNOLOGY

5.3. Results and Discussion

Synthesis and characterization of hydrous RuO_2 nanoparticles. The synthesis of RuO_2 nanoparticles by DHBCs is illustrated in Scheme 5.1. Traditionally, DHBCs have been employed in the growth control of inorganic mineralization with unusual structural specialty and complexity in aqueous solution such as $CaCO_3$, $BaSO_4$, and $Ca_3(PO_4)_2$;[26,27] however, there are only a few examples of employing the DHBCs in the synthesis of nanoparticles.[28-30] In our approach, we use PEO-*b*-PAA that consists of a binding ionizable PAA block and a solvating neutral PEO block, as stabilizers for the controlled synthesis of hydrous RuO_2 nanoparticles. Upon introduction of Ru^{3+} ions that interact with the ionizable PAA block in solution via electrostatic interactions, the PAA blocks are promoted to the formation of micellar aggregates in solution. The formation of micellar colloids with a similar core-shell structure was proposed with other metal ions complexing with DHBCs in previous reports.[31,32] Once the micelle formation is induced, the PEO-*b*-PAA micelle acts as a nanoreactor to control the nanoparticle growth within the micellar core with the addition of reducing agent, N_2H_4. The prepared homogeneous suspension of RuO_2 nanoparticles remains stable for several months without noticeable aggregates due to the PEO block that are sterically stabilizing the nanoparticles in aqueous solution (Figure. 5.1). A control experiment of using only PAA polymer of a similar molecular weight does not yield the stable suspension of hydrous RuO_2 nanoparticle, highlighting the important role of PEO block in stabilizing the nanoparticles. In addition, the selective interaction between the ionizable block of PAA with the Ru metal precursor was confirmed by the FT-IR spectra. The peak at 1570 cm^{-1} attributed to the stretching vibration of the carboxylate groups (COO^-) in PAA is considerably diminished after the addition of the Ru^{3+}, while the peak at 1104 cm^{-1} from the ether group (C-O-C) in PEO block does not change at all, suggesting the preferential interaction between PAA and metal precursor is dominant as presented in Scheme 5.1 and Figure 5.2.

The morphology and structure of the RuO_2 nanoparticles formed are investigated with transmission electron microscopy (TEM) (Figure 5.1), X-ray photoelectron spectroscopy (XPS) and X-ray diffraction (XRD) (Figure. 5.3). TEM image of the as-prepared RuO_2 nanoparticles shows a spherical shape of the RuO_2 nanoparticles with an average diameter 1.9 ± 0.63 nm. The average diameter of RuO_2 nanoparticles is also tunable with varying

ULSAN NATIONAL INSTITUTE OF SCIENCE AND TECHNOLOGY

ratio of metal precursor to DHBC in the range of ca. 1 – 3 nm (data not shown). Although the high-resolution TEM reveals the crystalline lattice fringe of 0.224 nm from some nanoparticles, which corresponds to the primary reflection of the (211) peak of RuO_2 nanoparticles, the XRD does not indicate the crystallinity of the RuO_2 nanoparticles prepared, suggesting the formation of amorphous $RuO_2 \cdot xH_2O$ nanoparticles. This is consistent with other studies of synthesizing RuO_2 nanoparticles under mild reaction temperature.[33,34]

XPS further reveals the oxidation status of as-prepared $RuO_2 \cdot xH_2O$ nanoparticles after the deconvolution of the peaks (Figure 5.3a). Though the $Ru3d_{5/2}$ and $3d_{3/2}$ signals are overlapping with the C1s peak centered at 284.0 eV, the signals at 280.9 and 285.6 eV can be assigned to Ru(IV) of RuO_2. The other two signals at 283.1 and 287.8 eV are characteristics of Ru(III) corresponding to hydrous Ru(III)-OH.[25] Moreover, the deconvoluted high-resolution O1s spectra of as-prepared $RuO_2 \cdot xH_2O$ nanoparticles exhibited three distinct components, including lattice oxygen O^{2-} in RuO_2 (530.2 eV), hydroxyl (532.0 eV), and surface bound H_2O (533.9 eV), which are all in good agreement with previous reports. Collectively, the TEM and XPS data support the successful formation of hydrous $RuO_2 \cdot xH_2O$ nanoparticles with the DHBC template.

As introduced, the careful control over the degree of crystallinity and hydration is essential in reaching high capacitance with enhanced cycle life that are related to the electrical and electrochemical properties of RuO_2-based materials. Thus, as-prepared hydrous $RuO_2 \cdot xH_2O$ nanoparticles were subjected to thermal annealing under different temperatures (200 to 600 ^oC) for 2 h to tune the level of crystallinity and the hydration of the RuO_2 nanoparticles and XRD followed to elucidate these changes in RuO_2 nanoparticles (Figure 5.3b).

As shown in Figure 5.3, the crystallinity of RuO_2 nanoparticles increases considerably upon annealing at high temperature. For example, the peaks related to the rutile phase of RuO_2 such as (101), (110), and (211) begin to evolve after heat treatment at 300 ^oC and becomes apparent after annealing beyond 400 ^oC (Figure 5.4). While annealing of as-prepared hydrous $RuO_2 \cdot xH_2O$ nanoparticles crystallized the inorganic network, the organic DHBC micelles surrounding the RuO_2 nanoparticles also began to decompose, resulting in an amorphous carbon layer on top of RuO_2 nanoparticles, which is not clearly discernable by XRD. Moreover, it should be noted that there are still some polymeric

ULSAN NATIONAL INSTITUTE OF SCIENCE AND TECHNOLOGY

layers remaining even after annealing at 400 ^{o}C, as evidenced by the presence of residual polymeric layers using FT-IR, including symmetric stretching of carboxylate peaks from PAA at 1435 cm^{-1} and strong rocking of PAA backbone at 863 cm^{-1}, which reflect the surface-bound strong coordinating carboxylate groups in PAA (Figure 5.5). In contrast, we could not observe any residual peaks relevant to PEO block after thermal annealing above 400 ^{o}C, suggesting the selective degradation of PEO block took place below 400 ^{o}C. It turns out that this residual polymeric layer of DHBC, which mainly consists of PAA block and amorphous carbon layer, serves a critical role in increasing the ionic and electronic conduction pathway during electrochemical cycles. Taken together, we postulate that as-prepared hydrous RuO_2 nanoparticles undergo the phase transition from amorphous to crystalline state upon thermal annealing with the formation of residual polymeric layer on top of nanoparticles. TEM measurements also indicate the size of nanoparticles increases gradually with the progress of annealing (Figure 5.6).

The thermal stability as well as the relative content of the polymer in the as-prepared $RuO_2 \cdot xH_2O$ nanoparticles was estimated based on the thermogravimetric analysis (TGA) measurement (Figure 5.7). As shown in the TGA curve of as-prepared hydrous $RuO_2 \cdot xH_2O$ nanoparticles, initial mass loss of water at around 62.8 ^{o}C was observed. Followed by the initial mass loss, the second mass loss began at around 250 ^{o}C, which is associated with the degradation of DHBCs. Subsequently, a characteristic peaks in the range of 300 - 400 ^{o}C was observed according to the differential TGA curve, which are attributed to the removal of crystalline water in hydrous RuO_2,[24,35] suggesting the initially formed amorphous hydrous RuO_2 was transformed into a crystalline phase near at 400 ^{o}C. As stated in the description of XRD, the existence of residual polymers at 400 ^{o}C is clearly evidenced by the presence of the peak near at 607 ^{o}C, indicating the complete degradation of DHBCs at this temperature. The subsequent weight loss corresponds to the conversion of residual DHBCs into amorphous carbonaceous layer on top of nanoparticles, which leads to approximately 38% of RuO_2 are present within the resulting nanocomposite. RuO_2 nanoparticles annealed at higher temperatures generally yield more amount of nanoparticles with respect to the polymer content from 19% (as-prepared) to 76% (annealed at 600 ^{o}C), as the polymer decomposed during the annealing process. In concert with the FT-IR data, TGA also provided that the specific interaction between the polymer and the metal precursor increased degradation temperature of pure PEO-*b*-PAA from 525

ULSAN NATIONAL INSTITUTE OF SCIENCE AND TECHNOLOGY

to 611 ^{o}C. This also demonstrates the strong interaction between the metal ions and DHBCs.

Electrochemical behavior of RuO_2 electrode in supercapacitor. The capacitive performance of the prepared RuO_2 nanoparticles was evaluated by using cyclic voltammetry (CV) (Figure 5.8). Figure 5.8 shows the CV results of all RuO_2 nanoparticles prepared before and after the annealing at different temperatures, which were measured in 1.0 M H_2SO_4 at potential intervals from -0.1 to 0.9 V using saturated calomel electrode (SCE) as a reference electrode. All samples exhibit broad redox peaks in the potential range investigated, which displays a typical pseudocapacitive behavior of RuO_2 nanoparticles. The specific capacitance (C_{sp}) was calculated by following equation.[23]

$$C_{sp} = \frac{1}{\mathrm{mv}(V_f - V_i)} \int_{V_i}^{V_f} I(V)dV$$

,where *m* is the mass of the active electrode materials measured by quartz crystal microbalance (QCM), *v* is the scan rate, *V* is the integration potential limit, and I(V) is the voltammetric current. As shown in Figure 5.8, the specific capacitances of as-prepared RuO_2, annealed at 200, 400, and 600 ^{o}C obtained at 10 mV/s are 106, 358, 962, and 25 F/g, respectively. As-prepared hydrous $RuO_2 \cdot xH_2O$ nanoparticles within a polymeric shell of DHBC did not show a noticeable capacitive activity possibly due to the existence of DHBCs on top of the nanoparticles which prevent the effective current pathway. On the other hand, the samples after annealing generally show the significantly enhanced capacitance values and, to our surprise, the sample annealed at 400 ^{o}C exhibits an outstanding specific capacitance of 962 F/g at a scan rate of 10 mV/s and even holds the specific capacitance of 430 F/g at a fast scan rate of 200 mV/s. Besides, a linear response of the capacitive current with respect to potential scan rate reveals the high reversibility of the system. Furthermore, it is important to note that the capacitance loss of the sample at a high scan rate is still moderate compared to other samples. This considerable difference in the specific capacitance is mainly attributed to the degree of crystallinity as well as the hydration, and most importantly, the role of residual DHBC in enhancing the ionic and electronic conductivity of the materials at the interface between the RuO_2 nanoparticles and H_2SO_4 electrolyte. The sample annealed at a higher temperature of 600 ^{o}C, however, displays a poor capacitance of 25 F/g even at a higher crystallinity of RuO_2

ULSAN NATIONAL INSTITUTE OF SCIENCE AND TECHNOLOGY

nanoparticle. This is primarily attributed to the dense crystalline structure of RuO_2 as well as the disappearance of residual ionic conducting layer on top of RuO_2 nanoparticles, which hamper the effective transport of protons upon complete removal of DHBCs. This is in accord with the high-resolution TEM image showing the highly crystalline carbon layer on top of RuO_2 nanoparticles (Figure 5.9).

Finally, we evaluated the cycling stability of the RuO_2 nanoparticles annealed at 400 ^{o}C using galvanostat charge/discharge test under the identical three-electrode system. As shown in Figure 5.8d, the non-linear charge/discharge curve featured the characteristic pseudocapacitive behavior of the sample. The specific capacitance of supercapacitor was calculated to be 800 F/g at a current density of 3 A/g, which is similar to that obtained from the CV measurement. This value is comparable to the recent study of Sassoye and co-workers reporting RuO_2-based mesoporous thin film prepared by amphiphilic block copolymer, PS-*b*-PEO, having a capacitance of 1000 ± 100 F/g and the other study of Huang co-workers reporting a capacitance of 653 F/g from hydrous RuO_2 loaded into PEDOT:PSS matrix.[15,36] Most notably, the excellent cycle life of the electrode is demonstrated with the 100% retention of capacitance even after 1000 cycles at a high current density of 20 A/g. It has been often observed that the RuO_2 nanoparticles often undergo irreversible aggregation after cycles of charging/discharging, which may significantly degrade their electrochemical redox processes at the interface with the electrolytes. However, in this case, the residual polymeric layer on top of RuO_2 nanoparticles not only prevents the re-aggregation of the active nanoparticles, but also provides an intimate ionic and electronic conducting pathway with electrolytes, leading to the rapid and efficient redox reactions on the surface of RuO_2 nanoparticles (Figure 5.10). Further electrochemical impedance measurements also support the markedly increased electrochemical property of RuO_2 nanoparticles annealed at 400 ^{o}C comparing to that of as-prepared hydrous $RuO_2 \cdot xH_2O$ nanoparticles (Figure 5.11). Although more stringent tests are still required, we have further optimized the current annealing temperature to different ranges near 400 ^{o}C and found that annealing of hydrous $RuO_2 \cdot xH_2O$ nanoparticles at 350 ^{o}C yielded a capacitance of even to 1070 F/g at a scan rate of 10 mV/s, which is about 11% capacitance increase comparing to that annealed at 400 ^{o}C (Figure 5.12).

ULSAN NATIONAL INSTITUTE OF
SCIENCE AND TECHNOLOGY

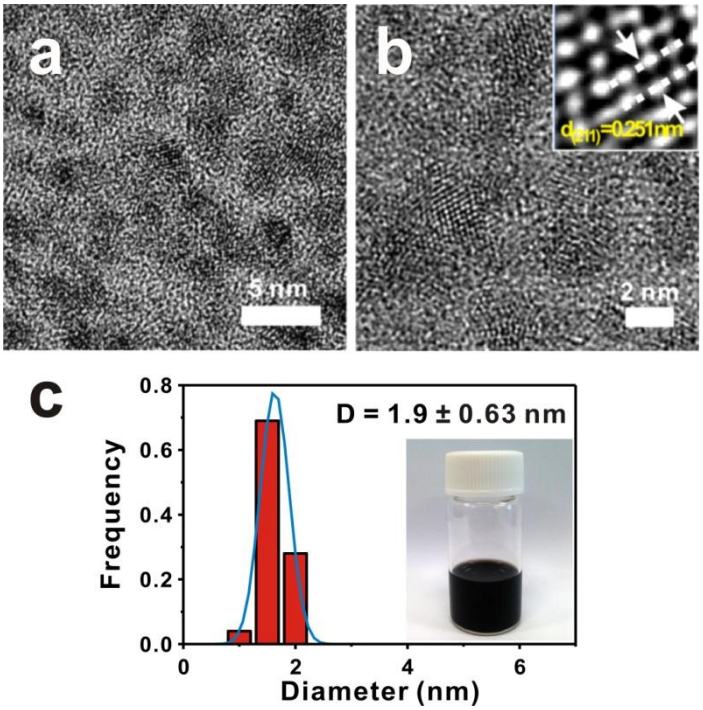

Figure 5.13. (a,b) TEM images of as-prepared hydrous $RuO_2 \cdot xH_2O$ nanoparticles. Inset in Figure 5.1b shows the crystalline lattice fringe of $RuO_2 \cdot xH_2O$ nanoparticles. (c) Corresponding size distribution histogram with an image of as-prepared hydrous $RuO_2 \cdot xH_2O$ nanoparticle suspension.

ULSAN NATIONAL INSTITUTE OF SCIENCE AND TECHNOLOGY

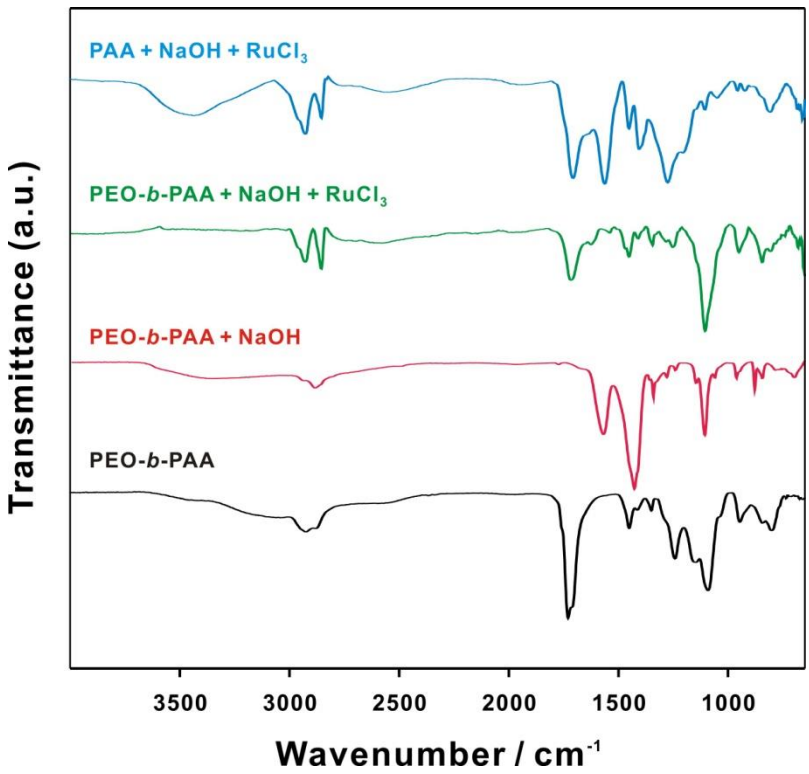

Figure 5. 14. FT-IR spectra of (a) PEO-*b*-PAA, (b) PEO-*b*-PAA with NaOH, (c) PEO-*b*-PAA with NaOH and $RuCl_3 \cdot xH_2O$, and (d) PAA with NaOH and $RuCl_3 \cdot xH_2O$. Note that the PEO-*b*-PAA shows the C=O stretching vibration of the carboxylic group at 1729 cm^{-1} and the C-O stretching vibration of PEO block and PAA block at 1241 and 1091 cm^{-1}, respectively. Upon complexation with Ru^{3+} through electrostatic interaction to form micellar structure, the carboxylic acid groups of PAA block are dissociated into COO^- groups, which correspond to the absorption peaks at 1625 and 1410 cm^{-1} assigned to asymmetric and symmetric stretching vibrations of COO^-, while a peak of C-O observed in PEO block still remains at 1104 cm^{-1}. This implies that the carboxylate groups of PAA block are easily involved in the reaction by combining with Ru^{3+}. In a control experiment using only PAA polymer, the absorption peaks at 1561 and 1404 cm^{-1} could be assigned to asymmetric and symmetric stretching vibrations of COO^-, supporting carboxylate groups in PAA complex with Ru^{3+}.

ULSAN NATIONAL INSTITUTE OF
SCIENCE AND TECHNOLOGY

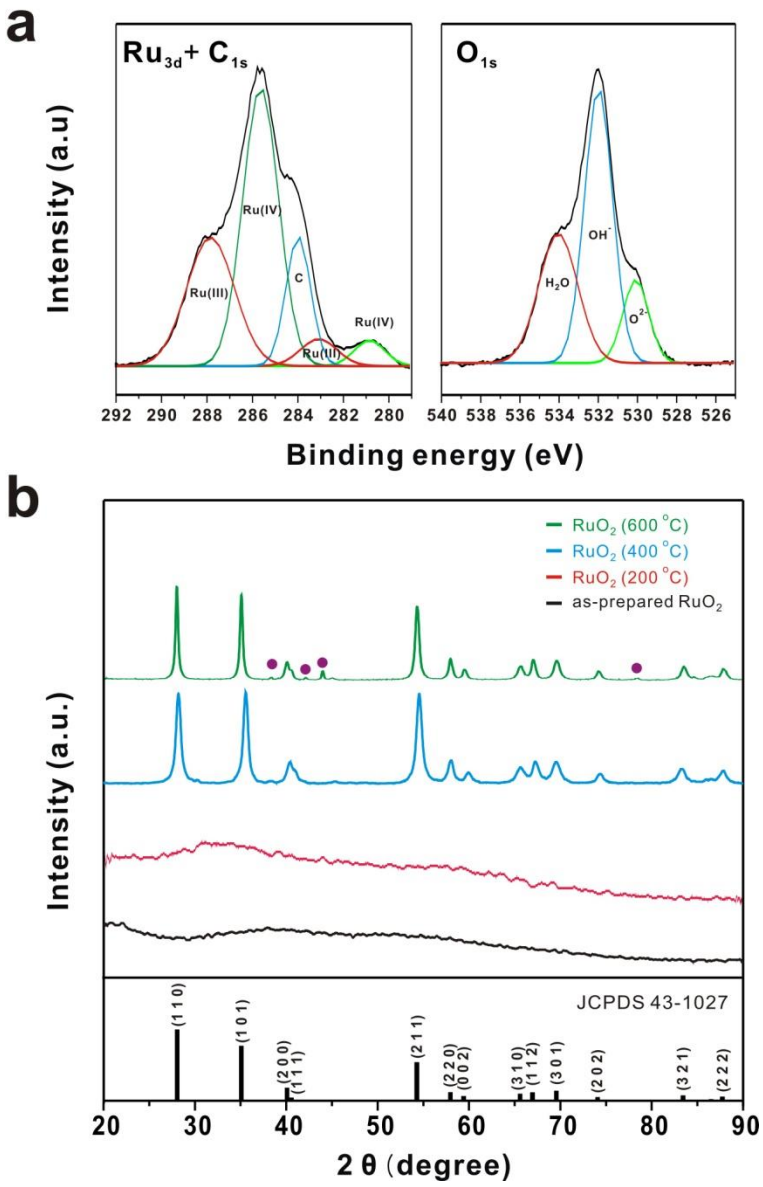

Figure 5.15. (a) Deconvoluted high-resolution XPS spectra of as-prepared hydrous $RuO_2 \cdot xH_2O$ nanoparticles. (b) XRD spectra of various RuO_2 nanoparticles before and after annealing at different temperatures. Note the circles in Figure 2b represent the peak matching to metallic ruthenium.

ULSAN NATIONAL INSTITUTE OF
SCIENCE AND TECHNOLOGY

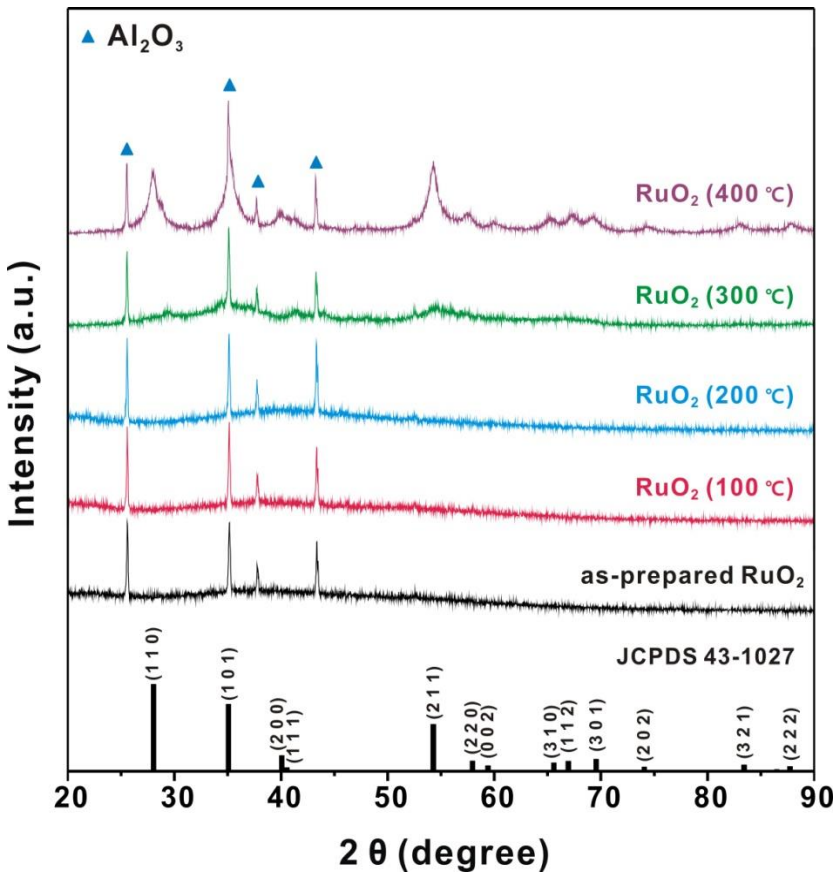

Figure 5.16. *In situ* XRD patterns of hydrous $RuO_2 \cdot xH_2O$ nanoparticles with increasing temperature under ambient condition. It indicates that the crystalline RuO_2 structure is evolved from amorphous structure of as-prepared hydrous $RuO_2 \cdot xH_2O$ near at 300 ^oC. Note that the peaks marked with blue triangle are assigned to the Al_2O_3substrate, where the sample was loaded.

ULSAN NATIONAL INSTITUTE OF
SCIENCE AND TECHNOLOGY

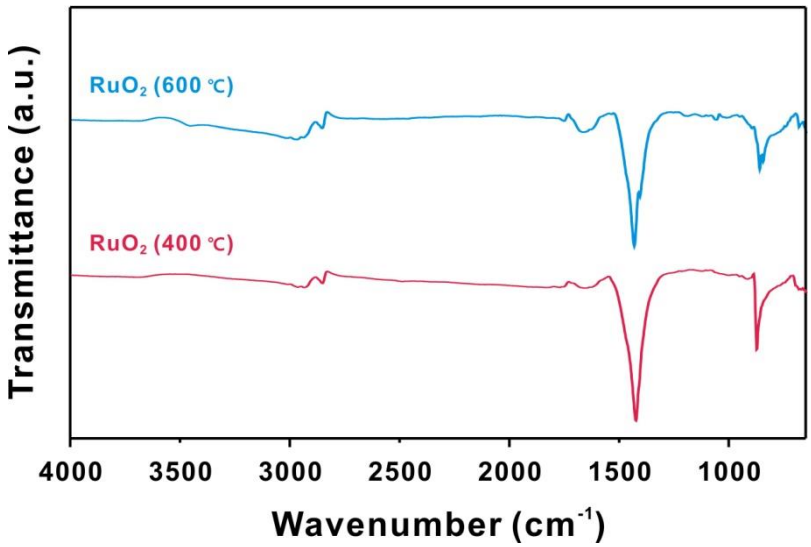

Figure 5. 17. FT-IR spectra of RuO_2 nanoparticles annealed at 400 ^oC and 600 ^oC. Both spectra reveals the presence of residual polymeric layer, including symmetric stretching of carboxylate peaks at 1435 cm^{-1}, which corresponds to the surface-bound strong coordinating carboxylate groups, and the other strong peak observed at 863 cm^{-1} due to the strong rocking of methylene ($-CH_2-$) backbone of the polymer.

ULSAN NATIONAL INSTITUTE OF
SCIENCE AND TECHNOLOGY

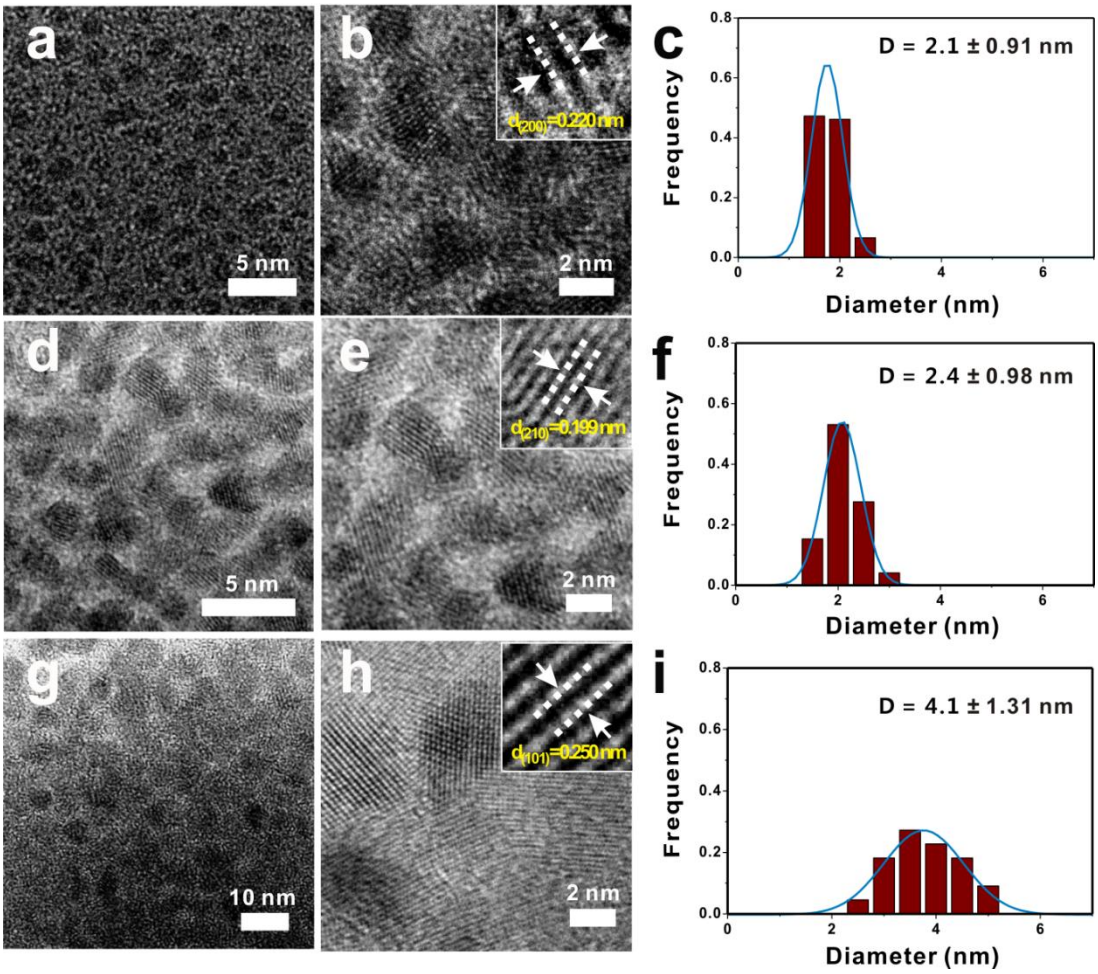

Figure 5.18. Representative TEM images of RuO_2 nanoparticles annealed at various temperatures. (a, b) 200 °C, (d, e) 400 °C and (g, h) 600 °C. The inset images show the crystalline plane of RuO_2 nanoparticles. (c, f, i) The corresponding size distribution histograms of RuO_2 nanoparticles averaged over 50 samples.

ULSAN NATIONAL INSTITUTE OF
SCIENCE AND TECHNOLOGY

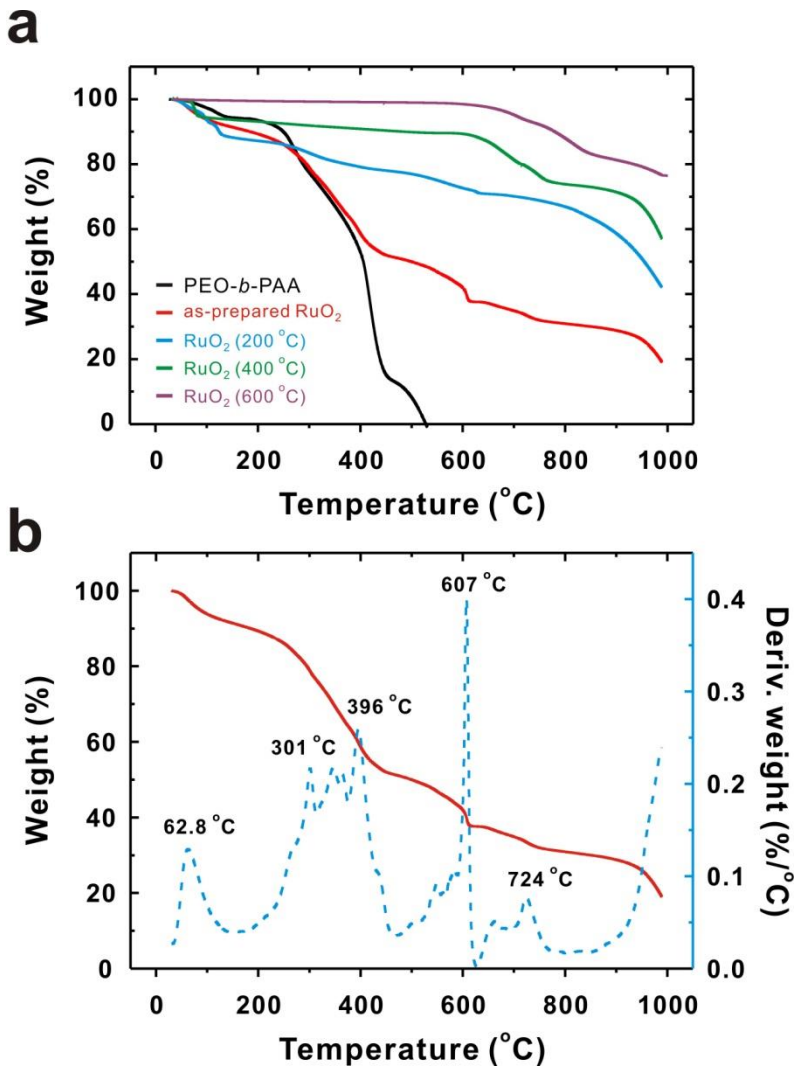

Figure 5.19. (a) Thermogravimetric analysis (TGA) and (b) differential thermal analysis (DTA) curves of as-prepared hydrous $RuO_2 \cdot xH_2O$ nanoparticles. The sample was subjected to heating at a rate of 10 °C/min under air atmosphere.

ULSAN NATIONAL INSTITUTE OF
SCIENCE AND TECHNOLOGY

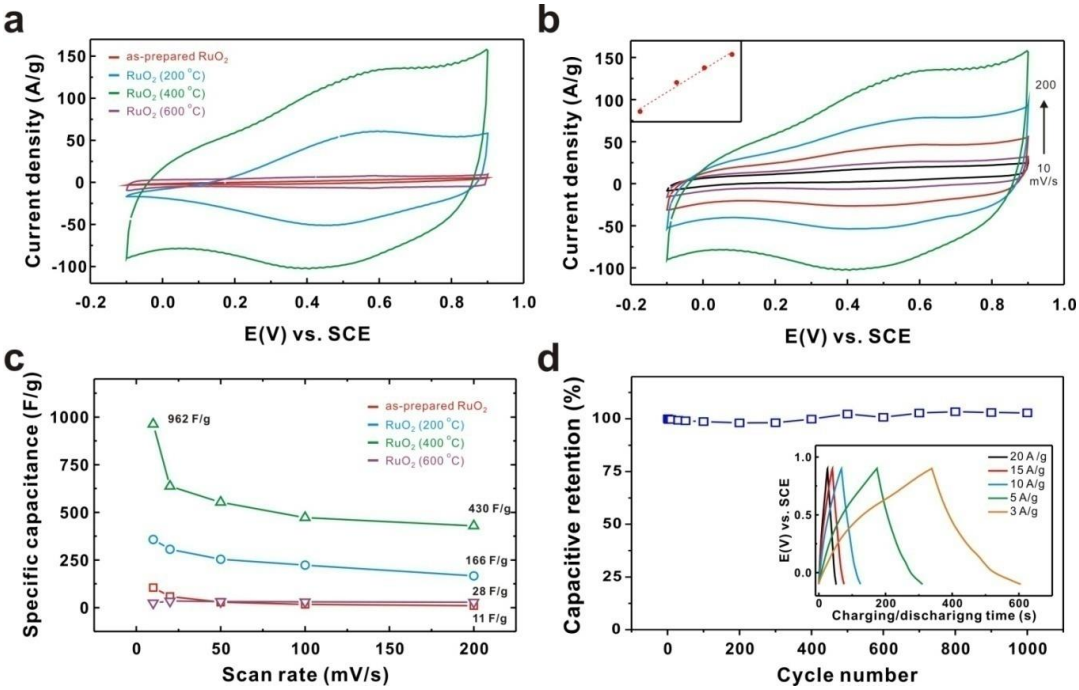

Figure 5.20. Comparison of electrochemical properties of all RuO_2 nanoparticle samples. (a) Cyclic voltammograms (CVs) of RuO_2 nanoparticle electrodes at a scan rate of 200 mV/s, (b) scan rate dependent current density plot of RuO_2 nanoparticles after annealing at 400 ^oC with a scan rate of 10, 20, 50, 100, 200 mV/s. Inset shows the peak current density versus scan rate plot in an equi-span log-log scale with a calculated slope of 1.0, (c) dependence of the capacitance loss on the scan rate of all RuO_2 nanoparticle samples, and (d) galvanostat cycling of RuO_2 after annealing at 400 ^oC with a current density of 20 A/g. Inset shows the charge/discharge curves with various current densities. All electrochemical properties were collected in a three-electrode system with a SCE reference in 1.0 M H_2SO_4 electrolyte.

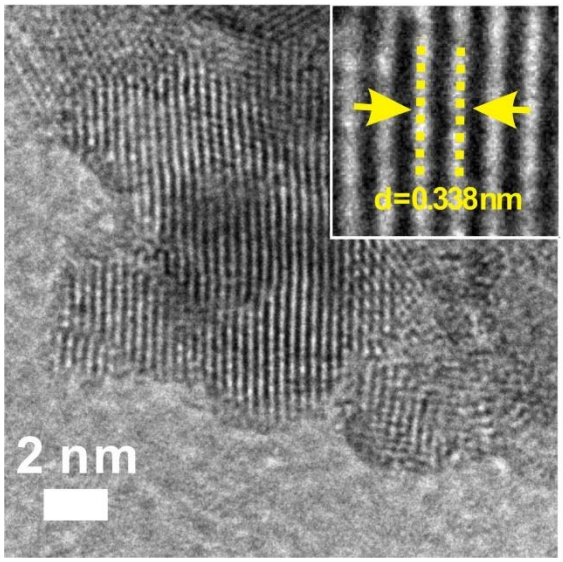

Figure 5. 21. Representative HR-TEM image of RuO_2 nanoparticles annealed at 600 ^oC. Highly crystalline carbon layer is formed on the surface of RuO_2 nanoparticles.

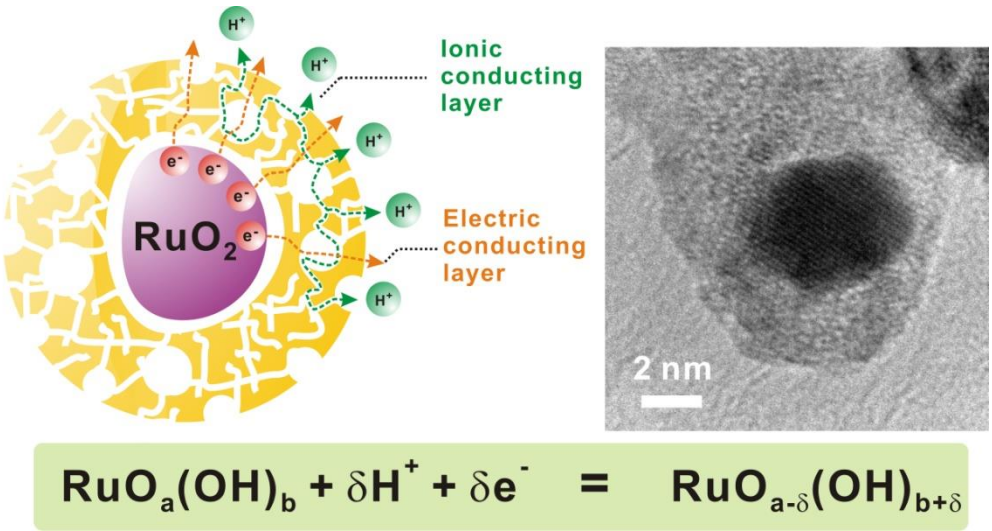

Figure 5.22. Schematic representation of the origin of enhanced capacitive performance of RuO_2 nanoparticles annealed at 400 ^oC with the corresponding TEM image.

ULSAN NATIONAL INSTITUTE OF
SCIENCE AND TECHNOLOGY

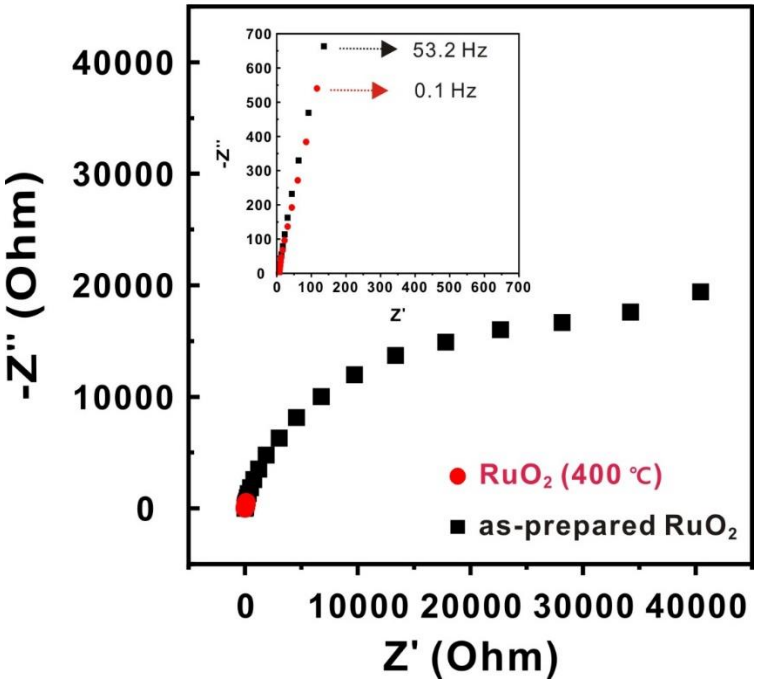

Figure 5. 23. Nyquist plots for an electrode of (black square) as-prepared RuO_2 and (red circle) RuO_2 annealed at 400 ^{o}C, measured over a frequency range from 100 mHz to 200 kHz at 0.6 V.

ULSAN NATIONAL INSTITUTE OF SCIENCE AND TECHNOLOGY

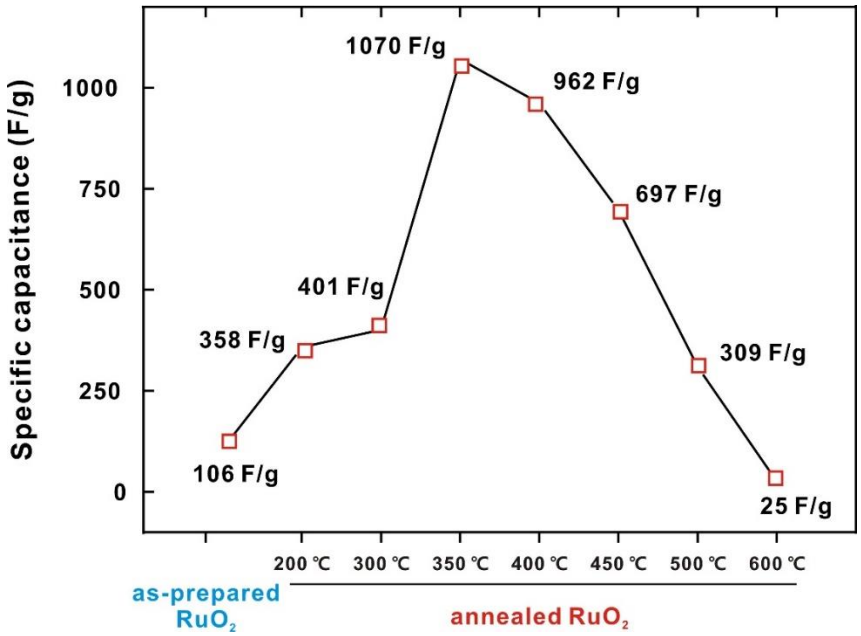

Figure 5.24. Comparison of capacitance values of all RuO_2 nanoparticles samples annealed at different temperature ranges. Capacitance values were obtained with a cyclic voltammetry measurement at a scan rate of 10 mV/s.

Table 5. 2. Comparison of capacitance values of all RuO_2 nanoparticles samples annealed at different temperature ranges measured at various scan rates.

Scan rate (mV/s)	as-prepared hydrous RuO_2	annealed RuO_2 nanoparticles						
		200°C	300°C	350°C	400°C	450°C	500°C	600°C
10	106	358	401	1070	962	697	309	25
20	59	306	314	953	637	464	293	35
50	29	254	260	858	553	426	284	32
100	17	223	231	819	472	396	276	30
200	11	166	209	751	430	362	266	28

ULSAN NATIONAL INSTITUTE OF SCIENCE AND TECHNOLOGY

5.4. Conclusion

In summary, we have developed a facile synthesis of ruthenium oxide (RuO_2) nanoparticles using double hydrophilic block copolymer, PEO-*b*-PAA, as a soft template and demonstrated its promising potential for supercapacitors. The stable suspension of hydrous $RuO_2 \cdot xH_2O$ nanoparticles of a controlled dimension was prepared under a mild aqueous condition. Furthermore, we found that upon annealing of as-prepared hydrous $RuO_2 \cdot xH_2O$ nanoparticles at 400 ^{o}C, the crystallinity of RuO_2 nanoparticles increased with a simultaneous transformation of the surrounding DHBC into ionic conducting buffer layer atop RuO_2 nanoparticles, which contributed to the significant enhancement of the overall specific capacitance of 962 F/g at a scan rate of 10 mV/s with an excellent cycle life over 1000 times. Because the self-assembly of DHBCs with metal precursor relies solely on the electrostatic interactions, we argue that this method can be readily extended to other nanoparticles of controlled dimension and structures. We envision that the DHBC will provide a facile and general means in creating other functional nanostructures for various applications.

ULSAN NATIONAL INSTITUTE OF SCIENCE AND TECHNOLOGY

5.5. References

(1) Conway, B. E., *Electrochemical Supercapacitors: Scientific Fundamentals and Technological Applications*. Kluwer Academic/Plenum: New York, 1999.

(2) Arico, A. S.; Bruce, P.; Scrosati, B.; Tarascon, J. M.; Van Schalkwijk, W., Nanostructured Materials for Advanced Energy Conversion and Storage Devices. *Nat. Mater.* **2005,** *4*, 366-377.

(3) Hall, P. J.; Mirzaeian, M.; Fletcher, S. I.; Sillars, F. B.; Rennie, A. J. R.; Shitta-Bey, G. O.; Wilson, G.; Cruden, A.; Carter, R., Energy Storage in Electrochemical Capacitors: Designing Functional Materials to Improve Performance. *Energy Environ. Sci.* **2010,** *3*, 1238-1251.

(4) Liu, C.; Li, F.; Ma, L. P.; Cheng, H. M., Advanced Materials for Energy Storage. *Adv. Mater.* **2010,** *22*, E28-E62.

(5) Simon, P.; Gogotsi, Y., Materials for Electrochemical Capacitors. *Nat. Mater.* **2008,** *7*, 845-854.

(6) Stoller, M. D.; Ruoff, R. S., Best Practice Methods for Determining an Electrode Material's Performance for Ultracapacitors. *Energy Environ. Sci.* **2010,** *3*, 1294-1301.

(7) Conway, B.; Birss, V.; Wojtowicz, J., The Role and Utilization of Pseudocapacitance for Energy Storage by Supercapacitors. *J. Power Sources* **1997,** *66*, 1-14.

(8) Hu, C. C.; Chang, K. H.; Lin, M. C.; Wu, Y. T., Design and Tailoring of the Nanotubular Arrayed Architecture of Hydrous RuO_2 for Next Generation Supercapacitors. *Nano Lett.* **2006,** *6*, 2690-2695.

(9) Liu, R.; Duay, J.; Lane, T.; Lee, S. B., Synthesis and Characterization of RuO_2/Poly(3, 4-ethylenedioxythiophene) Composite Nanotubes for Supercapacitors. *Phys. Chem. Chem. Phys.* **2010,** *12*, 4309-4316.

(10) Liu, X.; Pickup, P. G., Performance and Low Temperature Behaviour of Hydrous Ruthenium Oxide Supercapacitors with Improved Power Densities. *Energy Environ. Sci.* **2008,** *1*, 494-500.

(11) Susanti, D.; Tsai, D. S.; Huang, Y. S.; Korotcov, A.; Chung, W. H., Structures and Electrochemical Capacitive Properties of RuO_2 Vertical Nanorods Encased in Hydrous RuO_2. *J. Phys. Chem. C* **2007,** *111*, 9530-9537.

(12) Ye, J. S.; Cui, H. F.; Liu, X.; Lim, T. M.; Zhang, W. D.; Sheu, F. S., Preparation and

ULSAN NATIONAL INSTITUTE OF SCIENCE AND TECHNOLOGY

Characterization of Aligned Carbon Nanotube–Ruthenium Oxide Nanocomposites for Supercapacitors. *Small* **2005,** *1*, 560-565.

(13) Chang, K. H.; Hu, C. C., Hydrothermal Synthesis of Hydrous Crystalline RuO_2 Nanoparticles for Supercapacitors. *Electrochem. Solid-State Lett.* **2004,** *7*, A466.

(14) Chang, K. H.; Hu, C. C., Oxidative Synthesis of $RuO_2 \cdot nH_2O$ with Ideal Capacitive Characteristics for Supercapacitors. *J. Electrochem. Soc.* **2004,** *151*, A958.

(15) Sassoye, C.; Laberty, C.; Le Khanh, H.; Cassaignon, S.; Boissière, C.; Antonietti, M.; Sanchez, C., Block-Copolymer-Templated Synthesis of Electroactive RuO_2-Based Mesoporous Thin Films. *Adv. Funct. Mater.* **2009,** *19*, 1922-1929.

(16) Zheng, J.; Cygan, P.; Jow, T., Hydrous Ruthenium Oxide as an Electrode Material for Electrochemical Capacitors. *J. Electrochem. Soc.* **1995,** *142*, 2699.

(17) Hyun, T. S.; Tuller, H. L.; Youn, D. Y.; Kim, H. G.; Kim, I. D., Facile Synthesis and Electrochemical Properties of RuO_2 Nanofibers with Ionically Conducting Hydrous Layer. *J. Mater. Chem.* **2010,** *20*, 9172-9179.

(18) Su, Y.; Wu, F.; Bao, L.; Yang, Z., RuO_2/Activated Carbon Composites as a Positive Electrode in an Alkaline Electrochemical Capacitor. *New Carbon Materials* **2007,** *22*, 53-57.

(19) Zhang, J.; Jiang, D.; Chen, B.; Zhu, J.; Jiang, L.; Fang, H., Preparation and Electrochemistry of Hydrous Ruthenium Oxide/Active Carbon Electrode Materials for Supercapacitor. *J. Electrochem. Soc.* **2001,** *148*, A1362.

(20) Arabale, G.; Wagh, D.; Kulkarni, M.; Mulla, I.; Vernekar, S.; Vijayamohanan, K.; Rao, A., Enhanced Supercapacitance of Multiwalled Carbon Nanotubes Functionalized with Ruthenium Oxide. *Chem. Phys. Lett.* **2003,** *376*, 207-213.

(21) Fang, W. C.; Chyan, O.; Sun, C. L.; Wu, C. T.; Chen, C. P.; Chen, K. H.; Chen, L. C.; Huang, J. H., Arrayed Cnx Nt-RuO_2 Nanocomposites Directly Grown on Ti-Buffered Si Substrate for Supercapacitor Applications. *Electrochem. Commun.* **2007,** *9*, 239-244.

(22) Kim, Y. T.; Tadai, K.; Mitani, T., Highly Dispersed Ruthenium Oxide Nanoparticles on Carboxylated Carbon Nanotubes for Supercapacitor Electrode Materials. *J. Mater. Chem.* **2005,** *15*, 4914-4921.

(23) Wu, Z. S.; Wang, D. W.; Ren, W.; Zhao, J.; Zhou, G.; Li, F.; Cheng, H. M., Anchoring Hydrous RuO_2 on Graphene Sheets for High-Performance Electrochemical Capacitors. *Adv. Funct. Mater.* **2010,** *20*, 3595-3602.

ULSAN NATIONAL INSTITUTE OF SCIENCE AND TECHNOLOGY

(24) Zhang, J.; Jiang, J.; Li, H.; Zhao, X., A High-Performance Asymmetric Supercapacitor Fabricated with Graphene-Based Electrodes. *Energy Environ. Sci.* **2011,** *4*, 4009-4015.

(25) Zhang, J.; Ma, J.; Zhang, L. L.; Guo, P.; Jiang, J.; Zhao, X., Template Synthesis of Tubular Ruthenium Oxides for Supercapacitor Applications. *J. Phys. Chem. C* **2011,** *114*, 13608–13613.

(26) Cölfen, H., Double-Hydrophilic Block Copolymers: Synthesis and Application as Novel Surfactants and Crystal Growth Modifiers. *Macromol. Rapid Commun.* **2001,** *22*, 219-252.

(27) Nakashima, K.; Bahadur, P., Aggregation of Water-Soluble Block Copolymers in Aqueous Solutions: Recent Trends. *Adv. Colloid Interface Sci.* **2006,** *123*, 75-96.

(28) Kim, A.; Sharma, B.; Kim, B. S.; Park, K. H., Double-Hydrophilic Block Copolymer Nanoreactor for the Synthesis of Copper Nanoparticles and for Application in Click Chemistry. *J. Nanosci. Nanotechnol.* **2011,** *11*, 6162-6166.

(29) Qi, L.; Cölfen, H.; Antonietti, M., Synthesis and Characterization of Cds Nanoparticles Stabilized by Double-Hydrophilic Block Copolymers. *Nano Lett.* **2001,** *1*, 61-65.

(30) Taubert, A.; Palms, D.; Weiss, Ö.; Piccini, M. T.; Batchelder, D. N., Polymer-Assisted Control of Particle Morphology and Particle Size of Zinc Oxide Precipitated from Aqueous Solution. *Chem. Mater.* **2002,** *14*, 2594-2601.

(31) Bouyer, F.; Sanson, N.; Destarac, M.; Gérardin, C., Hydrophilic Block Copolymer-Directed Growth of Lanthanum Hydroxide Nanoparticles. *New J. Chem.* **2006,** *30*, 399-408.

(32) Bronstein, L.; Sidorov, S.; Gourkova, A.; Valetsky, P.; Hartmann, J.; Breulmann, M.; Colfen, H.; Antonietti, M., Interaction of Metal Compounds with 'Double-Hydrophilic' Block Copolymers in Aqueous Medium and Metal Colloid Formation. *Inorg. Chim. Acta* **1998,** *280*, 348-354.

(33) Gujar, T.; Shinde, V.; Lokhande, C.; Kim, W. Y.; Jung, K. D.; Joo, O. S., Spray Deposited Amorphous RuO_2 for an Effective Use in Electrochemical Supercapacitor. *Electrochem. Commun.* **2007,** *9*, 504-510.

(34) Walker, J.; Bruce King, R.; Tannenbaum, R., Sol-Gel Synthesis of Hydrous Ruthenium Oxide Nanonetworks from 1, 2-Epoxides. *J. Solid State Chem.* **2007,** *180*,

ULSAN NATIONAL INSTITUTE OF SCIENCE AND TECHNOLOGY

2290-2297.

(35) Zheng, J. P., High Energy Density Electrochemical Capacitors without Consumption of Electrolyte. *J. Electrochem. Soc.* **2009,** *156*, A500.

(36) Huang, L. M.; Lin, H. Z.; Wen, T. C.; Gopalan, A., Highly Dispersed Hydrous Ruthenium Oxide in Poly(3, 4-ethylenedioxythiophene)-Poly(styrene sulfonic acid) for Supercapacitor Electrode. *Electrochim. Acta* **2006,** *52*, 1058-1063.

***** Chapter 5 is reproduced in part with permission of *"Seo, E.; Lee, T.; Lee, K. T.; Song, H. K.; Kim, B. S., J. Mater. Chem.2012, 22, 11598−11604".* Copyright 2012, Royal Society of Chemistry.

ULSAN NATIONAL INSTITUTE OF SCIENCE AND TECHNOLOGY

Chapter 6.

Conclusions and Prospects

The thesis have concentrated on the research of nanoparticles induced by entirely water-soluble double hydrophilic block copolymer and metal ions in aqueous solution and their wide applications including energy conversion and storage, or catalytic reaction.

Among numerous candidates for nanomaterials preparation, we have been interested in double hydrophilic block copolymer because of a potential of various characteristics like surfactant, ligand, or polymer that is partially hydrophobic under specific condition, during the formation of nanoparticles. Particularly, micellization by complex with metal ions, and protection of polymeric shell are an important characteristic during the formation of nanoparticles, a successful preparation of various types of metals or metal oxide, and shapes supported the practical examples of DHBC applicable in nano-scale synthesis.

A study in this thesis demonstrate that the size and size distribution of nanoparticle by copolymer should depend on the molecular weight of ionic block, further, affecting the stability of synthesized nanoparticles. We believe that the control of composition and length in each block of copolymer will allow us to be able to make a nanomaterial applicable in wide application.

Considering that multifunctional characteristic of DHBCs, we anticipate that the synthetic approaches on the basis of DHBC in nanomaterials will be opening the new concept of nano-scale chemistry, and also we hope our attempts in this thesis will be a converstone of basic research in polymer-based nanomaterials as well as a practical applications.